Complementary tuning semiconductor NCs properties using precursor reactivity, doping, and post-synthetic modification

by

Mohammad Sadegh Yazdanparast

B.S., Zabol University, 2007
M.S., Tarbiyat Modares University, 2010

AN ABSTRACT OF A DISSERTATION

submitted in partial fulfillment of the requirements for the degree

DOCTOR OF PHILOSOPHY

Department of Chemistry
College of Arts and Sciences

KANSAS STATE UNIVERSITY
Manhattan, Kansas

2018

Abstract

Quantum dots are nanocrystalline semiconductors in which the size is so small that optoelectronic properties are size dependent. QDs have a lot of applications in displays, solar cells, lasers, light emitting diodes, etc. The optoelectronic properties of QDs depend on their size, composition, the shape of the particles and also the surface chemistry of the QDs. Phosphine based precursors have been mostly used in the synthesis of QDs. Due to the lack of tunable reactivity, this class of precursors, QDs with different shape are obtained by under different reaction conditions. With that, branched QDs are less likely to be obtained in one step reaction using phosphine based precursors.

To synthesis QDs with a branched structure, in a single step synthesis, mixtures of precursors with different reactivity were used. Using dichalcogenides mixture, $CdSe_{1-x}S_x$ hyperbranched supra-quantum dots (HSQDs) where synthesized in a one-step microwave-assisted synthesis and shape evolution mechanism of formation of NCs studied. It is shown that the NCs formed in three steps of nucleation, aggregation, and growth. By controlling the reaction conditions, simple branched tetrapod NCs are prepared, but the obtained NCs have no emission due to unpassivated surface and defects which work as trap.

To obtain luminescent NCs obtained through doping. Hyperbranched Mn^{2+}:$ZnSe_{1-x}S_x$ NCs also prepared using a mixture of Ph_2Se_2 and Me_2S_2. The shape evolution mechanism of the formation of NCs was studied and it is shown that the NCs are formed via oriented attachment of initially formed nanoparticles. The NCs used for thiol sensing, and it observed that they have a better sensitivity and detection limit than spherical QDs.

Although hyperbranched NCs have higher sensitivities over nonbranched NCs but, the spherical NCs have better detection limit and can dispersed in aqueous medium by ZnS shell growth followed by silica shell formation. To study the effect of ZnS shell thickness on sensing property of NCs, a set of spherical Mn:ZnSe@ZnS with different ZnS shell thickness were prepared and used for thiol sensing. It observed that in organic medium, thinner ZnS layer gives the highest sensitivity and QDs with thick ZnS shell layer have less sensitivity. For measurement in aqueous medium, QDs transferred to PBS buffer after formation of silica shell over QDs. It observed that NCs with a thin ZnS shell layer lose their emission and sensing completely. Thick ZnS shell protects NCs in the silica shell formation step but they show very low sensitivity to thiol compounds as well. ZnS shell with medium thickness gives the best sensitivity in an aqueous medium.

The emission of Mn:ZnSe@ZnS QDs originated from d-d electron transition of Mn(II) ions and is independent to the size of QDs. To extend our study to QDs with band edge emission, preparation of luminescent InP QDs by post-synthetic modification is studied. InP NCs were synthesized using heat up method and successive injection of precursors. Narrow size distribution NCs obtained after size selection precipitation. Emissive NCs obtained after etching using $InCl_3$ and fluoride containing salts. The study showed that more $InCl_3$ case more etching and presence of fluoride-containing salt is necessary for band edge emission of the NCs.

Complementary tuning semiconductor NCs properties using precursor reactivity, doping, and post-synthetic modification

by

Mohammad Sadegh Yazdanparast

B.S., Zabol University, 2007
M.S., Tarbiyat Modares University, 2010

A DISSERTATION

submitted in partial fulfillment of the requirements for the degree

DOCTOR OF PHILOSOPHY

Department of Chemistry
College of Arts and Sciences

KANSAS STATE UNIVERSITY
Manhattan, Kansas

2018

Approved by:

Major Professor
Emily J McLaurin

Copyright

Abstract

Quantum dots are nanocrystalline semiconductors in which the size is so small that optoelectronic properties are size dependent. QDs have a lot of applications in displays, solar cells, lasers, light emitting diodes, etc. The optoelectronic properties of QDs depend on their size, composition, the shape of the particles and also the surface chemistry of the QDs. Phosphine based precursors have been mostly used in the synthesis of QDs. Due to the lack of tunable reactivity, this class of precursors, QDs with different shape are obtained by under different reaction conditions. With that, branched QDs are less likely to be obtained in one step reaction using phosphine based precursors.

To synthesis QDs with a branched structure, in a single step synthesis, mixtures of precursors with different reactivity were used. Using dichalcogenides mixture, $CdSe_{1-x}S_x$ hyperbranched supra-quantum dots (HSQDs) where synthesized in a one-step microwave-assisted synthesis and shape evolution mechanism of formation of NCs studied. It is shown that the NCs formed in three steps of nucleation, aggregation, and growth. By controlling the reaction conditions, simple branched tetrapod NCs are prepared, but the obtained NCs have no emission due to unpassivated surface and defects which work as trap.

To obtain luminescent NCs obtained through doping. Hyperbranched Mn^{2+}:$ZnSe_{1-x}S_x$ NCs also prepared using a mixture of Ph_2Se_2 and Me_2S_2. The shape evolution mechanism of the formation of NCs was studied and it is shown that the NCs are formed via oriented attachment of initially formed nanoparticles. The NCs used for thiol sensing, and it observed that they have a better sensitivity and detection limit than spherical QDs.

Although hyperbranched NCs have higher sensitivities over nonbranched NCs but, the spherical NCs have better detection limit and can dispersed in aqueous medium by ZnS shell growth followed by silica shell formation. To study the effect of ZnS shell thickness on sensing property of NCs, a set of spherical Mn:ZnSe@ZnS with different ZnS shell thickness were prepared and used for thiol sensing. It observed that in organic medium, thinner ZnS layer gives the highest sensitivity and QDs with thick ZnS shell layer have less sensitivity. For measurement in aqueous medium, QDs transferred to PBS buffer after formation of silica shell over QDs. It observed that NCs with a thin ZnS shell layer lose their emission and sensing completely. Thick ZnS shell protects NCs in the silica shell formation step but they show very low sensitivity to thiol compounds as well. ZnS shell with medium thickness gives the best sensitivity in an aqueous medium.

The emission of Mn:ZnSe@ZnS QDs originated from d-d electron transition of Mn(II) ions and is independent to the size of QDs. To extend our study to QDs with band edge emission, preparation of luminescent InP QDs by post-synthetic modification is studied. InP NCs were synthesized using heat up method and successive injection of precursors. Narrow size distribution NCs obtained after size selection precipitation. Emissive NCs obtained after etching using $InCl_3$ and fluoride containing salts. The study showed that more $InCl_3$ case more etching and presence of fluoride-containing salt is necessary for band edge emission of the NCs.

Table of Contents

List of Figures

List of Tables

List of Abbriviations

OLA	Oleylamine
OA	Oleic acid
Ph_2Se_2	diphenyl diselenide
ODE	Octadecene
Me_2S_2	Dimethyl disulfide
Ph_2S_2	Diphenyl disulfide
Ph_2Te_2	Diphenyl ditelluride
CdO	Cadmium oxide
MeOH	Methanol
$Mn(Oac)_2•4H_2O$	Manganese(II) acetate tetrahydrate
$MnCl_2•4H_2O$,	Manganese (II) chloride tetrahydrate
SA	Stearic acid
DDT	Dodecane thiol
NMe_4Cl,	Tetramethylammonium chloride
TEA	Trimethylamine
PhSeH	Phenylselenol
$Zn(NO_3)_2•6H_2O$	Zinc nitrate hexahydrate $Zn(NO_3)_2•6H_2O$
$Zn(Un)_2$	Zinc undecylenate $Zn(Un)_2$
NaCl	Sodium chloride
QDs	Quantum dots
HSQDs	Hyperbranched supra quantum dots
Bu_4NPF_6	Tetrabutylammonium hexafluorophosphate

DDT	Dodecanethiol
NMe_4Cl,	Tetramethylammonium chloride
NH_4OH	Ammonium hydroxide solution
TEA	Triethylamine
TEOS	Tetraethylorthosilicate
PBS	Phosphate buffered saline
$CHCl_3$	Chloroform
DTT	Dithiothreitol
PA	Palmitic acid
$InCl_3$	Indium chloride
$P(TMS)_3$	Tris(trimethylsilyl)phosphine
$In(OAc)_3$	Indium acetate
$CDCl_3$	Deuterated chloroform
DMSO	Dimethyl sulfoxide
FWHM	Full width at half maximum
HF	Hydrogen fluoride
NCs	Nanocrystals
TEM	Transmission electron microscopy
MRI	Magnetic resonance imaging
UV-Vis	UV-Visible
XRD	X-ray diffraction
EDAX	Energy-dispersive X-ray spectroscopy
HRTEM	High-resolution transmission electron

	microscopy
TOP	Tri-n-octylphosphine
TOPO	Tri-n-octylphosphine oxide

Acknowledgements

I would like to express my sincere gratitude to my PI, Dr. Emily McLaurin for the continuous support of my Ph.D study and related research, for her patience, motivation, and immense knowledge. Her guidance helped me in all the time of research and writing of this thesis. I truly believe that, I couldn't have gotten a better adviser than you for my PhD. I am very thankful to Prof. Viktor Chikan for accepting to be my co-adviser and helping me finishing my PhD. I would also like to thank my review committee members Prof. Christer Aakeröy, Prof. Takashi Ito and Prof. Bin Liu for being in my review committee and for their support whenever I ask for any help.

To all of my friends at Kansas State who have made my time here so memorable. A special thanks to Navavi Naleem for his frendly supports.

I would also like to thank my family for all the support throughout my life. My special thanks to my parents, brothers and sisters. Lastly, and most importantly, I would like to thank my wife Zeinab for being there with me throughout all the ups and downs of my life. Thank you for everything!!!

I would like to thank Department of Chemistry, Kansas State University National Science Foundation (NSF) and Johnson Cancer Research Center for providing funding for my PhD work.

Chapter 1 - Introduction

1-1 Semiconductor NCs

Materials are classified as conductive, insulators and semiconductors based on their electric conductivity[1]. In semiconductor materials, the energy gap between the valence band and the conduction band is small enough so that a small portion of electrons occupy the valence band.[1] When a bulk semiconductor material absorbs a photon, an electron of the valence band can be promoted into the conduction band. As a result, a quasi-particle called an exiton (Figure 1-1) forms in which there is a hole in the valence band and an electron in the conduction band[2].

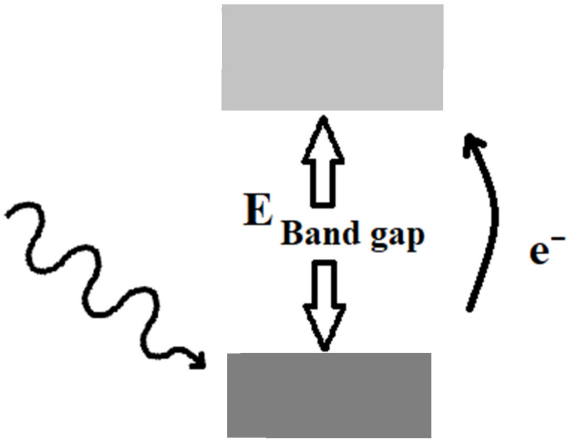

Figure 1-1 Formation of an exciton in the semiconductor due to the promotion of an electron from the valance band to the conduction band.[3]

In an exiton, depending on the material, the electron and hole orbit each other at a distance from a few to tens of nanometers, so-called Bohr radius.[2,3] The exciton recombines by emitting a photon, photoluminesence, or through nonradiative processes. A semiconductor material is called a quantum dot (QD) when the crystallite is small enough so that the possible separation distance between the excited electron and hole is smaller than the natural Bohr radius of

material.[2-4] In other words, in a QD the potential energy function model is a "particle-in-a-box" quantum mechanical system.[2–4]

The energy band structure of QDs is quantized at the band edge and then it is continuous. As shown in Figure 1-2 this energy band structure is in between that of molecules, which have completely distinct energy levels, and that of bulk semiconductors, which have continuous energy levels.[4–6]

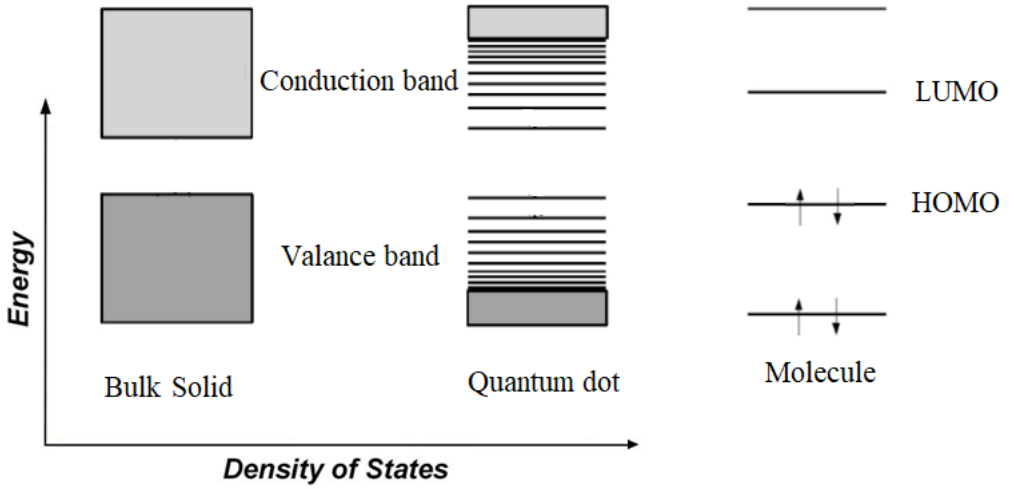

Figure 1-2 Electronic energy states of a bulk semiconductor, quantum dot and a molecule. Reprinted with permission from ref 6. Copyright © 2010, American Chemical Society.

As a result, the absorption spectra of QDs have a distinct sharp peak and broad absorption at higher energies. In other words, QDs combine the properties of small molecule fluorophores and bulk semiconductors (Figure 1-3).

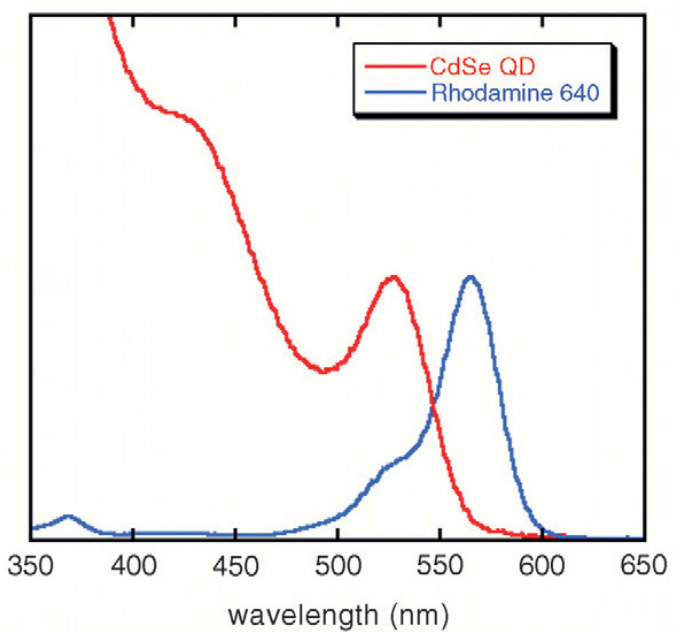

Figure 1-3 UV-Vis absorption spectrum of a QD (red) and an organic molecule (Rhodamine)[7] (blue). Reprinted with permission from ref 7. Copyright © 2011 Elsevier Ltd.

Due to quantum confinement a decrease in the size of QDs causes the exiton to have higher energy so smaller QDs, have higher energy excitons.[8,9] Thus, by tuning the size of QDs the electronic states and associated properties such as optical properties can be tuned. Figure 1-4, shows a rainbow of fluorescent colors all produced by CdSe QDs of various sizes.

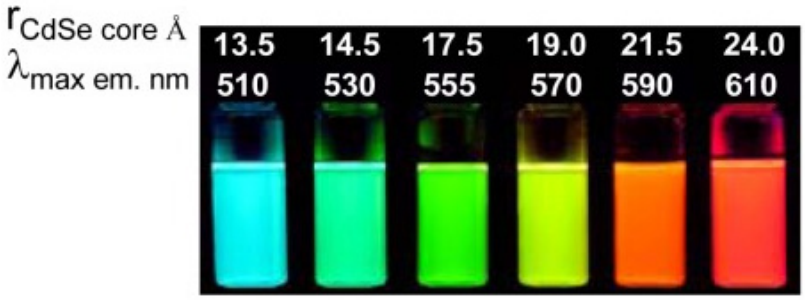

Figure 1-4 Size-dependent emission of CdSe QDs. Reprinted with permission from ref 31

QDs have several advantages over organic dyes. In term of quality, extremely bright QDs with quantum yields (QYs) near unity can be prepared.[10] Regarding photostability, unlike organic dye

molecules that tend to photobleach over a short period, QDs can last very long under constant excitation.[7,11,12] Any dye has a very narrow absorption spectral window (Figure 1-3), but QDs absorb any photons with higher energy than their bandgap and also have much larger absorption coefficients. Although dyes have better Stoke shift than QDs but the ability of QDs in the absorption of photon far above their band gap overcome their small Stoke shift.[7,11–15] These advantages made QDs very versatile for different applications. For instance, tunable energy gaps and multiple exciton generation features are very desirable for making solar cells.[7,11,13,14] The spectral tunability and high luminescence efficiency of QDs make them excellent for light emitting diodes (LED).[16,17] Notably, the luminance of displays for QD LEDs can be 10 to 100 times higher than organic LEDs.[18]

1-2 II-VI QDs

Among different types of nanomaterials, two classes of metal chalcogenides and noble metal nanoparticles are the most investigated due to their special electronic, optical, and catalytic properties.[19–21]

Oxygen (O), sulfur (S), selenium (Se), tellurium (Te) and polonium (Po) are the chemical elements of group 16 of the periodic table and are known as chalcogens.[19] Metal chalcogenide QDs mainly consist of sulfur, selenium and tellurium as the chalcogenide. QDs such as PbS, Ag_2S, CdS, ZnS, CdSe, and CdTe have broad absorbance in UV–Visible–IR range of electromagnetic spectrum.[18] These QDs have multiple exciton generation capability in which more than one photo induced electron-hole pair can be generated in a QD particle.[21–25] The color purity of their emission depends on the size distribution of the QDs, and their QY depends on their surface chemistry of the QDs.[19–21]

Metal chalcogenides QDs attracted considerable attention due to their easy synthesis, lower cost of the precursors, and higher performance in comparison with comparison with III-V QDs such as InP and InAs and InGaP.[29] Their photovoltaic and photo-optical properties are particularly studed[12] due to their application potentials in solar cells, optoelectronic sensors, bioimaging, cancer detection (Figure 1-5)[30] and tracking particles or cells.[31]

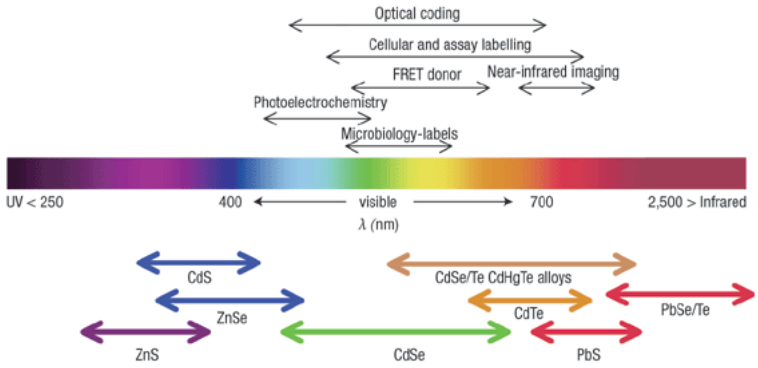

Figure 1-5 Metal chalcogenides can be used for different applications from visible to the near-infrared area. Reprinted with permission from ref 31.

For most of the applications, QDs with specific morphology, crystallinity, and composition are required. So controlling these parameters is critical role in their applications and performance.[32]

1-3 Ternary alloy materials

As mentioned, size and composition are the two main factors that determine the optoelectronic properties of QDs.[33] The most common method for achieving the desired band gap is by tuning the size of QDs,[20,26,27] but, the size of QDs plays an important role in their application. Figure 1-6 shows the band gap energies of popular binary semiconductors. For a typical semiconductor QD, the band gap of bulk semiconductor and its Bohr radius determine the spectra at which the different sizes QDs will have band edge emission which mean one can not obtain QDs of a semiconductor with desired size and desired band edge emission.[34–36] In some cases the size of QDs might limit their application. For instance, in case of solar cells, using QDs with different

band gaps increases the light harvesting efficiency, but smaller QDs that have larger band gaps, has less efficient charge transfer. In bioimaging and labeling, small QDs are desirable, but due to the higher penetration of infrared light into tissues,[38] QDs with emission in infrared region are more desirable. By just relying on quantum confinement of QDs, one can obtain infrared emotion from larger QDs.[37] When QDs are incorporated into mesoporous materials and other superstructures also their size can significantly affect their application.[39]

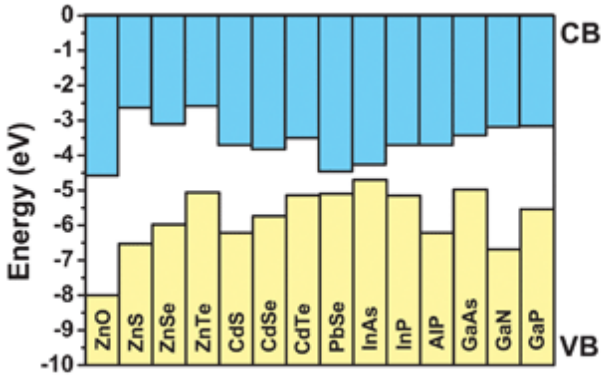

Figure 1-6 The band gap of some popular binary semiconductors materials (VB: valence band and CB: conduction band). Reprinted with permission from ref 34.

As the optoelectronic properties of ternary alloyed QDs can be tuned by changing not only the size but also the composition, the application limitations related to the size of QDs can be solved by tuning the composition. Among different alloys, ternary alloy QDs are of primary interest because the optical properties are tunable simply by adjusting the stoichiometric ratio of two components in the composition of the alloy.[40] Ternary QDs these materials have attracted enormous attention to for use in lasers,[41] solar cells,[42] light-emitting devices (LEDs)[28], bioimaging and biological fluorescence labeling.[31]

There are two different ways to classify alloy QDs. One is based on composition components. In this classification, if the parent semiconductors have common anion or cation, the alloy is a

ternary QD (three element alloys) and if the parents have no common element, the alloy will be a quartenary QD (four element alloy).[40,43,44] The second classification is based on the homogeneity of the structure.[40] Homogeneous QDs have the same composition in the entire particle.[40] Gradient particles have different compositions at the center and surface and the composition of particle smoothly change.[45–51] In core-shell structures, the composition of the core and the shell is different and changes drastically at the layers interface.[40]

In comparison, colloidal II-VI QDs such as CdS, ZnTe and CdSe with size-tunability, high crystallinity and narrow size distribution were prepared in 1980s.[36–38] Regarding the properties, due to their wide energy bands, the wavefunctions of the III-V materials are delocalized, but ionic solids have narrower energy bands and localized wavefunctions. When the wavefunctions and electrons are more localized, the dielectric constants are larger which cause attraction between holes and electrons to be stronger. III-V QDs have high charging energies and nonlinear optical susceptibilities which make them great candidates for being used in telecommunication field as photonic components for single-electron switching devices.[39,40] The main advantage of II-VI QDs is their ease synthesis, low cost of precursors and high quality and their biggest disadvantage is that cadmium-based QDs emit in the visible region of electromagnetic spectrum and cadmium toxicity limits their applications. Because of toxicity of cadmium, attentions have shifted to the indium-based QDs.[18,41,42]

1-4 III-V and II-VI semiconductors

Groups III-V and II-VI semiconductors QDs are the most promising and studied semiconductor materials, however, they have differences.[52] The bonding of group III-V materials has higher covalent characteristic which causes the properties of the III-V QDs to be dramatically different

from those of the II-VI materials with more ionic bonds.[53,54] This difference affects both the synthesis and properties of these two classes of materials significantly. The covalent nature of the bond of the III-V materials causes their synthesis to be more challenging and until very recently the synthesized QDs suffered from poor crystallinity and low quantum yield.[33-35]

In comparison, colloidal II-VI QDs such as CdS, ZnTe and CdSe with size-tunability, high crystallinity and narrow size distribution were prepared in 1980s.[55–57] Regarding the properties, due to their wide energy bands, the wavefunctions of the III-V materials are delocalized, but ionic solids have narrower energy bands and localized wavefunctions. When the wavefunctions and electrons are more localized, the dielectric constants are larger which cause attraction between holes and electrons to be stronger. III-V QDs have high charging energies and nonlinear optical susceptibilities which make them a great candidate for being used in telecommunication field as photonic components for single-electron switching devices.[58,59] The main advantage of II-VI QDs is their ease synthesis, low cost of precursors and high quality and their biggest disadvantage is that cadmium-based QDs emit in the visible region of electromagnetic spectrum and cadmium toxicity limits their applications. Because of toxicity of cadmium, attentions have shifted to the indium-based QDs.[18,60,61]

1-5 Mn^{2+}-Doped NCs

In bulk semiconductors, optical and electronic properties can be affected by impurities.[62–65] For instance, dopants can provide carriers of electrical current by donating electrons to the semiconductor in n-type doped materials or taking electrons from the semiconductor in p-type doped semiconductors. It should be noted that the synthesis of alloys is different from doping.[65] Alloys have different band gap and quantum confinement from their parent semiconductors; however, doping introduces new electronic energy levels without changing the band gap of the

host quantum dot.[40] In the case of QDs, due to the confinement of the electronic states into a small volume, different phenomena might be observed. As Mn(II) has a visible phosphorescence at ~580 nm resulted from the Mn^{2+} $^4T_1 \rightarrow {}^6A_1$ transition, manganese-doped QDs have very different emission properties from analogous undoped QDs.[66] However, the $^4T_1$ and $^6A_1$ energy levels should be within the band gap of material.[67] With that, research groups have developed different procedures for doping of wide band gap materials such as ZnSe with Mn(II).[66,68–73] As a result, these materials have a large Stokes shift which is an important advantage in some applications such as bioanalysis in by minimizing self-quenching of the PL[68]. Another advantage of Mn(II)-doped QDs is that Mn^{2+} acts as a paramagnetic center ($S = {}^5/_2$) and the doped NCs can be paramagnetic.[67,73]

1-6 Shape evolution of semiconductor NCs

By controlling reaction parameters during the synthesis, QDs with different shapes can be prepared.

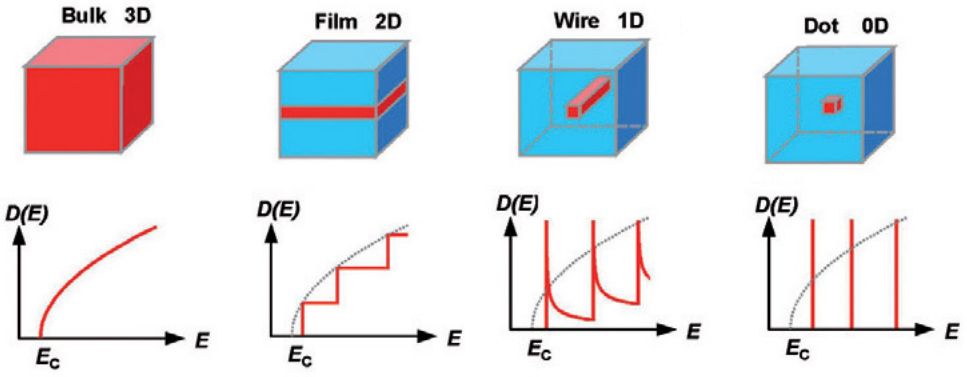

Figure 1-7 Effect of reduced dimensionality, (a) Charge carriers are confined in a semiconductor (red) with a smaller bandgap than the cladding semiconductor (blue). The confinement changes the density of states D(E). Ec is the conduction-band edge of a 3D semiconductor. Reprinted with permission from ref 14. Copyright © 2011 Elsevier Ltd.

As it shown in Figure 1-7, the shape of NCs determines the energy of the electron states and band gap of the particles. For instance in case of CdSe, an spherical quantum dot (QD) has a larger band gap, and the density of electron and hole states are less than those of an elongated quantum dot. By increasing the temperature, the bandgap gets smaller in both shapes, but the change for spherical QDs is less.[74] It is shown that the shape of silicon nanoparticles also strongly affects their optical properties and the band gap of cubic nanoparticles is smaller than octahedral of the same volume.[75]

Branched NCs can have enhanced properties from their spherical or enlongated counterparts, which leads to their higher functionality.[76] Due to that, branched NCs are used as highly beneficial elements in water-splitting systems,[77] light-emitting diodes, batteries, solar cells,[6,10–13] and single-electron transistors.[78] Among different morphologies of branched QDs, colloidal tetrapod nanocrystals have unique properties and advantages over spherical QDs.[79,80] Tetrapod QDs have relatively large absorption cross sections, intrinsic efficient charge separation in which the arms and cores tend to have different charges, and long biexciton lifetime and enhanced charge transport.[81–84] Moreover, enhanced self-assembly and self-aligning of tetrapods gives advantages when device assembly. For example, changing the surface ligands of QDs affects the self-assembly and causes obtaining the reproducible nanoscopic morphology after infusion of QDs in polymers to be challenging. It is shown that self-assembly of CdSe tetrapods can be independent of surface ligands, which enables more reproducible infusion of tetrapod QDs in semiconducting polymers.[85] Also, in dye-sensitized solar cells [86] and lithium ion batteries, [87] self-aligning of tetrapods on the substrate and their higher surface area, increases their charge transfer, resulting in higher performance of the device.[76,88] These advantages caused tetrapods

QDs to be studied as a promising candidate for lasers[89], light emitting diodes, photovoltaic devices,[90], and dual electroluminescence.[91]

Despite the great success in the engineering of the shape and size of NCs, there is still a lack of fundamental understanding in the mechanism of formation of some structures. For instance, there are just few general approaches for engineering the final shape of nanocrystals.[92–94] Even, in those cases that the shape evolution processes are demonstrated, the experimental conditions needs to be studied for the synthesis of other materials with the desired shape.[32]

1-7 Microwave-assisted NCs synthesis

Microwave heating is being used widely in the synthesis of both organic and inorganic compounds. [95–99] In a conventional flask heating system, the heat goes from the container wall to the reaction mixture and because of that, the heating is not uniform through the mixture.[100,101] However, in microwave assisted reactions, microwave irradiation causes heat generation and the components with good microwave dissipation factors.[97,102] Considering the delicate synthetic procedures of high-quality QDs, which require air and moisture free conditions, conventional heating and Schilink lines are mainly used in the QD synthesis.[97] However, considering the advantages of microwave heating including fast, uniform, and direct heating of reaction mixture and precursors, there is an interest in the microwave-assisted synthesis of QDs.[97] Moreover, as usually sealed vessels are used in microwave-assisted synthesis, precursors and solvents with low boiling can be used in these synthesizes, but also, volatile intermediates that might be formed during the reaction will remain in the reaction mixture. The later can be more important in the synthesis of alloys. If the precursor of one component of ally has a low boiling point, in

Schlenk line synthesis, the reaction parameters such as temperature need to be controlled carefully to get alloys with the same composition in batch to batch synthesizes.[102]

The above discussion shows that the properties of semiconductor NCs are dependents to several factors such as their composition, size and shape. Researchers try different methods to obtain desired NCs such as using different precursors, synthetic methods or by post-synthetic modification.

Here, we will examine synthesis of branched heterostructure NCs in a single-step reaction using mixture of precursors with different reactivities. Then we will examine single-step synthesis of dopped branched NCs for obtaining luminescent hyperbranched NCs. In the end, we study surface passivation using post-synthetic modifications for achieving band-edge emission.

The goals of this thesis are as follows:

I. Synthesis of heterostructure branched NCs in a single step reaction using mixture and study of shape evolution mechanism. (Chapter 2).

II. Achieve luminescent hyperbranched NCs through doping and examine their application potential as a chemical sensor (Chapters 3 and 4).

III. Tuning NCs properties using post-synthetic modification by ligand exchange based on hard-soft ligand/ion classification (Chapter 5).

1-8 References

(1) A. Neamen, D. Semiconductor Physics and Devices : Basic Principles / D.A. Neamen. **2012**.

(2) Efros, A.; L. Efros, A. Interband Light Absorption in Semiconductor Spheres. *Sov. Phys. Semicond.* **1982**, *16*, 772–775.

(3) Alivisatos, A. P. Perspectives on the Physical Chemistry of Semiconductor Nanocrystals. *J. Phys. Chem.* **1996**, *100* (31), 13226–13239.

(4) Kippeny, T.; Swafford, L. A.; Rosenthal, S. J. Semiconductor Nanocrystals: A Powerful Visual Aid for Introducing the Particle in a Box. *J. Chem. Educ.* **2002**, *79* (9), 1094.

(5) O'Farrell, N.; Houlton, A.; Horrocks, B. R. Silicon Nanoparticles: Applications in Cell Biology and Medicine. *Int. J. Nanomedicine* **2006**, *1* (4), 451–472.

(6) Smith, A. M.; Nie, S. Semiconductor Nanocrystals: Structure, Properties, and Band Gap Engineering. *Acc. Chem. Res.* **2010**, *43* (2), 190–200.

(7) Smyder, J. A.; Krauss, T. D. Coming Attractions for Semiconductor Quantum Dots. *Mater. Today* **2011**, *14* (9), 382–387.

(8) Rossetti, R.; Ellison, J. L.; Gibson, J. M.; Brus, L. E. Size Effects in the Excited Electronic States of Small Colloidal CdS Crystallites. *J. Chem. Phys.* **1984**, *80* (9), 4464–4469.

(9) Sapsford, K. E.; Pons, T.; Medintz, I. L.; Mattoussi, H. Biosensing with Luminescent Semiconductor Quantum Dots. *Sensors* **2006**, *6* (8), 925–953.

(10) Hines, M. A.; Guyot-Sionnest, P. Synthesis and Characterization of Strongly Luminescing ZnS-Capped CdSe Nanocrystals. *J. Phys. Chem.* **1996**, *100* (2), 468–471.

(11) Rühle, S.; Shalom, M.; Zaban, A. Quantum-Dot-Sensitized Solar Cells. *ChemPhysChem 11* (11), 2290–2304.

(12) Mal, J.; Nancharaiah, Y. V.; Hullebusch, E. D. van; Lens, P. N. L. Metal Chalcogenide Quantum Dots: Biotechnological Synthesis and Applications. *RSC Adv.* **2016**, *6* (47), 41477–41495.

(13) Yu, W. W.; Qu, L.; Guo, W.; Peng, X. Experimental Determination of the Extinction Coefficient of CdTe, CdSe, and CdS Nanocrystals. *Chem. Mater.* **2003**, *15* (14), 2854–2860.

(14) Bimberg, D.; Pohl, U. W. Quantum Dots: Promises and Accomplishments. *Mater. Today* **2011**, *14* (9), 388–397.

(15) Kershaw, S. V.; Susha, A. S.; Rogach, A. L. Narrow Bandgap Colloidal Metal Chalcogenide Quantum Dots: Synthetic Methods, Heterostructures, Assemblies, Electronic and Infrared Optical Properties. *Chem. Soc. Rev.* **2013**, *42* (7), 3033–3087.

(16) Shields, A. J. Semiconductor Quantum Light Sources. *Nat. Photonics* **2007**, *1* (4), 215–223.

(17) Nakamura, S. The Roles of Structural Imperfections in InGaN-Based Blue Light-Emitting Diodes and Laser Diodes. *Science* **1998**, *281* (5379), 956–961.

(18) Fan, G.; Wang, C.; Fang, J. Solution-Based Synthesis of III–V Quantum Dots and Their Applications in Gas Sensing and Bio-Imaging. *Nano Today* **2014**, *9* (1), 69–84.

(19) Sharma, D.; Jha, R.; Kumar, S. Quantum Dot Sensitized Solar Cell: Recent Advances and Future Perspectives in Photoanode. *Sol. Energy Mater. Sol. Cells* **2016**, *155*, 294–322.

(20) Cao, S.; Ji, W.; Zhao, J.; Yang, W.; Li, C.; Zheng, J. Color-Tunable Photoluminescence of Cu-Doped Zn–In–Se Quantum Dots and Their Electroluminescence Properties. *J. Mater. Chem. C* **2016**, *4* (3), 581–588.

(21) Kechiantz, A.; Afanasev, A.; Lazzari, J.-L. Releasing Confined Holes from Type-II Quantum Dots by Inelastic Scattering with Hot Photoelectrons. *Sol. Energy Mater. Sol. Cells* **2016**, *144*, 767–774.

(22) Dhomkar, S.; Manna, U.; Peng, L.; Moug, R.; Noyan, I. C.; Tamargo, M. C.; Kuskovsky, I. L. Feasibility of Submonolayer ZnTe/ZnCdSe Quantum Dots as Intermediate Band Solar Cell Material System. *Sol. Energy Mater. Sol. Cells* **2013**, *117*, 604–609.

(23) Kamat, P. V. Quantum Dot Solar Cells. The Next Big Thing in Photovoltaics. *J. Phys. Chem. Lett.* **2013**, *4* (6), 908–918.

(24) Boustanji, H.; Jaziri, S.; Lazzari, J.-L. Contribution of a Single Quantum Dots Layer in Intermediate Band Solar Cells: A Capacitance Analysis. *Sol. Energy Mater. Sol. Cells* **2017**, *159*, 633–639.

(25) Chand, S.; Thakur, N.; Katyal, S. C.; Barman, P. B.; Sharma, V.; Sharma, P. Recent Developments on the Synthesis, Structural and Optical Properties of Chalcogenide Quantum Dots. *Sol. Energy Mater. Sol. Cells* **2017**, *168*, 183–200.

(26) Yuan, X.; Ma, R.; Zhang, W.; Hua, J.; Meng, X.; Zhong, X.; Zhang, J.; Zhao, J.; Li, H. Dual Emissive Manganese and Copper Co-Doped Zn–In–S Quantum Dots as a Single Color-Converter for High Color Rendering White-Light-Emitting Diodes. *ACS Appl. Mater. Interfaces* **2015**, *7* (16), 8659–8666.

(27) Allan, J. M.; Abdul Mumin, M.; Xu, W. Z.; Al Sharari, Q.; Charpentier, P. A. Surface Functionalized Bare and Core–Shell Quantum Dots in Poly(Ethylene-Co-Vinyl Acetate) for Light Selective Nanocomposite Films. *Sol. Energy Mater. Sol. Cells* **2014**, *123*, 30–40.

(28) Yang, Y.; Zheng, Y.; Cao, W.; Titov, A.; Hyvonen, J.; Manders, J. R.; Xue, J.; Holloway, P. H.; Qian, L. High-Efficiency Light-Emitting Devices Based on Quantum Dots with Tailored Nanostructures. *Nat. Photonics* **2015**, *9* (4), 259.

(29) Joo, J.; Na, H. B.; Yu, T.; Yu, J. H.; Kim, Y. W.; Wu, F.; Zhang, J. Z.; Hyeon, T. Generalized and Facile Synthesis of Semiconducting Metal Sulfide Nanocrystals. *J. Am. Chem. Soc.* **2003**, *125* (36), 11100–11105.

(30) Trindade, T.; O'Brien, P.; Pickett, N. L. Nanocrystalline Semiconductors: Synthesis, Properties, and Perspectives. *Chem. Mater.* **2001**, *13* (11), 3843–3858.

(31) Medintz, I. L.; Uyeda, H. T.; Goldman, E. R.; Mattoussi, H. Quantum Dot Bioconjugates for Imaging, Labelling and Sensing. *Nat. Mater.* **2005**, *4* (6), 435–446.

(32) Polavarapu, L.; Mourdikoudis, S.; Pastoriza-Santos, I.; Pérez-Juste, J. Nanocrystal Engineering of Noble Metals and Metal Chalcogenides: Controlling the Morphology, Composition and Crystallinity. *CrystEngComm* **2015**, *17* (20), 3727–3762.

(33) Wang, B.; Jiang, Y.; Liu, C.; Lan, X.; Liu, X.; Wang, W.; Duan, H.; Zhang, Y.; Li, S.; Zhang, Z. One-Pot Synthesis of Homogeneous CdSexS1−x Alloyed Quantum Dots with Tunable Composition in a Green N-Oleoylmorpholine Solvent. *Phys. Status Solidi A 209* (2), 306–312.

(34) Mello Donegá, C. de. Synthesis and Properties of Colloidal Heteronanocrystals. *Chem. Soc. Rev.* **2011**, *40* (3), 1512–1546.

(35) Smith, D. K.; Luther, J. M.; Semonin, O. E.; Nozik, A. J.; Beard, M. C. Tuning the Synthesis of Ternary Lead Chalcogenide Quantum Dots by Balancing Precursor Reactivity. *ACS Nano* **2011**, *5* (1), 183–190.

(36) and, C. C. Y.; Li, S. Size, Dimensionality, and Constituent Stoichiometry Dependence of Bandgap Energies in Semiconductor Quantum Dots and Wires *J. Phys. Chem. C* **2008,** *112,* 2851-2856.

(37) Swafford, L. A.; Weigand, L. A.; Bowers, M. J.; McBride, J. R.; Rapaport, J. L.; Watt, T. L.; Dixit, S. K.; Feldman, L. C.; Rosenthal, S. J. Homogeneously Alloyed CdSxSe1-x Nanocrystals: Synthesis, Characterization, and Composition/Size-Dependent Band Gap. *J. Am. Chem. Soc.* **2006**, *128* (37), 12299–12306.

(38) Cassette, E.; Helle, M.; Bezdetnaya, L.; Marchal, F.; Dubertret, B.; Pons, T. Design of New Quantum Dot Materials for Deep Tissue Infrared Imaging. *Adv. Drug Deliv. Rev.* **2013**, *65* (5), 719–731.

(39) Thi, L. A.; Cong, N. D.; Dang, N. T.; Nghia, N. X.; Quang, V. X. Optical and Phonon Characterization of Ternary $CdSe_xS_{1-x}$ Alloy Quantum Dots. *J. Electron. Mater.* **2016**, *45* (5), 2621–2626.

(40) Regulacio, M. D.; Han, M.-Y. Composition-Tunable Alloyed Semiconductor Nanocrystals. *Acc. Chem. Res.* **2010**, *43* (5), 621–630.

(41) Fafard, S.; Hinzer, K.; Raymond, S.; Dion, M.; McCaffrey, J.; Feng, Y.; Charbonneau, S. Red-Emitting Semiconductor Quantum Dot Lasers. *Science* **1996**, *274* (5291), 1350–1353.

(42) Lee, H.; Wang, M.; Chen, P.; Gamelin, D. R.; Zakeeruddin, S. M.; Grätzel, M.; Nazeeruddin, M. K. Efficient CdSe Quantum Dot-Sensitized Solar Cells Prepared by an Improved Successive Ionic Layer Adsorption and Reaction Process. *Nano Lett.*, **2009**, 9 (12), 4221–4227.

(43) Maroudas, D.; Han, X.; Pandey, S. C. Design of Semiconductor Ternary Quantum Dots with Optimal Optoelectronic Function. *AIChE J. 59* (9), 3223–3236.

(44) Han, X.; Pandey, S. C.; Maroudas, D. Kinetics of Interdiffusion in Semiconductor Ternary Quantum Dots. *Appl. Phys. Lett.* **2012**, *101* (14), 141906.

(45) Debnath, T.; Parui, K.; Maiti, S.; Ghosh, H. N. An Insight into the Interface through Excited-State Carrier Dynamics for Promising Enhancement of Power Conversion Efficiency in a Mn-Doped CdZnSSe Gradient Alloy. *Chem. – Eur. J.* **2017**, *23* (15), 3755–3763.

(46) Gao, Z.; Zhang, Q.; Naylor, C. H.; Kim, Y.; Abidi, I. H.; Ping, J.; Ducos, P.; Zauberman, J.; Zhao, M.-Q.; Rappe, A. M.; et al. Crystalline Bilayer Graphene with Preferential Stacking from Ni–Cu Gradient Alloy. *ACS Nano* **2018**, *12* (3), 2275–2282.

(47) Cho, J.; Jung, Y. K.; Lee, J.-K.; Jung, H.-S. Highly Efficient Blue-Emitting CdSe-Derived Core/Shell Gradient Alloy Quantum Dots with Improved Photoluminescent Quantum Yield and Enhanced Photostability. *Langmuir* **2017**, *33* (15), 3711–3719.

(48) Roy, D.; Mandal, S.; De, C. K.; Kumar, K.; Mandal, P. K. Nearly Suppressed Photoluminescence Blinking of Small-Sized, Blue–Green–Orange–Red Emitting Single CdSe-Based Core/Gradient Alloy Shell/Shell Quantum Dots: Correlation between Truncation Time and Photoluminescence Quantum Yield. *Phys. Chem. Chem. Phys.* **2018**, *20* (15), 10332–10344.

(49) Yoon, D.; Bang, S.; Park, J.; Kim, J.; Baik, H.; Yang, H.; Lee, K. One Pot Synthesis of Octahedral {111} CuIr Gradient Alloy Nanocrystals with a Cu-Rich Core and an Ir-Rich Surface and Their Usage as Efficient Water Splitting Catalyst. *CrystEngComm* **2015**, *17* (36), 6843–6847.

(50) Roy, D.; Routh, T.; Asaithambi, A. V.; Mandal, S.; Mandal, P. K. Spectral and Temporal Optical Behavior of Blue-, Green-, Orange-, and Red-Emitting CdSe-Based Core/Gradient Alloy Shell/Shell Quantum Dots: Ensemble and Single-Particle Investigation Results *J. Phys. Chem. C*, **2016**, 120 (6), pp 3483–3491.

(51) Surface Modification and Its Role in the Preparation of FeSi Gradient Alloys with Good Magnetic Property and Ductility. *J. Magn. Magn. Mater.* **2018**, *451*, 373–378.

(52) Mikhailov, A. I.; Kabanov, V. F.; Gorbachev, I. A.; Glukhovsky, E. G. Study of the Properties of II–VI and III–V Semiconductor Quantum Dots. *Semiconductors* **2018**, *52* (6), 750–754.

(53) Green, M. Solution Routes to III–V Semiconductor Quantum Dots. *Curr. Opin. Solid State Mater. Sci.* **2002**, *6* (4), 355–363.

(54) Guzelian, A. A.; Banin, U.; Kadavanich, A. V.; Peng, X.; Alivisatos, A. P. Colloidal Chemical Synthesis and Characterization of InAs Nanocrystal Quantum Dots. *Appl. Phys. Lett.* **1996**, *69* (10), 1432–1434.

(55) Alivisatos, A. P. Semiconductor Clusters, Nanocrystals, and Quantum Dots. *Science* **1996**, *271* (5251), 933–937.

(56) Burda, C.; Chen, X.; Narayanan, R.; El-Sayed, M. A. Chemistry and Properties of Nanocrystals of Different Shapes. *Chem. Rev.* **2005**, *105* (4), 1025–1102.

(57) Norris, D. J.; Bawendi, M. G. Measurement and Assignment of the Size-Dependent Optical Spectrum in CdSe Quantum Dots. *Phys. Rev. B* **1996**, *53* (24), 16338–16346.

(58) Vahala, K. J. Optical microcavities *Nature.* **2003** 14, 839-46.

(59) Nakamura, H.; Sato, N.; Tabuchi, N. An Efficient and Portable Scheduler for RTOS Simulation and Its Certified Integration to SystemC. In *Proceedings of the Design Automation Test in Europe Conference*; 2006; Vol. 1, pp 1–2.

(60) Park, J. P.; Lee, J.-J.; Kim, S.-W. Highly Luminescent InP/GaP/ZnS QDs Emitting in the Entire Color Range via a Heating up Process. *Sci. Rep.* **2016**, *6*, 30094.

(61) Brunetti, V.; Chibli, H.; Fiammengo, R.; Galeone, A.; Malvindi, M. A.; Vecchio, G.; Cingolani, R.; Nadeau, J. L.; Pompa, P. P. InP/ZnS as a Safer Alternative to CdSe/ZnS Core/Shell Quantum Dots: In Vitro and in Vivo Toxicity Assessment. *Nanoscale* **2013**, *5* (1), 307–317.

(62) Zandi, O.: Agrawal, A.; Shearer, A. B.; Reimnitz, L. C.; Dahlman, C. J.; Staller, C. M.; Milliron, D. J.; Impacts of surface depletion on the plasmonic properties of doped semiconductor nanocrystals. *Nat. Mater*. **2018**, 17, 710–717.

(63) Hartstein, K. H.; Brozek, C. K.; Hinterding, S. O. M.; Gamelin, D. R. Copper-Coupled Electron Transfer in Colloidal Plasmonic Copper-Sulfide Nanocrystals Probed by in Situ Spectroelectrochemistry. *J. Am. Chem. Soc.* **2018**, *140* (9), 3434–3442.

(64) Araujo, J. J.; Brozek, C. K.; Kroupa, D. M.; Gamelin, D. R. Degenerately N-Doped Colloidal PbSe Quantum Dots: Band Assignments and Electrostatic Effects. *Nano Lett.* **2018**, *18* (6), 3893–3900.

(65) Norris, D. J.; Efros, A. L.; Erwin, S. C. Doped Nanocrystals. *Science* **2008**, *319* (5871), 1776–1779.

(66) Thakar, R.; Chen, Y.; Snee, P. T. Efficient Emission from Core/(Doped) Shell Nanoparticles: Applications for Chemical Sensing. *Nano Lett.* **2007**, *7* (11), 3429–3432.

(67) Norris, D. J.; Yao, N.; Charnock, F. T.; Kennedy, T. A. High-Quality Manganese-Doped ZnSe Nanocrystals. *Nano Lett.* **2001**, *1* (1), 3–7.

(68) Wu, P.; Yan, X.-P. Doped Quantum Dots for Chemo/Biosensing and Bioimaging. *Chem. Soc. Rev.* **2013**, *42* (12), 5489–5521.

(69) Ke, B.; Bai, X.; Wang, R.; Shen, Y.; Cai, C.; Bai, K.; Zeng, R.; Zou, B.; Chen, Z. Alkylthiol-Enabled Se Powder Dissolving for Phosphine-Free Synthesis of Highly Emissive, Large-Sized and Spherical Mn-Doped ZnSeS Nanocrystals. *RSC Adv.* **2017**, *7* (71), 44867–44873.

(70) Jalalah, M.; Ko, Y.-H.; Harraz, F. A.; Al-Assiri, M. S.; Park, J.-G. Enhanced Efficiency and Current Density of Solar Cells via Energy-down-Shift Having Energy-Tuning-Effect of Highly UV-Light-Harvesting Mn2+-Doped Quantum Dots. *Nano Energy* **2017**, *33*, 257–265.

(71) Zhang, L.-J.; Shen, X.-C.; Liang, H.; Chen, F.-Y.; Huang, H.-J. Phosphine-Free Synthesis of ZnSe:Mn and ZnSe:Mn/ZnS Doped Quantum Dots Using New Se and S Precursors. *New J. Chem.* **2013**, *38* (1), 448–454.

(72) Zhou, R.; Lu, X.; Yu, H.; Wu, L.; Wu, P.; Hou, X. Se Powder as Precursor without Solubilization for Mn-Doped ZnSe QDs: Fast Synthesis and Analytical Characterization. *Microchem. J.* **2017**, *134*, 191–196.

(73) S. Yazdanparast, M.; T. Webb, M.; J. McLaurin, E. Single-Step Synthesis of Hyperbranched, Luminescent Mn 2+ -Doped ZnSe 1−x S x Nanocrystals Using Dichalcogenide Precursors. *J. Mater. Chem. C* **2016**, *4* (28), 6907–6913.

(74) Chen, L.; Bao, H.; Tan, T.; Prezhdo, O. V.; Ruan, X. Shape and Temperature Dependence of Hot Carrier Relaxation Dynamics in Spherical and Elongated CdSe Quantum Dots. *J. Phys. Chem. C* **2011**, *115* (23), 11400–11406.

(75) Wilson, H. F.; McKenzie-Sell, L.; Barnard, A. S. Shape Dependence of the Band Gaps in Luminescent Silicon Quantum Dots. *J. Mater. Chem. C* **2014**, *2* (44), 9451–9456.

(76) Zamani, R. R.; Ibáñez, M.; Luysberg, M.; García-Castelló, N.; Houben, L.; Prades, J. D.; Grillo, V.; Dunin-Borkowski, R. E.; Morante, J. R.; Cabot, A.; et al. Polarity-Driven Polytypic Branching in Cu-Based Quaternary Chalcogenide Nanostructures. *ACS Nano* **2014**, *8* (3), 2290–2301.

(77) Amirav, L.; Alivisatos, A. P. Photocatalytic Hydrogen Production with Tunable Nanorod Heterostructures, *J. Phys. Chem. Lett.*, **2010**, *1* (7), 1051–1054.

(78) Yi Cui,; Uri Banin,; Mikael T. Björk,; A. Paul Alivisatos,. Electrical Transport through a Single Nanoscale Semiconductor Branch Point *Nano Lett.*, **2005**, 5 (7), 1519–1523.

(79) Talapin, D. V.; Nelson, J. H.; Shevchenko, E. V.; Aloni, S.; Sadtler, B.; Alivisatos, A. P. Seeded Growth of Highly Luminescent CdSe/CdS Nanoheterostructures with Rod and Tetrapod Morphologies. *Nano Lett.* **2007**, *7* (10), 2951–2959.

(80) Fiore, A.; Mastria, R.; Lupo, M. G.; Lanzani, G.; Giannini, C.; Carlino, E.; Morello, G.; De Giorgi, M.; Li, Y.; Cingolani, R.; et al. Tetrapod-Shaped Colloidal Nanocrystals of II−VI Semiconductors Prepared by Seeded Growth. *J. Am. Chem. Soc.* **2009**, *131* (6), 2274–2282.

(81) Liao, Y.; Xing, G.; Mishra, N.; Sum, T. C.; Chan, Y. Low Threshold, Amplified Spontaneous Emission from Core-Seeded Semiconductor Nanotetrapods Incorporated into a Sol–Gel Matrix. *Adv. Mater.* **2012**, *24* (23), OP159–OP164.

(82) Mishra, N.; Wu, W.-Y.; Srinivasan, B. M.; Hariharaputran, R.; Zhang, Y.-W.; Chan, Y. Continuous Shape Tuning of Nanotetrapods: Toward Shape-Mediated Self-Assembly. *Chem. Mater.* **2016**, *28* (4), 1187–1195.

(83) Dayal, S.; Kopidakis, N.; Olson, D. C.; Ginley, D. S.; Rumbles, G. Photovoltaic Devices with a Low Band Gap Polymer and CdSe Nanostructures Exceeding 3% Efficiency. *Nano Lett.* **2010**, *10* (1), 239–242.

(84) Tong, S. W.; Mishra, N.; Su, C. L.; Nalla, V.; Wu, W.; Ji, W.; Zhang, J.; Chan, Y.; Loh, K. P. High-Performance Hybrid Solar Cell Made from CdSe/CdTe Nanocrystals Supported on Reduced Graphene Oxide and PCDTBT. *Adv. Funct. Mater.* **2013**, *24* (13), 1904–1910.

(85) Lim, J.; Lee, D.; Park, M.; Song, J.; Lee, S.; Kang, M. S.; Lee, C.; Char, K. Modular Fabrication of Hybrid Bulk Heterojunction Solar Cells Based on Breakwater-like CdSe Tetrapod Nanocrystal Network Infused with P3HT. *J. Phys. Chem. C* **2014**, *118* (8), 3942–3952.

(86) Ko, S. H.; Lee, D.; Kang, H. W.; Nam, K. H.; Yeo, J. Y.; Hong, S. J.; Grigoropoulos, C. P.; Sung, H. J. Nanoforest of Hydrothermally Grown Hierarchical ZnO Nanowires for a High Efficiency Dye-Sensitized Solar Cell *Nano Lett.*, **2011**, 11 (2), 666–671.

(87) Liu, B.; Zhang, J.; Wang, X.; Chen, G.; Chen, D.; Zhou, C.; Shen, G. Hierarchical Three-Dimensional $ZnCo_2O_4$ Nanowire Arrays/Carbon Cloth Anodes for a Novel Class of High-Performance Flexible Lithium-Ion Batteries. *Nano Lett.*, **2012**, 12 (6), 3005–3011.

(88) Song, J.; Lim, J.; Lee, D.; Thambidurai, M.; Kim, J. Y.; Park, M.; Song, H.-J.; Lee, S.; Char, K.; Lee, C. Nanostructured Electron-Selective Interlayer for Efficient Inverted Organic Solar Cells. *ACS Appl. Mater. Interfaces* **2015**, *7* (33), 18460–18466.

(89) Radychev, N.; Lokteva, I.; Witt, F.; Kolny-Olesiak, J.; Borchert, H.; Parisi, J. Physical Origin of the Impact of Different Nanocrystal Surface Modifications on the Performance of CdSe/P3HT Hybrid Solar Cells *J. Phys. Chem. C*, **2011**, 115 (29), 14111–14122.

(90) Han, L.; Qin, D.; Jiang, X.; Liu, Y.; Wang, L.; Chen, J.; Cao, Y. Synthesis of High-Quality Zinc-Blende CdSe Nanocrystals and Their Application in Hybrid Solar Cells. *Nanotechnology* **2006**, *17* (18), 4736.

(91) Ren, S.; Chang, L.-Y.; Lim, S.-K.; Zhao, J.; Smith, M.; Zhao, N.; Bulović, V.; Bawendi, M.; Gradečak, S. Inorganic-Organic Hybrid Solar Cell: Bridging Quantum Dots to Conjugated Polymer Nanowires *Nano Lett.*, **2011**, 11 (9), 3998–4002.

(92) Hurst, M. N.; DeLong, R. K. Two-Dimensional Fluorescence Difference Spectroscopy to Characterize Nanoparticles and Their Interactions. *Sci. Rep.* **2016**, *6*.

(93) Lohse, S. E.; Burrows, N. D.; Scarabelli, L.; Liz-Marzán, L. M.; Murphy, C. J. Anisotropic Noble Metal Nanocrystal Growth: The Role of Halides. *Chem. Mater.* **2014**, *26* (1), 34–43.

(94) Sun, Y.; Xia, Y. Shape-Controlled Synthesis of Gold and Silver Nanoparticles. *Science* **2002**, *298* (5601), 2176–2179.

(95) Baghbanzadeh, M.; Carbone, L.; Cozzoli, P. D.; Kappe, C. O. Microwave-Assisted Synthesis of Colloidal Inorganic Nanocrystals. *Angew. Chem. Int. Ed.* **2011**, *50* (48), 11312–11359.

(96) Dallinger, D.; Kappe, C. O. Microwave-Assisted Synthesis in Water as Solvent. *Chem. Rev.* **2007**, *107* (6), 2563–2591.

(97) Meng, L.-Y.; Wang, B.; Ma, M.-G.; Lin, K.-L. The Progress of Microwave-Assisted Hydrothermal Method in the Synthesis of Functional Nanomaterials. *Mater. Today Chem.* **2016**, *1–2*, 63–83.

(98) Garrett, E. T.; Pei, Y.; Lowe, A. B. Microwave-Assisted Synthesis of Block Copolymer Nanoparticles via RAFT with Polymerization-Induced Self-Assembly in Methanol. *Polym. Chem.* **2015**, *7* (2), 297–301.

(99) Ma, M.-G.; Zhu, J.-F.; Zhu, Y.-J.; Sun, R.-C. The Microwave-Assisted Ionic-Liquid Method: A Promising Methodology in Nanomaterials. *Chem. – Asian J.* **2014**, *9* (9), 2378–2391.

(100) Mirzaei, A.; Neri, G. Microwave-Assisted Synthesis of Metal Oxide Nanostructures for Gas Sensing Application: A Review. *Sens. Actuators B Chem.* **2016**, *237*, 749–775.

(101) Kappe, C. O.; Dallinger, D.; Murphree, S. S. *Practical Microwave Synthesis for Organic Chemists: Strategies, Instruments, and Protocols*; John Wiley & Sons, 2008.

(102) Siramdas, R.; McLaurin, E. J. InP Nanocrystals with Color-Tunable Luminescence by Microwave-Assisted Ionic-Liquid Etching *Chem. Mater.* **2017**, *29* (5), 2101–2109.

Chapter 2 - Microwave-Assisted Synthesis and Assembly of Hyperbranched supra Quantum Dot CdE (E = S, Se, Te) Nanocrystals

2-1 Introduction

Asymmetric heterostructures of semiconductor nanocrystalline materials _ so-called quantum dots (QDs) _ are ideal candidates for photocatalysis[1,2] and other light-driven charge-transfer processes such as light-emitting diodes (LEDs),[3–5] solar cells,[6–8] displays,[4,5,9] field-effect transistors,[10,11] photodetectors,[12] and lasers.[10,13,14]

Size-tunable optoelectronic properties are frequently highlighted as a desirable feature of QDs and formation of alloys and heterostructures provides additional optoelectronic tunability.[4,13,15,16] Asymmetric structures offer electronic tunability as well as more complicated changes in material properties due to changes in crystallinity and surface area. During the last decade dichalcogenides have attracted more attention as precursors for the synthesis of metal compounds of all group VI elements.[17-18] They have several advantages over the other precursors such as phosphine, urea or silyl based chalcogenide and dissolved sulfur and selenium in organic solvents. For example, relatively weak E−E bonds make them suitable for synthesis at lower reaction temperatures. However, their reactivity can be tuned by changing the organic substituents.[17,18]

Dichalcogenides have been used to synthesize nanocrystals of different ternary, quaternary, and quinary metal chalcogenide such as $ZnSe_{1-x}S_x$,[19] $Cu_2ZnSn(SSe)_4$,[20] $Cu_2CdSn(S_{1-x}Se_x)_4$, $Sn_xGe_{1-x}Se$, $Cu_{2-x}S_ySe_{1-y}$, Cu_2SnSe_3, and $CuFeSe_2$.[18] But there are just a few studies on the

reaction of mixtures of dichalcogenides. Guo et al. demonstrated that the reactivity and kinetics of the reaction of dichalcogenides depend on their C−E and E−E bond strengths. Guo and coworkers showed that in a mixture of Ph_2S_2 with Ph_2Se_2 and Me_2S_2, Ph_2S_2 works as a ligand. They demonstrated that differences in dichalcogenides reactivity result in NCs with different morphologies.[17] Generally, the bond dissociation energies of sulfur bonds are higher than of those of selenium and significantly higher than of those of tellurium congeners.[21] Among different alkyl disulfides of their study, Me_2S_2 has the strong C−S bonds and yields CdS tetrapods through an anisotropic growth pathway. Among other results also found that Ph_2Se_2 reacts faster than Me_2S_2 and gives spherical CdSe.[17]

Microwave-assisted synthesis is used widely in the synthesis of both organic and inorganic materials.[22–26] Among inorganic NCs microwave-assisted synthesis has been used mostly for metal oxides and is less popular for semiconductor NCs synthesis due to their delicate synthetic procedures which needs air and moisture free condition.[15,24,27] Microwave heating can generate very fast heating similar to the hot-injection method in which at high-temperature precursors injected into the reaction mixture and narrow size-distribution particles can be obtained in the case of the of II-VI NCs.[27,28]

Hyperbranched structures are observed mostly in noble metal NCs[29–35] and less for semiconductor NCs. Kanaras et al. reported the synthesis of highly crystalline hyperbranched CdSe and CdTe NCs using dissolved Se and Te powders in tri-n-octylphosphine (TOP). Hyperbranched snowflake CdTe NCs resulted from the growth of the new arms on previously formed arms and starlike CdSe particles from the growth of the new arms from the center of the original arm and aligned with the initial arms.[36]

Self-assembly and oriented attachments of NCs lead to formation of new structures as well.[19,37–42] Park and coworkers reported the formation of massive supra QDs CdS, CdSe, CdTe and CdSeTe using TOP solution of related chalcogenide. In their study, spherical NCs are made through self-assembly of small zinc blend spherical QDs.[37] In our previous work, we showed the formation of hyperbranched $ZnSe_{1-x}S_x$ NCs using dichalcogenides as the precursor. Our study showed that hyperbranched nanostructures formed from oriented attachment of zinc blend spherical NCs and unlike tetrapod structures in which the arms have wurtzite structure,[43–46] in that study, after formation of arms also the branched structures had zinc blend structure .[19]

Microwave-assisted synthesis of hyperbranched $CdSe_{1-x}S_x$ NCs using dichalcogenide precursors in the microwave-transparent solvent has been demonstrated. Structures varied from spherical NCs with diameters of ~4 nm to large, hyperbranched NCs with diameters approaching 200 nm. Synthetic conditions were adapted from a previous report of NC synthesis using single dichalcogenide precursors, forming binary materials. Moreover, microwave synthesis provides a sealed reaction environment which prevents loss of gases and volatile chemicals or intermediates. Microwave conditions tolerate high pressures (up to 30 bar) allowing the use of lower-boiling solvents, such as decane, but octadecene was also used for comparison.

In this chapter we will address/answer the following questions:

I. Can we synthesis branched hetrostructure NCs in a single step reaction using a mixture of precursors with different reactivities?

II. What is the shape evolution mechanism for the formation of branched NCs?

III. Is it possible to tune the morphology of NCs by controlling the reaction conditions?

2-2 Results and Discussions

2-2-1 Microwave-Assisted Synthesis of CdSeS NCs

In our previous study, we synthesized Mn:ZnSeS with different composition and morphologies using a mixture of Me_2S_2 and Ph_2Se_2 and NCs via hot-injection method. Our study showed that hyperbranched NCs results from nucleation and aggregation on NCs and changing the ratio of dichalcogenides affect the size of initial NCs.[19] In that case, due to doping purpose of the study, a different solvent was used and also lower reactivity of Zn(II), reaction carried out at a higher temperature. Here we study the microwave-assisted reaction of $Cd(oleate)_2$ with a mixture of Me_2S_2 and Ph_2Se_2 in a sealed reaction vessel.

As described by Vela and coworkers reaction of $Cd(oleate)_2$, with Ph_2Se_2 forms spherical CdSe NCs, but Me_2S_2 has less reactivity and gives tetrapod CdS NCs after 40 minutes.[17] Our microwave synthesis of CdSe shows that reaction happen faster, and yields a high amount of $CdSe_{1-x}S_x$ NCs (Figure 2-1), but Vela et al. reported Ph_2Se_2 hardly react with $Cd(oleate)_2$[17]. As the reaction conditions and solvents are the same for both the CdSe and the CdS synthesis, we studied the microwave-assisted reaction of $Cd(oleate)_2$ and a mixture of Ph_2Se_2 to Me_2S_2.

Among different dichalcogenides, these two were selected because they give alloy/heterostructures and also based on their different reactivity. Our hypothesis was the more reactive Ph_2Se_2 gives spherical CdSe NCs, and the less reactive Me_2S_2 gives tetrapod arms in a more alloyed fashion than the standard core-shell hot-injection approach[43,47]. $CdSe_{1-x}S_x$ NCs were synthesized in a set of reactions of $Cd(oleate)_2$ with dichalcogenides mixtures containing a different ratio of Ph_2Se_2 to Me_2S_2, where the overall ratio of $Cd(oleate)_2$ to dichalcogenides kept same (1:1). In case of pure Me_2S_2 the yield of the reaction was very low, but as the portion of Ph_2Se_2 in dichalcogenide mixture increased, more NCs obtained.

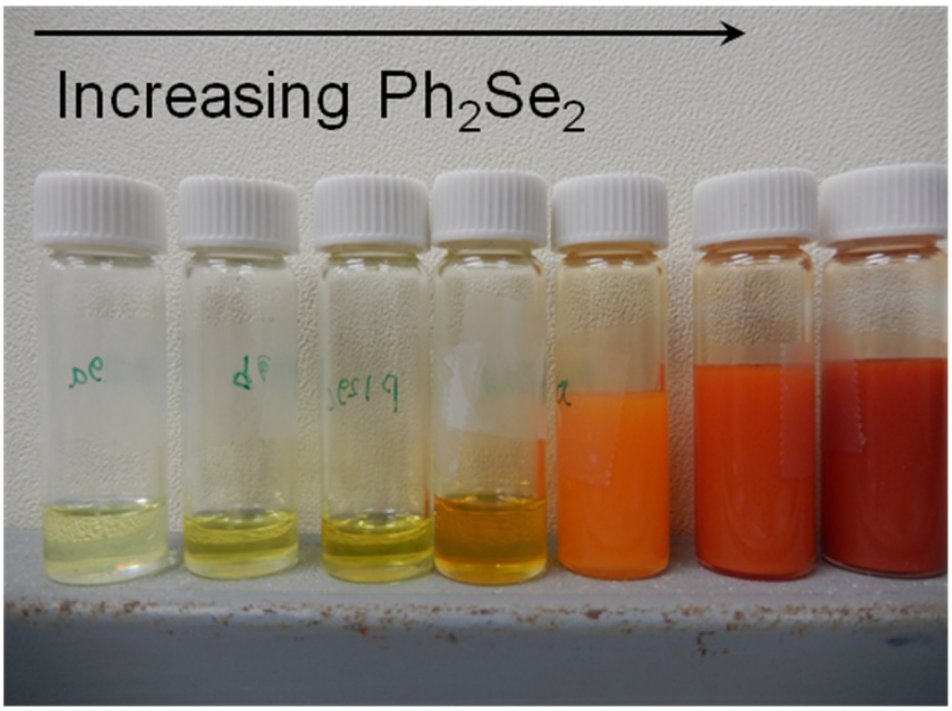

Figure 2-1 Image of NCs obtained from different ratio of Me_2S_2 and Ph_2Se_2, more NCs obtained from reactions with higher amount of Ph_2Se_2

Considering the combination of chalcogenide precursors and the radical mechanism of dichalcogenide conversion to the relevant chalcogenide anion,[17] cross-reaction between dichalcogenides is probable. This prevents the formation of pure CdSe cores with CdS shells or arms, but, considering the higher reactivity of Ph_2Se_2, the selenium content is expected to be higher at early stages of $CdSe_{1-x}S_x$ NCs formation (x is more close to unity). Over time, since the concentration of selenium precursor decreases, the Ph_2Se_2 content decreases and the composition of the NCs shifts to CdS.

2-2-2 Ratio Dependence

Figure 2-2 shows the UV-Vis absorption spectra and X-Ray diffraction (XRD) patterns of NCs obtained from reactions with different ratios of Ph_2Se_2 to Me_2S_2. In Figure 2-2a, the first absorption feature red-shift with increasing the ratio of Ph_2Se_2, suggesting formation of alloyed NCs with different compositions. It can be seen that the addition of small amount of Ph_2Se_2, (1%, 3%, 6%) causes a considerable shift in the first absorption peak feature but the shift for 70% to 100% is small. The reason for the shift is the difference in reactivity of precursors. As it mentioned, the yield of reaction in case of the pure Ph_2Se_2 is high but for pure Me_2S_2 is low. As a result, the ratio of Se in the composition of NCs obtained from reaction mixtures containing 1%, 3%, 6% Ph_2Se_2 will be higher than those of reaction mixture. The XRD patterns in figure 2-2b are broadened _which indicates the small size of NCs_ and shift of XRD peaks also indicates that the red-shift in absorption spectra to higher wavelengths by increasing the Ph_2Se_2 ratio is mainly due to the increase of Se portion in the composition of $CdSe_{1-x}S_x$. In the case of the pure Me_2S_2 and the mixtures containing 1% and 3% Ph_2Se_2, not enough NCs for XRD analysis obtained.

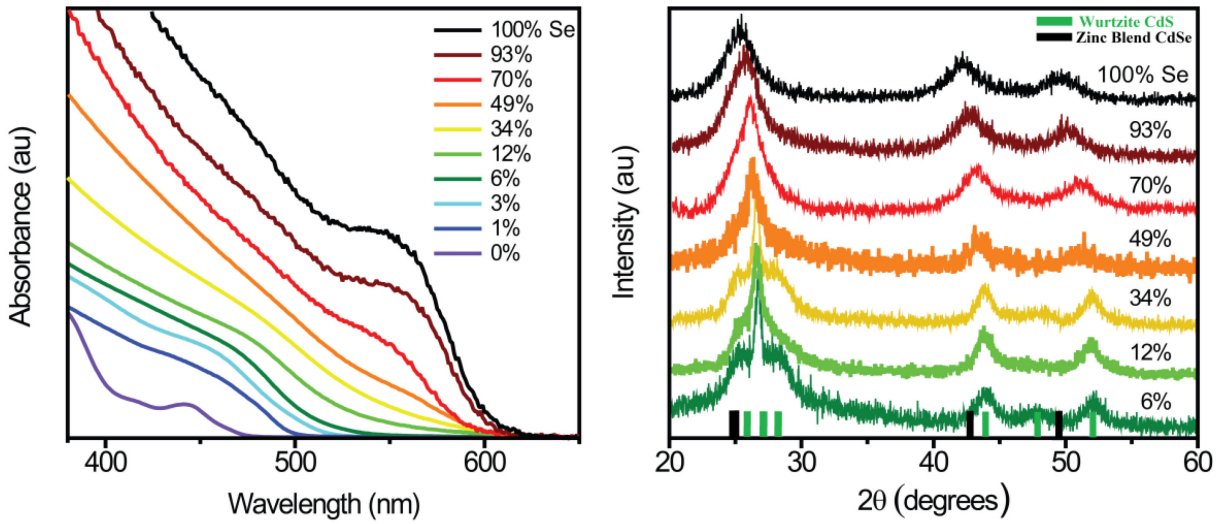

(a) (b)

Figure 2-2 Characterization of $CdSe_{1-x}S_x$ nanocrystals. (A) Absorption spectra of NCs with varying amounts of Se and S. As the amount of Se increases, the absorption feature red-shifts and narrows. (B) XRD of NCs with varying amounts of Se and S. As the amount of Se decreases, hexagonal features appear in the XRD pattern indicating wurtzite structure.

The XRD pattern of NCs further suggests the presence of ternary NCs. The peak positions are between those of CdS and CdSe. The broadened peak suggests NCs with poor crystallinity. High-resolution transmission electron microscopy (HRTEM) of the NCs shows that there are several crystal domains in each NC (Figure 2-3). Based on Scherrer analysis, average domain size of ~7 nm (±2 nm) is obtained for samples formed under varying conditions.

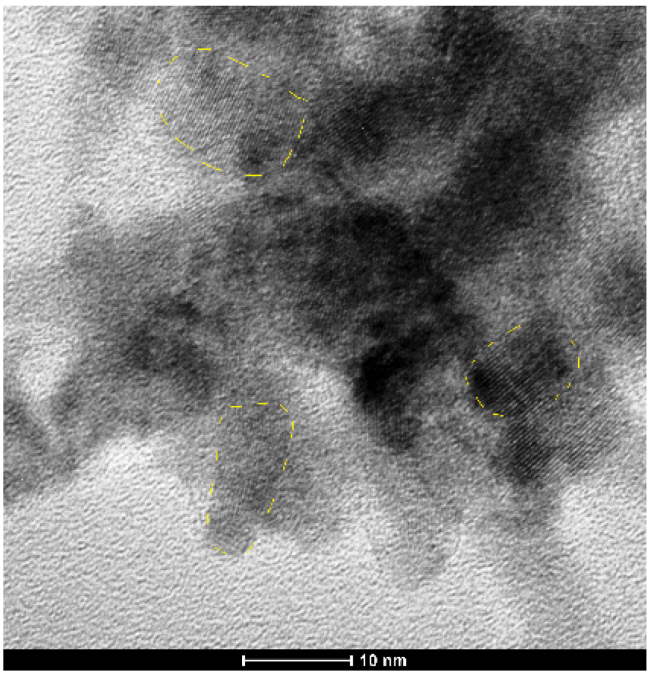

Figure 2-3 HRTEM image of HSQDs obtained from dichalcogenides with 12% Ph_2Se_2.

The XRD patterns show that CdSe NCs obtained from Ph_2Se_2 exhibits Zinc blend structure[48] (JCPDS file No. 19-0191), and CdS NCs obtained from Me_2S_2 has Wurtzite structure[49] (JCPDS files No. 06-0314 and 02-0563) which is an agreement with the previous study[17]. The crystalline

structure of $CdSe_{1-x}S_x$ is dependent to the ratio of the precursors and more closely resembles the chalcogenide with the higher ratio. Since S^{2-} and Se^{2-} have similar ionic radii (0.17 nm and 0.18 nm respectively), they readily substitute in the crystal lattice.[50] The gradual shift in XRD peaks positions indicates a gradual change in NC composition, which is due to the similar lattice parameter of CdS and CdSe crystals.[50]

Figure 2-4 shows TEM images of the NCs obtained from reactions with different ratios of Me_2S_2 to Ph_2Se_2. The shape and morphology of the NCs changes with the ratio of dichalcogenides. It was previously shown that the bond dissociation energy of S^{2-} and Se^{2-} precursors controls the shape of the NCs by regulation of reaction kinetics.[17]

Spherical NCs with zinc blend structure form from reaction of $Cd(oleate)_2$ with Ph_2Se_2. In the case of Me_2S_2, the concentration of reactive reactants is low in the reaction mixture due to its low reactivity. This causes kinetically controlled growth in which growth takes place on the more active, the 100 facet of the initially formed seeds, forming of arms with wurtzite structure,[17] as indicated by XRD pattern. On the other hand, the low concentration of reactive precursors limits the nucleation and results a reaction mixture with a lower number of seeds.[51] In reactions with mixtures of sulfur and selenium precursors, the composition, crystal structure, shape and morphology of NCs depends on the ratio of chalcogenide reactants. Figures 2-4a-c show that the shape of the NCs obtained from reactions with low fractions of Ph_2Se_2 (up to about 6%) are similar to CdS NCs and increasing the amount of Ph_2Se_2 increases the aggregation of NCs. The arm length of NCs obtained from reaction with 6% Ph_2Se_2 is about 40 nm (Figure 2-4).

Hyperbranched supra quantum dots (HSQDs) which are highly branched large NCs in which the arms-length are about 25 nm (Figure 2-5) are obtained in the reaction with 12% Ph_2Se_2 (Figure 2-4d).

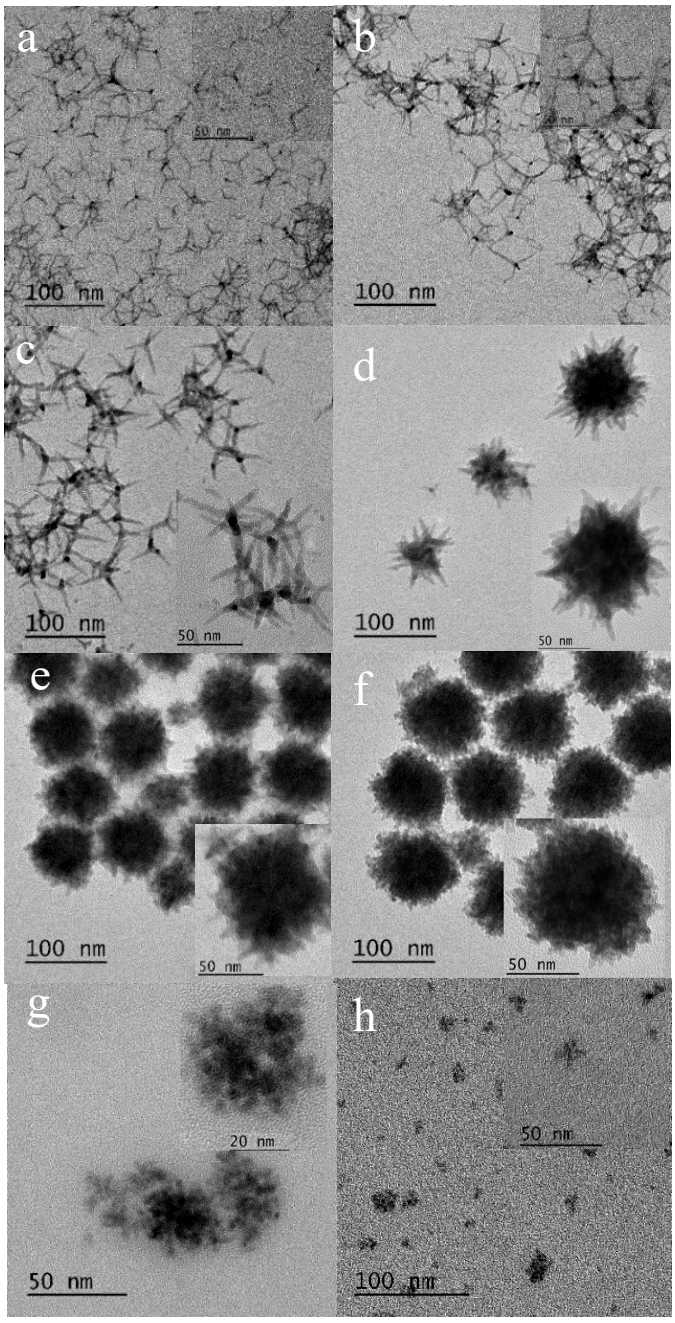

Figure 2-4 TEM images of NCs from reactions with 0, 3, 6, 12, 34, 49, 70 and 100% of Ph_2Se_2 respectively. In the absence of Ph_2Se_2, CdS tetrapod nanocrystals are formed (a); Increasing the amount of Ph_2Se_2 to 6% forms NCs with simple branched structure, but they are more aggregated (c); Mixture with 12% Ph_2Se_2 yields hyperbranched NCs (d); Further increasing the ratio of Ph_2Se_2, causes the arms to shrink until reaction with 70% of selenium precursor gives aggregated spherical NCs (e-g); Finally,

reaction of Cd oleate with just Ph_2Se_2 gives CdSe spheres QDs and aggregates (h). Insets highlight particles that are linking together, likely through oriented attachment, to form larger networks and aggregates of the NCs.

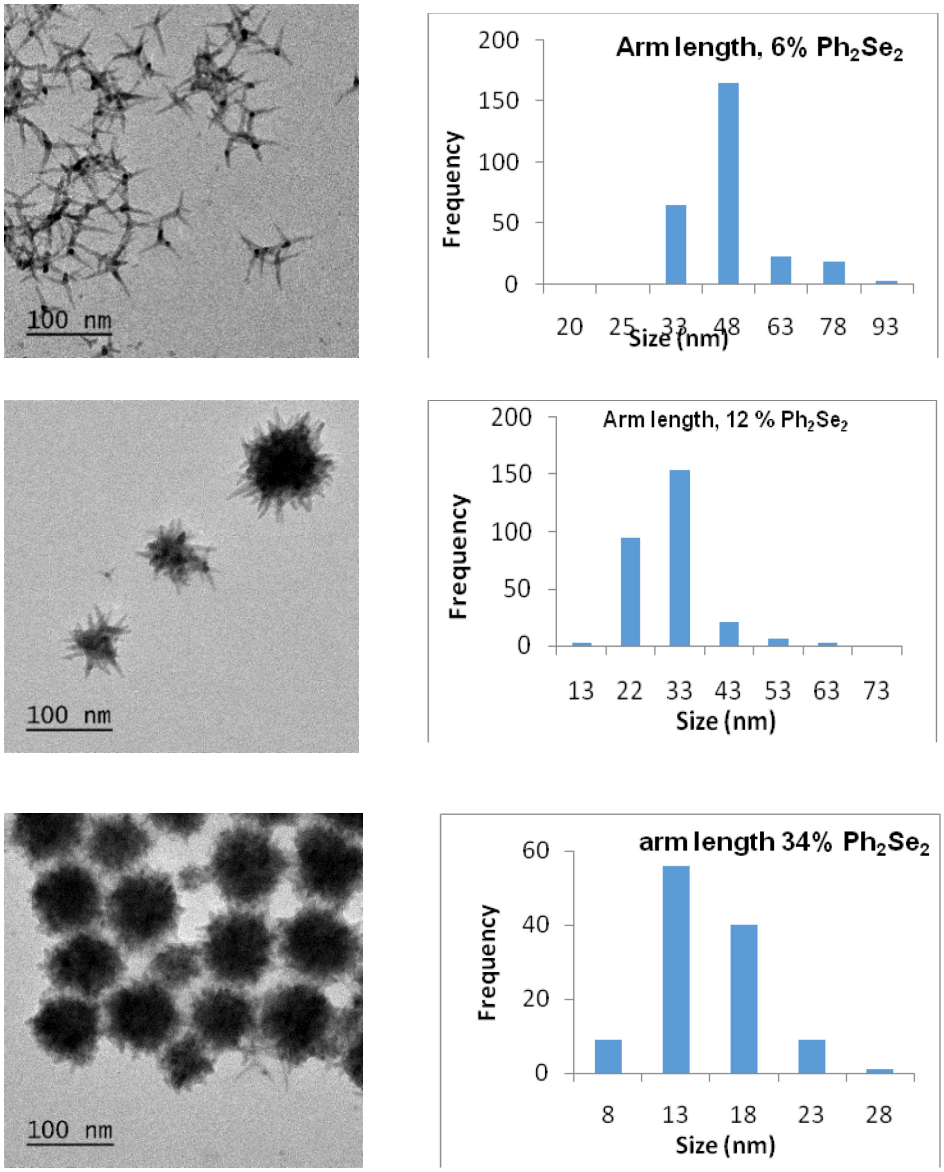

Figure 2-5 TEM image and histogram of arm length of NCs obtained from samples with 6%, 12% and 34% Ph_2Se_2.

Figures 2-4e and 2-4f show that by increasing the ratio of Ph_2Se_2, aggregated zinc blend NCs with smaller arms (as shown in Figure 2-5, the in case of 34% Ph_2Se_2 the arm length is 13 nm) are obtained indicating arms with wurtzite structure result from the reaction of $Cd(oleate)_2$ with Me_2S_2. At very high ratios of Ph_2Se_2, the NCs form from aggregation of spherical NCs (Figures 2.4g and 2.4h).

2-2-3 Shape evolution mechanism

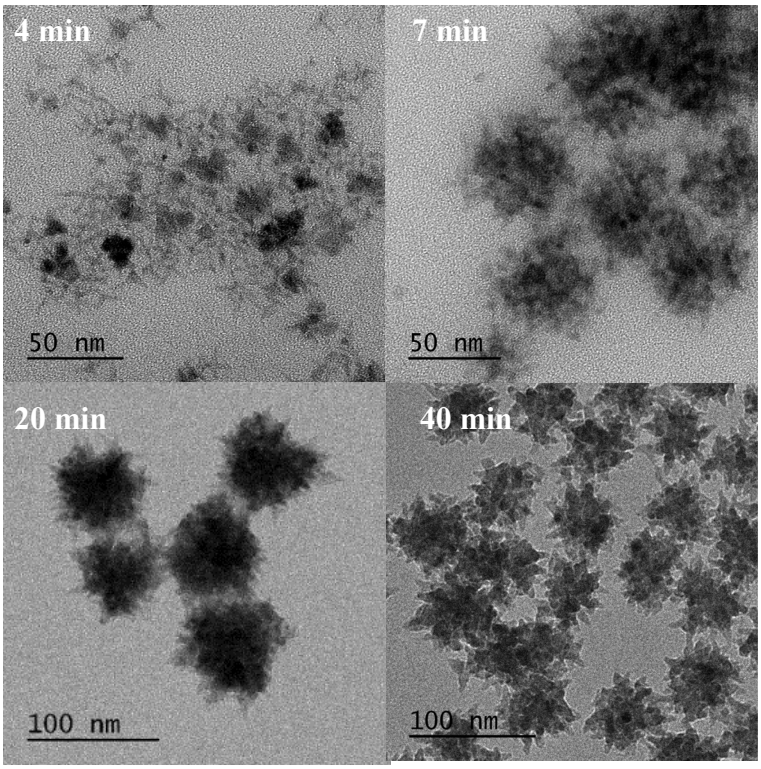

Figure 2-6 TEM image of NCs obtained from reactions with different times at 250 ˚C with 12% Ph_2Se_2. Initially, simple branched NCs form. The NCs aggregate over time and growth of the arms leads to the formation of HSQDs .

As mentioned, formation of NCs with hyperbranched morphology through branching of initial NCs or oriented attachment of small NCs are reported before. To find the shape evolution mechanism of HSQDs, a set of reactions with 12% Ph_2Se_2 and different reaction time were placed. Monitoring the reaction over time reveals that initial NCs are simply branched and tend to aggregate over time (Figure 2-6). UV-Vis spectra show that initial particles absorb at lower wavelengths and overtime shifts to higher wavelengths due to increasing size of the NCs (Figure 2.7).

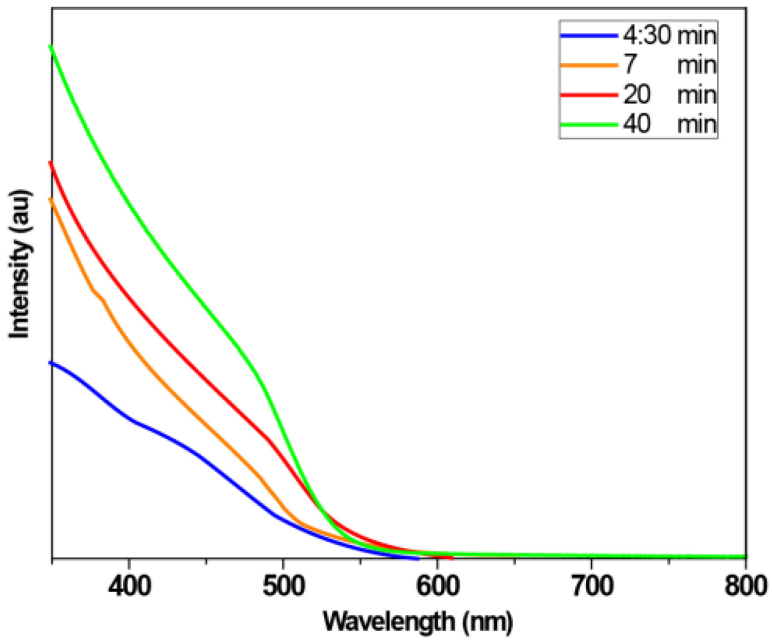

Figure 2-7 . UV-Vis spectrum of NCs obtained from dichalcogenides with 12% Ph_2Se_2 over time.

To further study the shape evolution mechanism reactions of $Cd(oleate)_2$ with 10% Ph_2Se_2 mixture at 250 ˚C _ which is regular temperature_ and 295 ˚C were studied. The selected ratio seems to be binary with simple branched QDs and HSQDs and gives both individual branched NCs and aggregated hyperbranched NCs. (Figure 2-8)

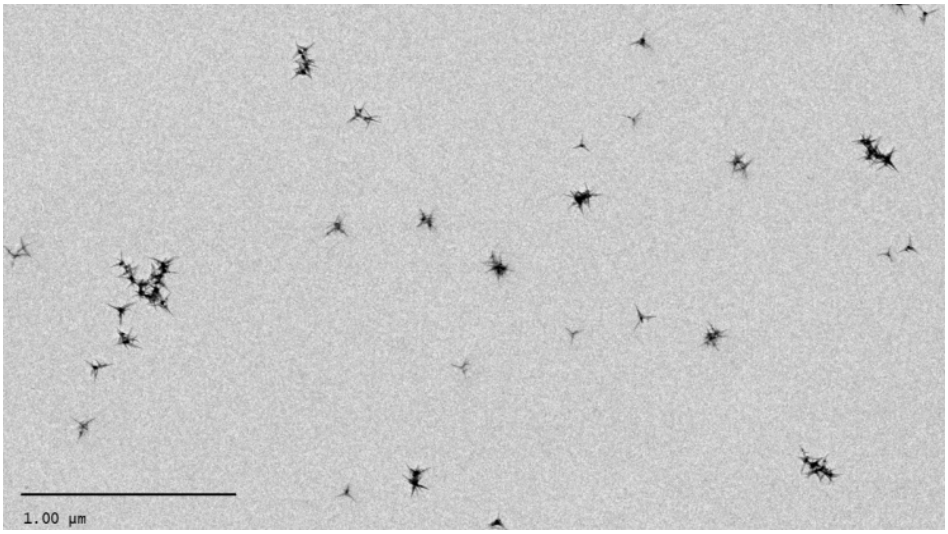

Figure 2-8 . Individual and aggregated branched NCs obtained from 10% Ph_2Se_2

So we performed reactions at different temperature and reactants concentrations to study the possibility of setting the reaction condition toward the formation of individual branched NCs and aggregated hyperbranched NCs. Figure 2-9 shows UV-Vis absorption and TEM images of the NCs. In the case of the diluted reaction mixture at 250 ˚C, UV-Vis absorption is similar to heterogeneous CdSe/CdS core-shells[43].

Absorption feature at above 650 nm is related to the $CdSe_{1-x}S_x$ with x close to unity and the absorption feature at 450 nm (Figure 2-10) is from CdS arms.[43] This is confirmed by d spacing measurement of HRTEM image of arms which is 0.336 nm, which is related to the (002) planes of CdS (Figure 2-11). In the case of other reactions, no distinguished absorption features for the formation of CdSe@CdSe core/shell structure[44,52,53] observed in the UV-Vis spectra.

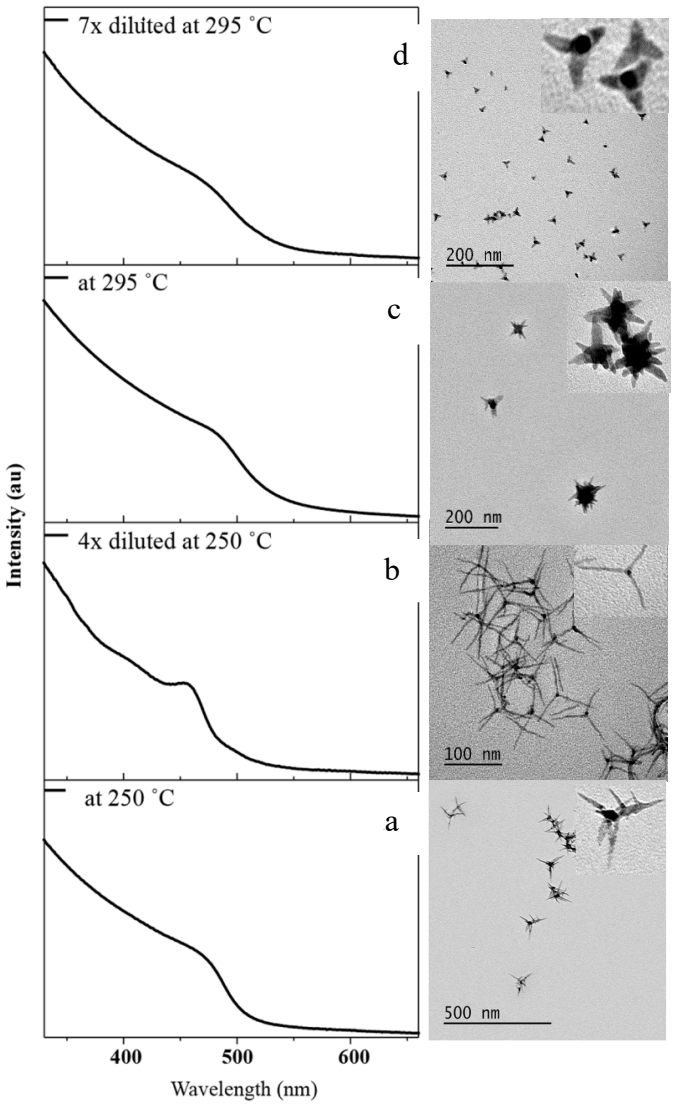

Figure 2-9 . UV-Vis spectrum and TEM images of NCs obtained from reaction of a dry mixture of oleic acid and oleylamine and other reactants at a) 250 ˚C, b) 250 ˚C 4x diluted c) 295 ˚C, and d) 295 ˚C 7x diluted

TEM images reveal complementary information for observed spectra. As shown in Figures 2-8 and 2-9a, the reaction at 250 ˚C gives both individual and aggregated branched NCs. In comparison, because of the higher precursor conversion rate at higher temperature, the higher

concentration of active precursors boosts the formation of cores at the beginning of the reaction, increasing the aggregation of the initial simple-branched NCs and forms HSQDs.

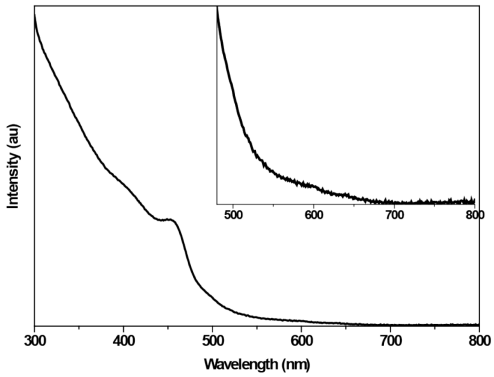

Figure 2-10 UV-Vis spectrum of NCs obtained from reaction of diluted mixture at 250 ˚C.

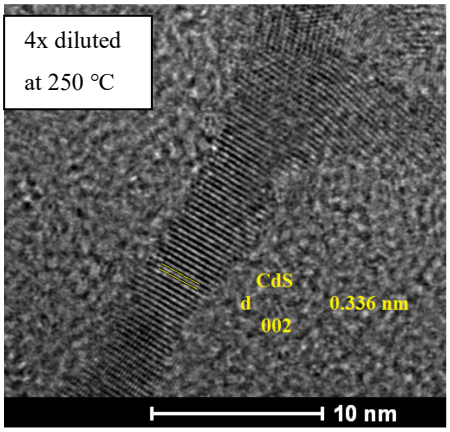

Figure 2-11 HRTEM image of NCs obtained from reaction of diluted mixture containing 10% Ph_2Se_2 at 250 ˚C.

Dilution of the reaction mixture separates the cores and decreases aggregation. Study of the reaction of the diluted mixture reveals details of kinetically controlled growth of the arms of the NCs. As shown in Figures 2-12, the arms of the NCs obtained from reactions at high and low temperatures have aspect ratios (arm length /diameter) of 7.27 nm and 1.65 nm respectively.

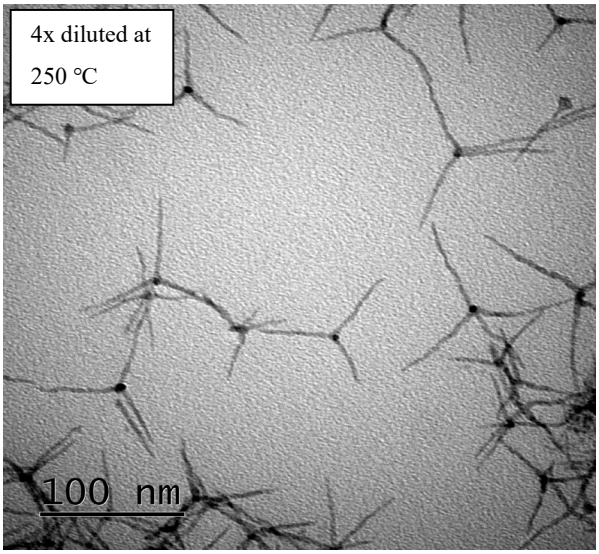

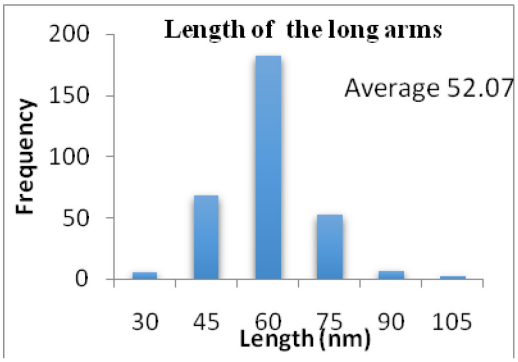

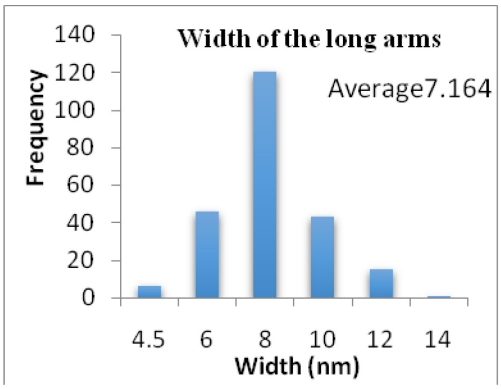

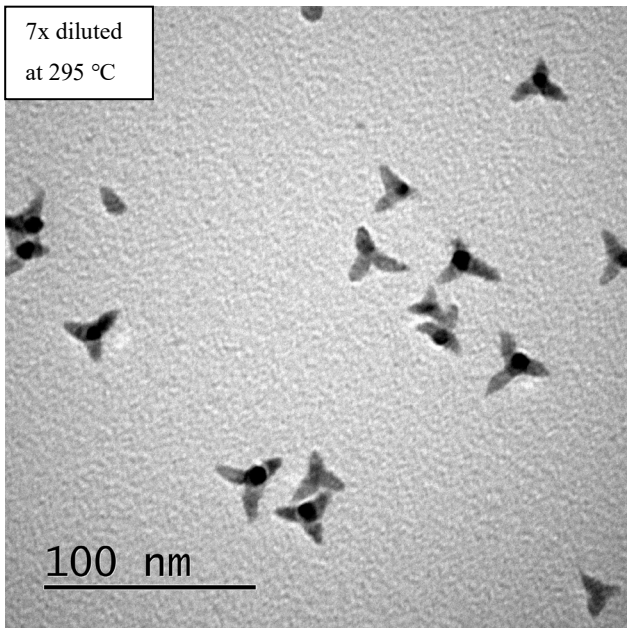

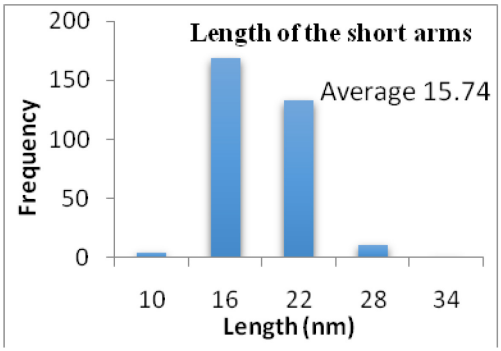

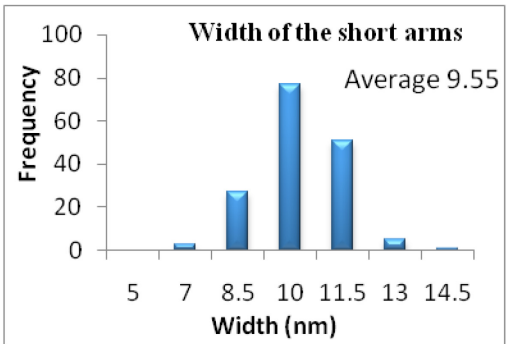

Figure 2-12. TEM images and histogram of arms length and thickness of NCs obtained from samples 10% Ph_2Se_2 at different temperatures.

In the case of the diluted reaction mixture reacted at 250 ˚C, the reaction rate is low, and since the reaction mixture is diluted, the concentration of active precursors is low enough for anisotropic growth at the most reactive $(000\bar{1})$-facet. Moreover, at low temperature, growth on the less reactive side facets such as the $(11\bar{2}0)$- and $(10\bar{1}0)$-facets is slow, yielding formation of long, thin arms.[51] Reaction at high temperature yields short and thick arms. Higher reaction temperature affects the reaction in two ways. First, it increases the conversion rate of dichalcogenides resulting higher concentration of the active precursors and second, it causes higher reactivity of the side facets. These two promote growth at side facets and gives NCs with shorter but thicker arms.[51]

Scheme 1 shows the proposed shape evolution mechanism of NCs. The reaction of $Cd(oleate)_2$ with Me_2S_2 or Ph_2Se_2 gives tetrapodal and spherical particles respectively. In the case of mixtures of chalcogenide precursors, nucleation of NCs at the beginning of the reaction is related to the amount of the more reactive Ph_2Se_2 in the reaction mixture and epitaxial growth is related to the amount of Me_2S_2. When the amount of Ph_2Se_2 is about 12% or more, plentiful nuclei form and slow reaction of Me_2S_2 yields gradual growth of the arms. Meanwhile, the high concentration of particles increases the aggregation and, along with the ongoing growth of the arms, gives HSQDs (Figure 2-4). At higher percentages of selenium precursor, the amount of Me_2S_2 is less and consequently, the arms are smaller. Alternatively, increasing the amount of Ph_2Se_2 leads to the formation of more cores and subsequently increases the number of arms and intensifies the reduction of the arms size. These two factors_ the decrease in the amount of Me_2S_2 and an increase in the number of arms_ shorten the size of the arms significantly (Figure 2-4). Dilution of the reaction mixture, prevent aggregation of NCs and by tuning the temperature, the kinetics of the reaction can be controlled (Figure 2-9).

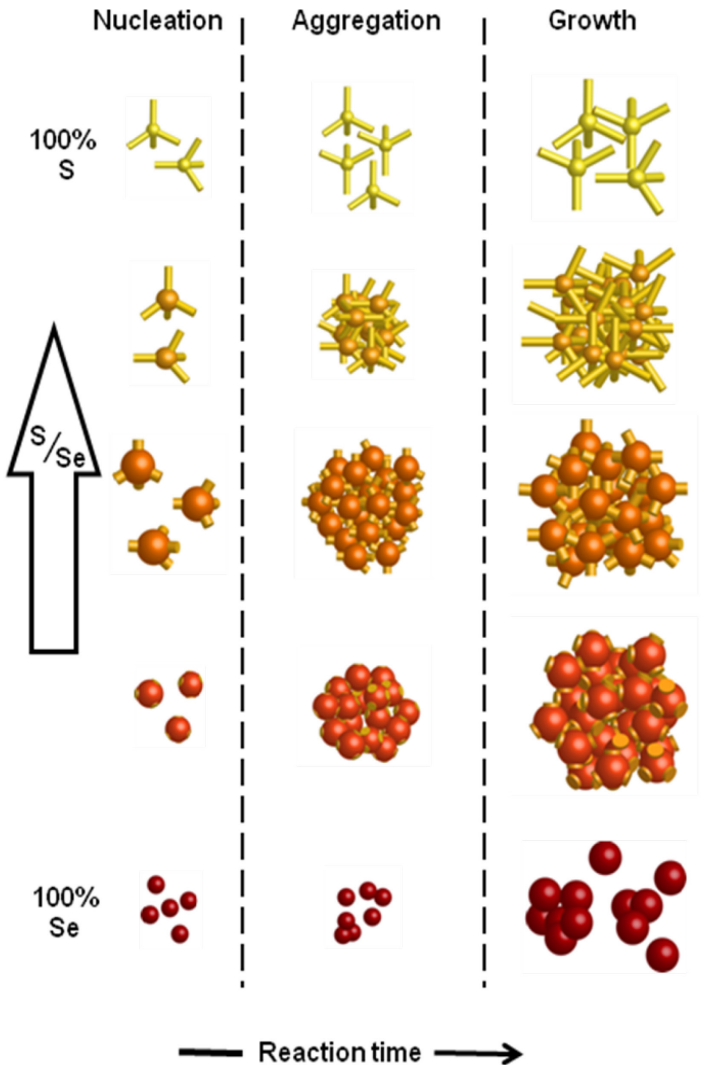

Scheme 1. Formation of NCs with different shapes and morphologies by varying the ratios of Se and S precursors. Higher ratios of Me_2S_2 tend to form branched NCs, and more Ph_2Se_2 gives spherical NCs. Since Ph_2Se_2 is more reactive, it forms the initial cores for arm growth. Increasing the ratio of Ph_2Se_2 precursors yields more cores, and subsequently more platforms for arms, and decreasing the ratio of S precursor gives smaller arms.

Spontaneous assembly and self-organization of tetrapods can occur in different ways, but for oriented attachment, adjoining tetrapods need to share crystallographic facets with complementary _ if not identical _ lattice parameters.[54–56] This study shows that tetrapods assemble mostly through side-to-side bonding and tip-to-tip is less likely to happen, indicating that strong van der Waals interactions are the aggregation driving force.[54] Figure 2-4h shows that aggregation driving force is low for small spherical CdSe NCs.

To check the effect of Me_2S_2 on the morphology of NCs, $Cd(oleate)_2$ was reacted with a mixture of Ph_2Se_2 and Ph_2S_2 with 1:1 ratio. The absorption spectrum feature at 550 nm (Figure 2-13) shows that the composition of the NCs is similar to CdSe NCs obtained from the reaction of $Cd(oleate)_2$ with Ph_2Se_2 (Figure 2-2a) and XRD pattern of particles shows formation of zinc blend CdSe NCs (Figure 2-14).

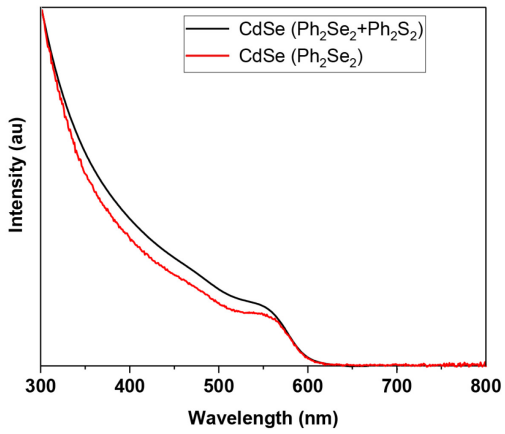

Figure 2-13 UV-Vis spectra of CdSe NCs obtained from reaction of $Cd(oleate)_2$ with Ph_2Se_2 and mixture of Ph_2Se_2 and Ph_2S_2.

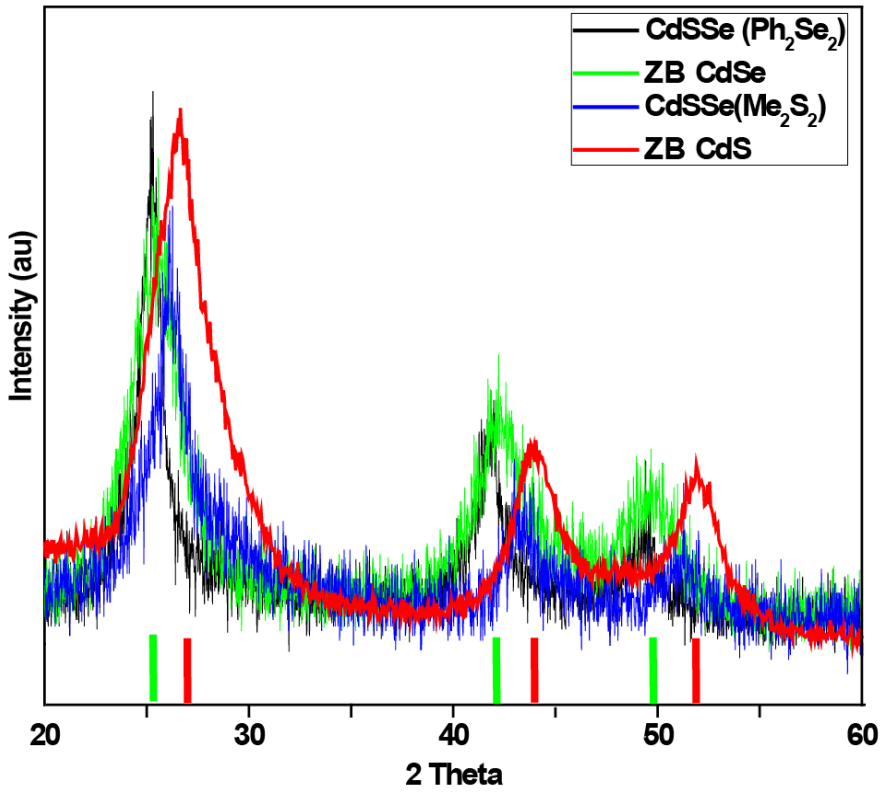

Figure 2-14 XRD pattern of CdS (JCPDS files No. 06-0314 and 02-0563), CdSe (JCPDS file No. 19-0191) compared with CdSeS NCs obtained from Me_2S_2 and Ph_2S_2 as source of sulfur.

As reported previously,[17] Ph_2S_2 is not a good source for S^{2-} since the S-C bond is too strong (BDE 69.75 kcal/mol)[17] to break in these reactions. However, low BDE of S-S bond (24.11 kcal/mol)[17] leads its dissociation and formation of thiophenol radicals that works as capping ligands as it observed in TEM image, the shape and morphology of NCs are similar to NCs obtained from 100% Ph_2Se_2 (Figure 2-15).

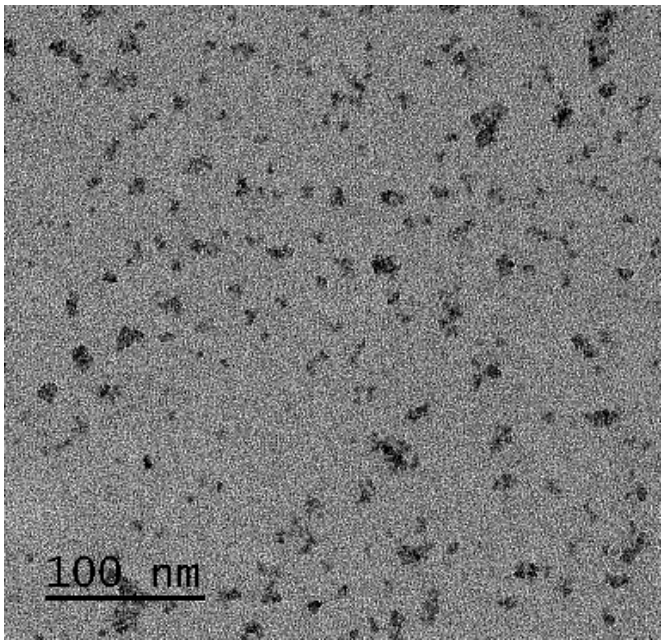

Figure 2-15 TEM image of CdSe NCs obtained from reaction of $Cd(oleate)_2$ with 1:1 ratio mixture of Ph_2Se_2 and Ph_2S_2.

Besides providing homogenous heating, microwave synthesis uses a sealed reaction vessel which prevents loss of volatile reactants or reaction intermediates. Performing the synthesis in a sealed reactor under pressure makes it possible to use solvents with boiling temperatures below the reaction temperature. For instance, decane and mineral spirits are not suitable solvents for conventional heating synthesis due to their low boiling temperatures which prevent the reaction from reaching the required synthesis temperature. Water generated from amide formation causes the same problem in the conventional synthesis and limit reactions with separately dried oleic acid and oleylamine which in case of this study, no NCs was obtained in conventional heating as the reaction temperature of didn't rich 250 ˚C.

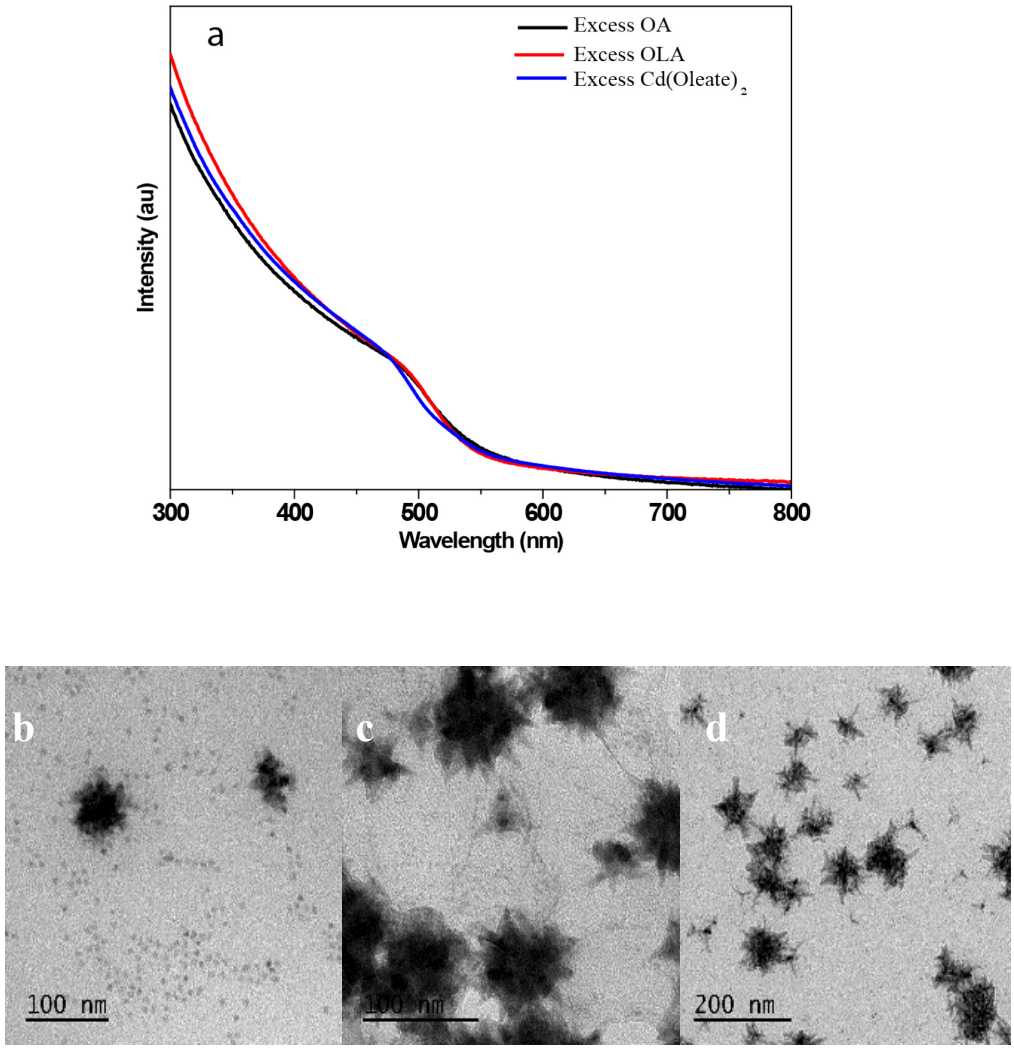

Figure 2-16 a) Uv-Vis spectra and TEM images of NCs obtained from reactions with an excess amount of b) O-acid, c) O-amine and d) $Cd(oleate)_2$

It is reported that different ligands have different capping ability which affects the shape of NCs especially their arms[44,47,57] and also their aggregation.[55,58] To study if any of the ligands have a specific effect on the shape of NCs, excess amounts of ligands were added to the reaction mixture. Figure 2-16a shows that the absorptions of NCs are very similar and have absorption features at about 480 nm which are very close to the absorption feature of synthesis without excess ligand which is about 480 nm as well (Figure 2-4a, 12% Ph_2Se_2). This indicates that NCs

has the same composition and excess ligand and $Cd(oleate)_2$ does not affect the conversion of dichalcogenides to their active forms. TEM images show that the overall morphologies of the NCs are the same, and in all cases HSQDs are formed but, the arm shapes are different (Figure 2-16b-d) which is agreement with previous reports on different capping ability of different ligands.[44,47,57] In case of excess oleic acid, a high number of non-aggregated spherical NCs are formed (Figure. 2-16b). Since oleic acid has a strong capping ability for CdS and CdSe NCs, using it in excess amount promotes the formation of non-aggregated NCs. [44,57]

2-2-4 Synthesis of telluride alloys

The procedure was used to synthesize CdTe, CdTeSe and CdTeS alloys as well. Figures 2-17 and 2-18 show the absorption and XRD pattern of NCs. In the case of the mixture of Ph_2Te_2 and Me_2S_2, no distinct absorption feature observed in UV-Vis absorption spectra of NCs, but the XRD peaks positions which are between those of CdTe and CdS indicates the formation of alloy nanoparticles. NCs obtained from the mixture of Ph_2Te_2 and Ph_2Se_2 have an absorption feature at about 685 nm which can be related to CdSe, CdTe or CdTeSe NCs.

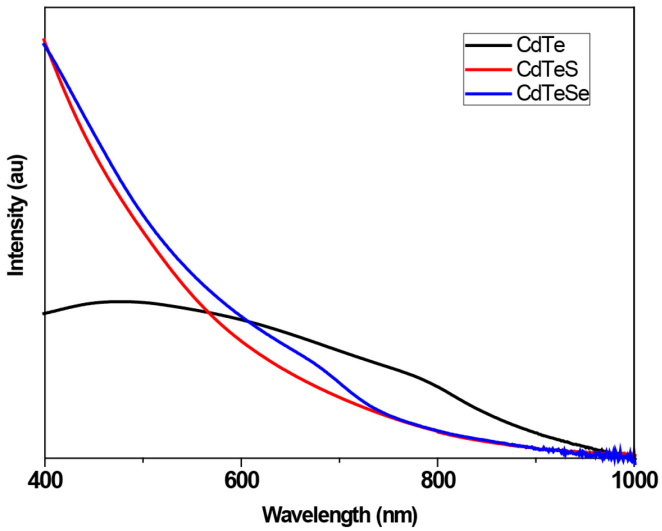

Figure 2-17 UV-Vis spectrum of CdTe, CdTeS and CdTeSe.

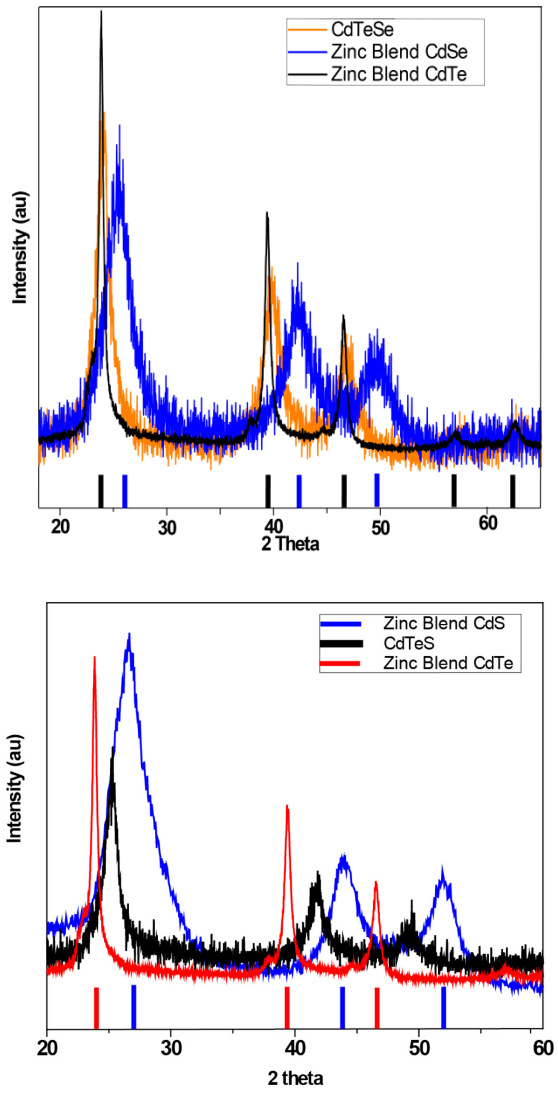

Figure 2-18 XRD pattern of CdS (JCPDS files No. 06-0314 and 02-0563), CdTeS, CdTeSe, CdSe (JCPDS file No. 19-0191) and CdTe (JCPDS files No. 15-0770) NCs

The XRD peaks are slightly shifted from those of CdTe. To confirm formation of alloy NCs,

Energy-dispersive X-ray spectroscopy (EDAX) study was performed on the NCs (Figure 2-19).

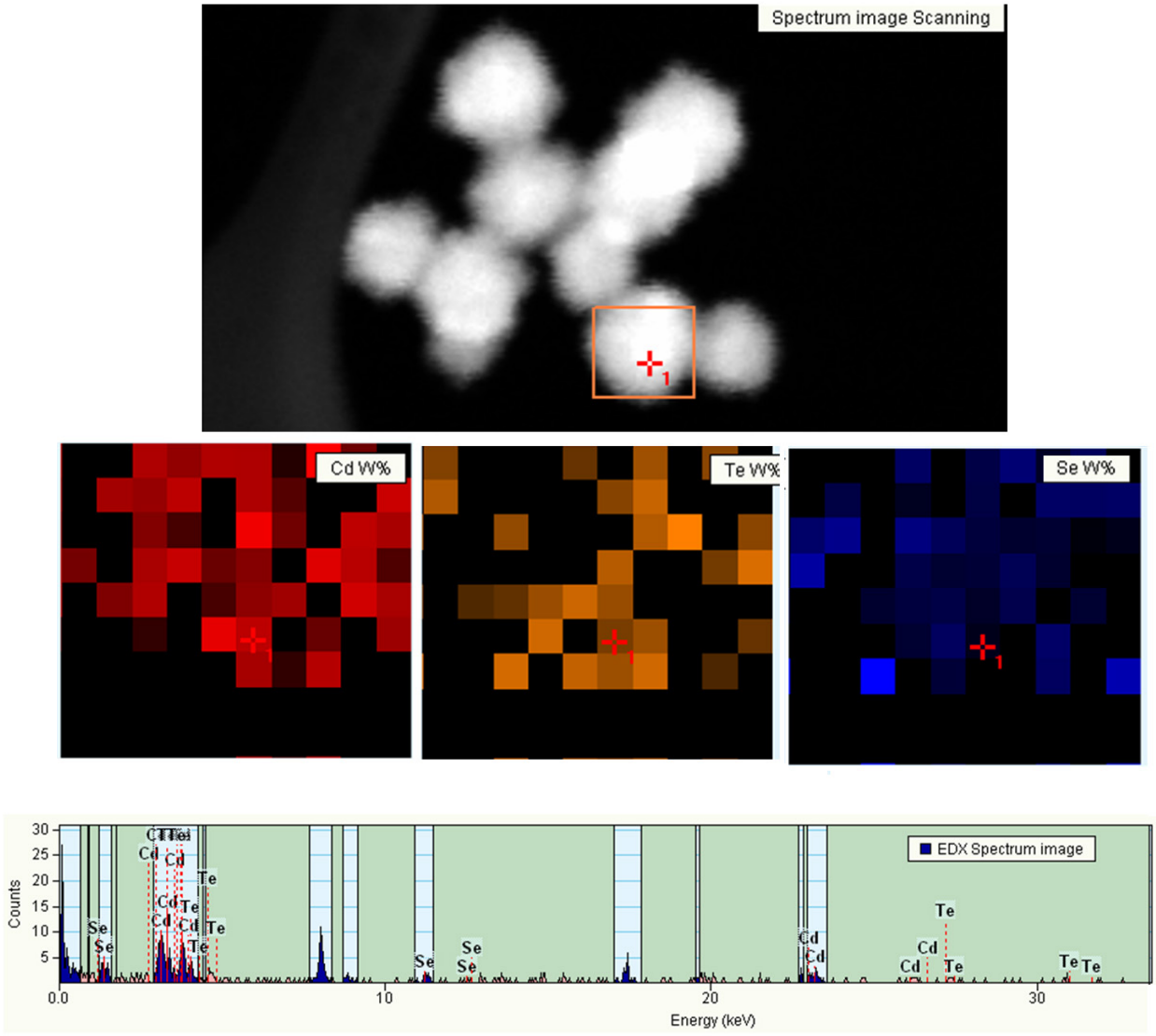

Figure 2-19 EDAX analysis of CdTeSe.

Figure 2-20 shows the TEM image of CdTe, CdTeS and CdTeSe nanocrystals. In general, both heteronuclear and homonuclear single bonds of tellurium have lower energy than those of their sulfur and selenium congeners[21]. For instance, BDE of E-E bonds of Ph_2S_2, Ph_2Se_2 and Ph_2Te_2 are 45.66 kcal/mol[17] 43.63 kcal/mol[17] and 31.6 kcal/mol[59] respectively. Due to higher reactivity

of Ph_2Te_2, the kinetics of the reactions and subsequently, the morphology of the NCs are different.

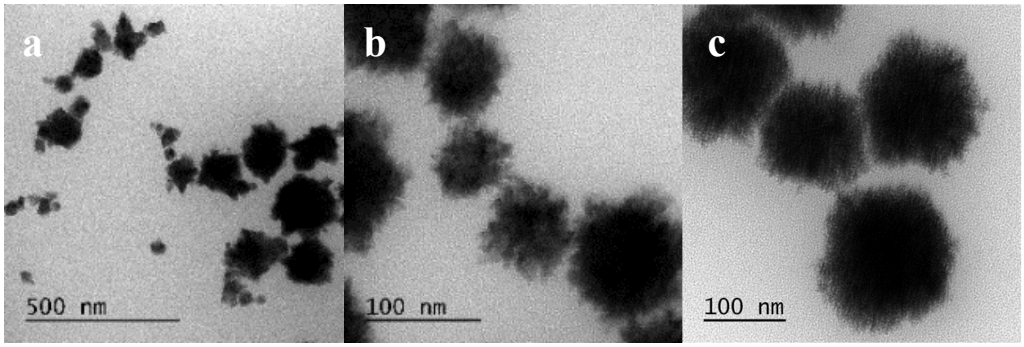

Figure 2-20. TEM image of a) CdTe, b) CdTeS and c) CdTeSe NCs

2-3 Summary

In summary, dimethyl disulfide, diphenyl diselenide and diphenyl ditelluride used to synthesize cadmium chalcogenide alloys in a single-step microwave-assisted synthesis. In the case of a mixture of precursors with different reactivity, the more reactive precursor determines the nucleation rate, number of particles, and subsequent aggregation of NCs and the less reactive precursor dictates the reaction growth period after the nucleation stage. HSQDs were successfully stabilized by optimizing the amount of ligands and solvents resulting in a highly branched NCs in which no two particles are exactly same but particles of very uniform with no formation of individual spherical or branched NCs. By knowing the chemistry of the precursors, combinations of precursors can be used to synthesize alloys with desired composition and morphology. Considering both precursors are in the reaction mixture we believe that cross-reaction causes a moderate composition shift and formation of a graded interface in core-shell structures.

2-4 Materials and Methods

All the chemicals listed below are commercially available and were used without further purification; oleylamine (OLA, ≥98%), oleic acid (OA, 90%), diphenyl diselenide (Ph_2Se_2, 99%), octadecene (ODE, 90%), toluene Bis(trimethylsilylmethyl) sulfide (≥99%) and decane, (≥99) from Aldrich; dimethyl disulfide (Me_2S_2, 99%), diphenyl disulfide (Ph_2S_2 ≥99%), diphenyl ditelluride (Ph_2Te_2, 97%), cadmium oxide (CdO, ≥99.0%) from Fluka and methanol (MeOH) from Acros.

2-4-1 Physical measurements

In this study, a Cary 500 UV-Vis-NIR spectrophotometer was used for recording UV-Vis absorption spectra. For transmission electron microscopy (TEM) analysis, a drop of sample was dried on a copper grid. TEM images were recorded using an FEI Tecnai G2 Spirit BioTWIN microscope. For high-resolution transmission electron microscopy (HRTEM), carbon grid and an FEI Tecnai F20 XT Field Emission Transmission Electron Microscope were used. Powder X-Ray diffraction (XRD) patterns were recorded using a PANalytical Empyrean multi-purpose X-Ray diffractometer.

2-4-2 Synthesis

The synthesis adopted from the previous study[17].

Stock solutions of Ph_2Se_2 (0.115 M in ODE and 0.0848 M in decane) were prepared by dissolving 0.238 g Ph_2Se_2 (0.76 mmol) in 5.20 g ODE, or 0.1456 g (0.465 mmol) in 4 .002 g decane.

A stock solution of Me_2S_2 (0.364 M in ODE and 0.41 M in decane) were prepared by dissolving 0.1996 g Me_2S_2 (2.13 mmol) in 4.62 g ODE, or 0.2093 g (2.23 mmol) in 4.016 g decane. 0.17 M Ph_2Te_2 stock solution was prepared by dissolving 1.00 g Pe_2Te_2 (2.44 mmol) in a mixture of 5.9 g toluene and 6.1 g ODE.

The reaction mixture can be prepared in two different ways. Different reaction mixture preparation can affect the synthesis because of the formation of water. In the first method, cadmium oxide (CdO), oleic acid (OA) and oleylamine (OLA) can be degassed all in one flask, heated to 180-220 ˚C to obtain a clear mixture following by degassing step again. The reaction mixture is then is moved to the glovebox. Alternatively, the solvents and reactant were degassed separately and moved to the glovebox. The later procedure produces more water as a result of the amidation reaction between oleylamine and oleic acid. In the first, since all ligands were heated together in $Cd(oleate)_2$ formation step, less amide formation takes place during the synthesis. Both procedures give NCs with similar UV-Vis absorption spectra but, reactions with water formation had less yield especially at shorter times. In this study, we used separately dried solvents and ligands.

To minimize variation in reagent concentrations, stock solutions were prepared for 8 reactions. In a flask, 0.2015 g CdO (1.56 mmol) and 10.51 g oleic acid (38 mmol) were degassed at 100 ˚C for 60 min and then under N_2, heated at 180 ˚C until a colorless solution was obtained. The mixture was cooled and degassed at 100 ˚C again and moved to the glovebox. Dry oleylamine (8.3 g, 31 mmol) and the desired amount of dichalcogenide stock solutions were added, and the mixture was stirred vigorously and used to study the effect of time at 250 ˚C. To study the effect of the ratio of dichalcogenides, $Cd(oleate)_2$ stock solution was prepared in the same way and 3 g of it was transferred to a microwave vial and an appropriate amount of dichalcogenides were

added to it. To study the effect of ODE, 7.6 g (30 mmol) of it was added to a Shilink flask during the $Cd(oleate)_2$ preparation step. To get a colorless mixture in the case of one step degassing of oleic acid and oleylamine mixture, during the $Cd(oleate)_2$ preparation step, the solution was heated to 220 ˚C and since the reaction forms a water, it cooled down and degassed at 100 ˚C and then, under N_2 atmosphere, heat to 220 ˚C and degassed at 100 ˚C again and then filled with N_2 and moved to glovebox. 3.3 g of the reaction mixture was poured in 10 ml microwave glass vial containing a stir bar and the reaction was heated using 2.4 GHz microwave irradiation at 800 W set-power and the desired temperature for different times. For the reactions at 295 ˚C, the reaction times were limited to a maximum 30 minutes by the instrument.

The CdS NCs with zinc blende structure were prepared in the same way except Bis(trimethylsilylmethyl) sulfide was used instead of Me_2S_2.

2-5 Conclusion

Our study showed that branched heterostructures NCs in one step reaction using precursors with different reactivities. The mechanism of shape evolution of NCs is demonstrated and it's shown that by controlling reaction conditions, NCs with desired shape can be synthesized. Synthesized NCs has no luminescence probably due to the unpassivated surface and defects of the structures.

2-6 References

(1) Eley, C.; Li, T.; Liao, F.; Fairclough, S. M.; Smith, J. M.; Smith, G.; Tsang, S. C. E. Nanojunction-Mediated Photocatalytic Enhancement in Heterostructured CdS/ZnO, CdSe/ZnO, and CdTe/ZnO Nanocrystals. *Angew. Chem. Int. Ed.* **2014**, *53* (30), 7838–7842.

(2) Amirav, L.; Alivisatos, A. P. Photocatalytic Hydrogen Production with Tunable Nanorod Heterostructures *J. Phys. Chem. Lett.*, **2010**, 1 (7), 1051–1054.

(3) Yang, Y.; Zheng, Y.; Cao, W.; Titov, A.; Hyvonen, J.; Manders, J. R.; Xue, J.; Holloway, P. H.; Qian, L. High-Efficiency Light-Emitting Devices Based on Quantum Dots with Tailored Nanostructures. *Nat. Photonics* **2015**, *9* (4), 259.

(4) Anikeeva, P. O.; Halpert, J. E.; Bawendi, M. G.; Bulović, V. Quantum Dot Light-Emitting Devices with Electroluminescence Tunable over the Entire Visible Spectrum. *Nano Lett.* **2009**, *9* (7), 2532–2536.

(5) Qian, L.; Zheng, Y.; Xue, J.; Holloway, P. H. Stable and Efficient Quantum-Dot Light-Emitting Diodes Based on Solution-Processed Multilayer Structures. *Nat. Photonics* **2011**, *5* (9), 543.

(6) Yang, Z.; Fan, J. Z.; Proppe, A. H.; Arquer, F. P. G. de; Rossouw, D.; Voznyy, O.; Lan, X.; Liu, M.; Walters, G.; Quintero-Bermudez, R.; et al. Mixed-Quantum-Dot Solar Cells. *Nat. Commun.* **2017**, *8* (1), 1325.

(7) Albero, J.; Clifford, J. N.; Palomares, E. Quantum Dot Based Molecular Solar Cells. *Coord. Chem. Rev.* **2014**, *263–264* (Supplement C), 53–64.

(8) Sargent, E. H. Colloidal quantum dot solar cells, *Nature Photon* **2012**, 6, 133–135.

(9) Kim, T.-H.; Cho, K.-S.; Lee, E. K.; Lee, S. J.; Chae, J.; Kim, J. W.; Kim, D. H.; Kwon, J.-Y.; Amaratunga, G.; Lee, S. Y.; et al. Full-Colour Quantum Dot Displays Fabricated by Transfer Printing. *Nat. Photonics* **2011**, *5* (3), 176.

(10) Schön, J. H.; Dodabalapur, A.; Kloc, C.; Batlogg, B. A Light-Emitting Field-Effect Transistor. *Science* **2000**, *290* (5493), 963–965.

(11) Talapin, D. V.; Murray, C. B. PbSe Nanocrystal Solids for N- and p-Channel Thin Film Field-Effect Transistors. *Science* **2005**, *310* (5745), 86–89.

(12) Sukhovatkin, V.; Hinds, S.; Brzozowski, L.; Sargent, E. H. Colloidal Quantum-Dot Photodetectors Exploiting Multiexciton Generation. *Science* **2009**, *324* (5934), 1542–1544.

(13) Klimov, V. I.; Mikhailovsky, A. A.; Xu, S.; Malko, A.; Hollingsworth, J. A.; Leatherdale, C. A.; Eisler, H.-J.; Bawendi, M. G. Optical Gain and Stimulated Emission in Nanocrystal Quantum Dots. *Science* **2000**, *290* (5490), 314–317.

(14) Vargas, A.; Liu, F.; Lane, C.; Rubin, D.; Bilgin, I.; Hennighausen, Z.; DeCapua, M.; Bansil, A.; Kar, S. Tunable and Laser-Reconfigurable 2D Heterocrystals Obtained by Epitaxial Stacking of Crystallographically Incommensurate Bi2Se3 and MoS2 Atomic Layers. *Sci. Adv.* **2017**, *3* (7), e1601741.

(15) Siramdas, R.; McLaurin, E. J. InP Nanocrystals with Color-Tunable Luminescence by Microwave-Assisted Ionic-Liquid Etching. *Chem. Mater.* **2017**, *29* (5), 2101–2109.

(16) Wei, G.; Czaplewski, D. A.; Lenferink, E. J.; Stanev, T. K.; Jung, I. W.; Stern, N. P. Size-Tunable Lateral Confinement in Monolayer Semiconductors. *Sci. Rep.* **2017**, *7* (1), 3324.

(17) Guo, Y.; Alvarado, S. R.; Barclay, J. D.; Vela, J. Shape-Programmed Nanofabrication: Understanding the Reactivity of Dichalcogenide Precursors. *ACS Nano* **2013**, *7* (4), 3616–3626.

(18) Brutchey, R. L. Diorganyl Dichalcogenides as Useful Synthons for Colloidal Semiconductor Nanocrystals. *Acc. Chem. Res.* **2015**, *48* (11), 2918–2926.

(19) S. Yazdanparast, M.; T. Webb, M.; J. McLaurin, E. Single-Step Synthesis of Hyperbranched, Luminescent Mn 2+ -Doped ZnSe 1−x S x Nanocrystals Using Dichalcogenide Precursors. *J. Mater. Chem. C* **2016**, *4* (28), 6907–6913.

(20) Singh, S.; Liu, P.; Singh, A.; Coughlan, C.; Wang, J.; Lusi, M.; Ryan, K. M. Colloidal Cu2ZnSn(SSe)4 (CZTSSe) Nanocrystals: Shape and Crystal Phase Control to Form Dots, Arrows, Ellipsoids, and Rods. *Chem. Mater.* **2015**, *27* (13), 4742–4748.

(21) Chivers, T.; S. Laitinen, R. Tellurium: A Maverick among the Chalcogens. *Chem. Soc. Rev.* **2015**, *44* (7), 1725–1739.

(22) Kappe, C. O.; Dallinger, D. Controlled Microwave Heating in Modern Organic Synthesis: Highlights from the 2004–2008 Literature. *Mol. Divers.* **2009**, *13* (2), 71.

(23) Kappe, C. O.; Dallinger, D. The Impact of Microwave Synthesis on Drug Discovery. *Nat. Rev. Drug Discov.* **2006**, *5* (1), 51.

(24) Dallinger, D.; Kappe, C. O. Microwave-Assisted Synthesis in Water as Solvent. *Chem. Rev.* **2007**, *107* (6), 2563–2591.

(25) Meng, L.-Y.; Wang, B.; Ma, M.-G.; Lin, K.-L. The Progress of Microwave-Assisted Hydrothermal Method in the Synthesis of Functional Nanomaterials. *Mater. Today Chem.* **2016**, *1–2*, 63–83.

(26) Ma, M.-G.; Zhu, J.-F.; Zhu, Y.-J.; Sun, R.-C. The Microwave-Assisted Ionic-Liquid Method: A Promising Methodology in Nanomaterials. *Chem. – Asian J.* **2014**, *9* (9), 2378–2391.

(27) Baghbanzadeh, M.; Carbone, L.; Cozzoli, P. D.; Kappe, C. O. Microwave-Assisted Synthesis of Colloidal Inorganic Nanocrystals. *Angew. Chem. Int. Ed.* **2011**, *50* (48), 11312–11359.

(28) Ramasamy, P.; Kim, N.; Kang, Y.-S.; Ramirez, O.; Lee, J.-S. Tunable, Bright, and Narrow-Band Luminescence from Colloidal Indium Phosphide Quantum Dots. *Chem. Mater.* **2017**, *29* (16), 6893–6899.

(29) Kang, Y.; Pyo, J. B.; Ye, X.; Diaz, R. E.; Gordon, T. R.; Stach, E. A.; Murray, C. B. Shape-Controlled Synthesis of Pt Nanocrystals: The Role of Metal Carbonyls. *ACS Nano* **2013**, *7* (1), 645–653.

(30) Pan, Y.; Guo, X.; Li, M.; Liang, Y.; Wu, Y.; Wen, Y.; Yang, H. Construction of Dandelion-like Clusters by PtPd Nanoseeds for Elevating Ethanol Eletrocatalytic Oxidation. *Electrochimica Acta* **2015**, *159*, 40–45.

(31) Ji Ye, S.; Youb Kim, D.; Wook Kim, D.; Ok Park, O.; Kang, Y. Facile Synthesis of Palladium Nanodendrites Supported on Graphene Nanoplatelets: An Efficient Catalyst

for Low Overpotentials in Lithium–Oxygen Batteries. *J. Mater. Chem. A* **2016**, *4* (2), 578–586.

(32) Dong, Z.; Le, X.; Dong, C.; Zhang, W.; Li, X.; Ma, J. Ni@Pd Core–Shell Nanoparticles Modified Fibrous Silica Nanospheres as Highly Efficient and Recoverable Catalyst for Reduction of 4-Nitrophenol and Hydrodechlorination of 4-Chlorophenol. *Appl. Catal. B Environ.* **2015**, *162*, 372–380.

(33) Feng, J.-J.; Liu, L.; Huang, H.; Wang, A.-J. Poly(Ionic Liquid)-Assisted One-Pot Synthesis of Au Hyperbranched Architectures for Enhanced SERS Performances. *Sens. Actuators B Chem.* **2017**, *238*, 91–97.

(34) Zhang, L.; Chen, D.; Jiang, Z.; Zhang, J.; Xie, S.; Kuang, Q.; Xie, Z.; Zheng, L. Facile Syntheses and Enhanced Electrocatalytic Activities of Pt Nanocrystals with {*hkk*} High-Index Surfaces. *Nano Res.* **2012**, *5* (3), 181–189.

(35) Zhang, W.; Lu, X. Morphology Control of Bimetallic Nanostructures for Electrochemical Catalysts. *Nanotechnol. Rev.* **2013**, *2* (5), 487–514.

(36) Kanaras, A. G.; Sönnichsen, C.; Liu, H.; Alivisatos, A. P. Controlled Synthesis of Hyperbranched Inorganic Nanocrystals with Rich Three-Dimensional Structures. *Nano Lett.* **2005**, *5* (11), 2164–2167.

(37) Park, J.; Jeong, S.; Bang, J.; Kim, B.; Doh, H.; Cho, S.; Hwang, S.; Kim, S. Formation and Stepwise Self-Assembly of Cadmium Chalcogenide Nanocrystals to Colloidal Supra-Quantum Dots and the Superlattices. *Chem. Mater.* **2016**, *28* (15), 5329–5335.

(38) José Dalmaschio, C.; Ribeiro, C.; Roberto Leite, E. Impact of the Colloidal State on the Oriented Attachment Growth Mechanism. *Nanoscale* **2010**, *2* (11), 2336–2345.

(39) Boneschanscher, M. P.; Evers, W. H.; Geuchies, J. J.; Altantzis, T.; Goris, B.; Rabouw, F. T.; Rossum, S. A. P. van; Zant, H. S. J. van der; Siebbeles, L. D. A.; Tendeloo, G. van; et al. Long-Range Orientation and Atomic Attachment of Nanocrystals in 2D Honeycomb Superlattices. *Science* **2014**, 1252642.

(40) Bahrig, L.; G. Hickey, S.; Eychmüller, A. Mesocrystalline Materials and the Involvement of Oriented Attachment – a Review. *CrystEngComm* **2014**, *16* (40), 9408–9424.

(41) Ge, J.; Hu, Y.; Biasini, M.; Beyermann, W. P.; Yin, Y. Superparamagnetic Magnetite Colloidal Nanocrystal Clusters. *Angew. Chem. Int. Ed.* **2007**, *46* (23), 4342–4345.

(42) Lv, W.; He, W.; Wang, X.; Niu, Y.; Cao, H.; H. Dickerson, J.; Wang, Z. Understanding the Oriented-Attachment Growth of Nanocrystals from an Energy Point of View: A Review. *Nanoscale* **2014**, *6* (5), 2531–2547.

(43) Talapin, D. V.; Nelson, J. H.; Shevchenko, E. V.; Aloni, S.; Sadtler, B.; Alivisatos, A. P. Seeded Growth of Highly Luminescent CdSe/CdS Nanoheterostructures with Rod and Tetrapod Morphologies. *Nano Lett.* **2007**, *7* (10), 2951–2959.

(44) Mishra, N.; Wu, W.-Y.; Srinivasan, B. M.; Hariharaputran, R.; Zhang, Y.-W.; Chan, Y. Continuous Shape Tuning of Nanotetrapods: Toward Shape-Mediated Self-Assembly. *Chem. Mater.* **2016**, *28* (4), 1187–1195.

(45) Manna, L.; Milliron, D. J.; Meisel, A.; Scher, E. C.; Alivisatos, A. P. Controlled Growth of Tetrapod-Branched Inorganic Nanocrystals. *Nat. Mater.* **2003**, *2* (6), 382–385.

(46) Lim, J.; Bae, W. K.; Park, K. U.; zur Borg, L.; Zentel, R.; Lee, S.; Char, K. Controlled Synthesis of CdSe Tetrapods with High Morphological Uniformity by the Persistent Kinetic Growth and the Halide-Mediated Phase Transformation. *Chem. Mater.* **2013**, *25* (8), 1443–1449.

(47) Manna, L.; Milliron, D. J.; Meisel, A.; Scher, E. C.; Alivisatos, A. P. Controlled Growth of Tetrapod-Branched Inorganic Nanocrystals. *Nat. Mater.* **2003**, *2* (6), 382–385.

(48) Mohamed, M. B.; Tonti, D.; Al-Salman, A.; Chemseddine, A.; Chergui, M. Synthesis of High Quality Zinc Blende CdSe Nanocrystals. *J. Phys. Chem. B* **2005**, *109* (21), 10533–10537.

(49) Chen, M.; Xie, Y.; Lu, J.; Xiong, Y.; Zhang, S.; Qian, Y.; Liu, X. Synthesis of Rod-, Twinrod-, and Tetrapod-Shaped CdS Nanocrystals Using a Highly Oriented Solvothermal Recrystallization Technique. *J. Mater. Chem.* **2002**, *12* (3), 748–753.

(50) Kim, J.-P.; Christians, J. A.; Choi, H.; Krishnamurthy, S.; Kamat, P. V. CdSeS Nanowires: Compositionally Controlled Band Gap and Exciton Dynamics. *J. Phys. Chem. Lett.* **2014**, *5* (7), 1103–1109.

(51) Lim, J.; Bae, W. K.; Park, K. U.; zur Borg, L.; Zentel, R.; Lee, S.; Char, K. Controlled Synthesis of CdSe Tetrapods with High Morphological Uniformity by the Persistent Kinetic Growth and the Halide-Mediated Phase Transformation. *Chem. Mater.* **2013**, *25* (8), 1443–1449.

(52) Deka, S.; Falqui, A.; Bertoni, G.; Sangregorio, C.; Poneti, G.; Morello, G.; Giorgi, M. D.; Giannini, C.; Cingolani, R.; Manna, L.; et al. Fluorescent Asymmetrically Cobalt-Tipped CdSe@CdS Core@Shell Nanorod Heterostructures Exhibiting Room-Temperature Ferromagnetic Behavior. *J. Am. Chem. Soc.* **2009**, *131* (35), 12817–12828.

(53) Zhou, C.; Chen, Q.; Wang, G.; Guan, A.; Xu, J.; Liu, X.; Shi, Z.; Zhou, L. One-Pot Synthesis of CdSe@CdS Core@shell Quantum Dots and Their Photovoltaics Application in Quantum-Dot-Sensitized ZnO Nanorods. *J. Photochem. Photobiol. Chem.* **2017**, *332*, 251–257.

(54) R. Franchini, I.; Cola, A.; Rizzo, A.; Mastria, R.; Persano, A.; Krahne, R.; Genovese, A.; Falqui, A.; Baranov, D.; Gigli, G.; et al. Phototransport in Networks of Tetrapod -Shaped Colloidal Semiconductor Nanocrystals. *Nanoscale* **2010**, *2* (10), 2171–2179.

(55) Park, J.; Jeong, S.; Bang, J.; Kim, B.; Doh, H.; Cho, S.; Hwang, S.; Kim, S. Formation and Stepwise Self-Assembly of Cadmium Chalcogenide Nanocrystals to Colloidal Supra-Quantum Dots and the Superlattices. *Chem. Mater.* **2016**, *28* (15), 5329–5335.

(56) Sinkovits, D. W.; Luijten, E. Nanoparticle-Controlled Aggregation of Colloidal Tetrapods. *Nano Lett.* **2012**, *12* (4), 1743–1748.

(57) Mishra, N.; Orfield, N. J.; Wang, F.; Hu, Z.; Krishnamurthy, S.; Malko, A. V.; Casson, J. L.; Htoon, H.; Sykora, M.; Hollingsworth, J. A. Using Shape to Turn off Blinking for Two-Colour Multiexciton Emission in CdSe/CdS Tetrapods. *Nat. Commun.* **2017**, *8*, 15083.

(58) Ko, W. Y. L.; Bagaria, H. G.; Asokan, S.; Lin, K.-J.; Wong, M. S. CdSe Tetrapod Synthesis Using Cetyltrimethylammonium Bromide and Heat Transfer Fluids. *J. Mater. Chem.* **2010**, *20* (12), 2474–2478.

(59) Joo, S.-W. Te-Te Cleavage of Aromatic Ditellurides on Silver and Gold Surfaces. *J. Raman Spectrosc.* **2006**, *37* (11), 1244–1247.

Chapter 3 - Single-step synthesis of hyperbranched, luminescent Mn^{2+}-doped $ZnSe_{1\_x}S_x$ nanocrystals using dichalcogenide precursors

3.1 Introduction

Mn^{2+}-doped semiconductors are widely used in many photo and electroluminescent applications.[1,2] The availability of luminescent colloidal nanocrystals (NCs) of these materials expanded their use to bioimaging and sensing,[3–5] and solar energy,[6–8] among other applications.[9,10] The nature of the Mn^{2+} dopants can provide a probe of local environment, elucidating NC structural information via their optical and magnetic properties.[11–14] Applications involving Mn^{2+} phosphorescence involve doping of wide bandgap semiconductors.[15] The fixed $^4T_1$ energy level of the Mn^{2+} provides a trap for energy absorbed by the NC. This energy is released radiatively as an orange luminescence. This is only observed when the conduction band energy level is above the energy of the Mn^{2+} $^4T_1$, and thus frequently the zinc chalcogenides are employed as host materials.[3,13,15–18]

Dichalcogenides, namely diorganyl dichalcogenides, have recently been revived as synthons in colloidal NC syntheses.[19–22]

They are touted for their ability to provide access to unfavourable crystal phases,[19] resulting in a myriad of NC shapes, compositions, and properties.[20–22] Their reactivity can be tuned by changing the organic substituents, allowing formation of quantum dots, tetrapods, nanorods, and other asymmetric, hyperbranched NCs from nearly identical reaction conditions.[20] Hyperbranched and asymmetric semiconductor nanocrystals have large surface-area-to-volume ratios often resulting in a large number of surface defects.[23,24] Both of these characteristics garner

interest for use of these NCs for selective, efficient catalysis,[25] gas adsorption and sensing,[26] and defect-related luminescence.[27]

Luminescent Mn^{2+}-doped chalcogenide NCs are readily synthesized using colloidal methods.[15,16] Protocols using binary clusters,[28,29] multi-step shell additions,[12] and post-synthetic diffusion[30] have been established. Each method provides advantages and disadvantages, such that the synthetic method can be chosen depending on the application requirements. Overall, these methods have multiple steps often involving reactive, expensive precursors, and the products of these syntheses have been limited in scope. This is ascribed to the difficulty in doping transition metal ions into anisotropic NCs.[31,32] Although there are numerous reports of emissive Mn^{2+}-doped spherical NCs and even nanorods,[33–39] there are only two reports of luminescent asymmetric Mn^{2+}-doped NCs.[32,40] In the detailed work of Wu & Warner, luminescent Mn^{2+}-doped ZnSe NCs were synthesized with spherical and pod-like structures. The branching is ascribed to polymorphism, resulting in tetrapods, with average sizes of 15 nm.[24,40] A sophisticated, successful effort to obtain asymmetric luminescent Mn^{2+}-doped NCs was presented by Yao et al. in which a one-pot synthesis generated elongated doped NCs exhibiting Mn^{2+} emission. The worm-like shapes and defects support an oriented-attachment-type growth of these 4−10 nm long particles.[32,41,42] Here we report the first example, to the best of our knowledge, of luminescent Mn^{2+}-doped hyperbranched NCs. Zinc chalcogenides were chosen to exploit the characteristic luminescence observed from the Mn^{2+} $^4T_1$ - $^6A_1$ transition. Changing the dichalcogenide precursors resulted in different morphologies, with compositions varying with precursor ratios. An electron paramagnetic resonance (EPR) signal is observed for the NCs, providing additional evidence for doping and information about the NC structure. This simple procedure provides a new synthetic method for successful incorporation of Mn^{2+} in wide bandgap

$ZnSe_{1-x}S_x$ semiconductor NCs using dichalcogenide precursors. The incorporation of a radiative defect allows luminescence to be observed from these materials.

In this chapter we will address/answer following questions:

I. Can we synthesis doped branched hetrostructure NCs in a single step reaction?

II. What is the shape evolution mechanism of NCs?

III. Does branche NCs show same application potential as non-branched NCs?

3-2 Experimental section

3-2-1 Materials

All the following chemicals are commercially available and were used without further purification; Manganese(II) acetate tetrahydrate ($Mn(OAc)_2 \cdot 4H_2O$, ≥99%), manganese (II) chloride tetrahydrate ($MnCl_2 \cdot 4H_2O$, 99.99%),oleylamine (OLA, ≥98%),stearic acid (SA, ≥95%), dodecane thiol (DDT, ≥98%), selenium (≥99.5%), tetramethylammonium chloride (NMe_4Cl, ≥98%),trimethylamine (TEA), cyclohexane, and toluene from Aldrich, diphenyl diselenide (Ph_2Se_2, 99%), dimethyl disulfide (Me_2S_2, 99%),phenylselenol (PhSeH, 98%), and methanol (MeOH) from Acros,zinc nitrate hexahydrate ($Zn(NO_3)_2 \cdot 6H_2O$) from J. T. Baker,and zinc undecylenate ($Zn(Un)_2$) from Gelest.

3-2-2 Preparation of Manganese Steareate ($Mn(St)_2$)

A mixture of $Mn(OAc)_2 \cdot 4H_2O$ (1.000 g, 4.08 mmol) and stearic acid (5.226 g, 18.37 mmol) were degassed under vacuum at 100 °C and then under inert atmosphere, the temperature was increased to 180 °C and held for 20 min. After cooling the reaction mixture to 100 °C, the reaction mixture degassed for another 60 min. The flask was cooled down to room temperature and white solid was obtained.

3-2-3 Hyperbranched Mn^{2+}:ZnSe (1)

In a three-neck flask $Mn(St)_2$ (~0.003 g, 5 μmol), zinc undecylenate (0.0865 g, 0.20 mmol), Ph_2Se_2 (0.1000 g, 0.32 mmol) and OLA (5.00 g, 18.7 mmol) were degassed at 100 °C for 90 min and then under nitrogen atmosphere, the temperature was increased to 280 °C and held for 10 min. After 10 min, the heating mantle was removed, and the reaction mixture was cooled down to 65 ˚C immediately using a water bath. Then, 2 ml of toluene was added to the reaction mixture followed by 5 ml of methanol. The particles were separated by centrifugation, resuspended in toluene, and precipitated with methanol again. The final sample was dispersed in cyclohexane. Mn^{2+}:ZnSe NCs were also synthesized using similar moles of $Mn(OAc)_2$•$4H_2O$ and $MnCl_2$•$4H_2O$.

3-2-4 Mn^{2+}:$ZnSe_{1-x}S_x$

Samples were prepared using a procedure similar to that for**1**, but with mixtures of Ph_2Se_2 and Me_2S_2 or Ph_2S_2. The total amount of dichalcogenide was kept near ~0.33 mmol. Ratios of Ph_2Se_2:R_2S_2 were approximately 3:1(**2**), 1:1(**3a**), 5:4 (**3b**), and 1:3(**4**). In the case of Mn^{2+}:ZnS (**5**), Me_2S_2 (31 μl, 0.35 mmol) was used instead of Ph_2Se_2 and the reaction was carried out at 300 °C. Because of the lower boiling point of Me_2S_2, it must be injected into the reaction mixture after the degassing step.

3-2-5 $[NMe_4][Zn_4(SePh)_{10}]$

The cluster precursor was prepared by adapting previous methods.[43,44]Three separate solutions were prepared and degassed for 30-60 min by bubbling with N_2: 1) $Zn(NO_3)_2$•$6H_2O$ (7.318 g) in 35 ml MeOH, 2) Me_4NCl (4.42 g) in 20 ml MeOH, and 3) TEA (9.5 g) in 20 ml MeOH. Under a N_2 overpressure, PhSeH (10 g) was added to solution 3, followed by stirring for 20 minutes. Solution 1 was then transferred to solution 3 dropwise via cannula, forming a cloudy suspension.

After cannula transfer of solution 2 to solution 3 over a period of 10-30 min, solution 3 was cooled in an ice bath for 30 min. The solid was then filtered and rinsed thoroughly with MeOH and toluene, yielding a white powder.

3-2-6 Mn^{2+}:ZnSe (6)

Unbranched Mn^{2+}:ZnSe NCs were synthesized by adapting previously described methods.[28,44] Briefly, OLA (10 g) and $MnCl_2$•$4H_2O$ (0.0012 g, 6.1μmol) were combined in a flask and degassed at 100 °C under vacuum for 120 min. After cooling below 80 °C, the cluster precursor (0.2 g, 0.073 mmol) and Se (0.0108 g, 0.137 mmol) were added under N_2 overpressure. After briefly degassing the solution under vacuum at 100 °C, the reaction is heated to 280 °C under N_2 and the NCs are grown at this temperature for 15 min. After cooling below 80 °C, the NCs were isolated by precipitation and resuspension with methanol and toluene, respectively.

3-2-7 Thiol titrations

Thiol titration experiments were performed using a PTI Quanta Master 400 fluorometer. The samples were prepared in a 10 mm septum-sealed screw-top cuvette (Starna Cells, Inc.) with a stir bar and were diluted to have absorbance ~0.3 at 350 nm. A syringe pump (New Era Pump Systems, Inc.) was used for the titration with injection of thiol via a syringe with NanoTight™ adapters (Idex Health & Science, LLC) and 250 μm diameter flexible fused silica capillary tubing (Polymicro Technologies) which was inserted through the cuvette septum. While stirring, spectra were taken at intervals of 2-30 minutes, depending on sample brightness and sensitivity. Titrations were done until there was no increase in Mn^{2+} PL.

3-2-8 Physical measurements

In this study a Cary 500 UV-Vis-NIR spectrophotometer was used for recording UV-vis absorption spectra. A PTI Quanta Master 400 fluorometer was used to record photoluminescence

and photoluminescence excitation spectra. For transmission electron microscopy (TEM) analysis, a drop of sample was dried on a copper grid. TEM images were recorded using a FEI Tecnai G2 Spirit BioTWIN microscope. The EPR spectrum was recorded using a Bruker EMXplus X-band EPR spectrometer. Powder X-ray diffraction (XRD) patterns were recorded using PANalytical Empyrean multi-purpose x-ray diffractometer.

3-3 Results and discussion

3-3-1 Synthesis of Mn^{2+}:$ZnSe_{1-x}S_x$ nanocrystals

The general synthetic procedure used to obtain the NCs is shown in Figure 1. The synthesis is similar to ot described methods using dichalcogenide precursors (previous chapter) with the notable distinction of inclusion of the dichalcogenides in the reaction mixture at temperatures lower than that of the reaction (heat-up method). Generally, a Zn^{2+} precursor (zinc undecylenate), Mn^{2+} precursor (manganese stearate), and dichalcogenide(s) are combined in a coordinating solvent (oleylamine). After heating at 280 °C in an inert atmosphere for 10-60 minutes, NCs form. The exception was for Mn^{2+}:ZnS (4), which required 300 °C to obtain a significant quantity of NCs. The NCs are isolated by precipitation and resuspension in organic solvent followed by characterization to determine NC photophysical and magnetic properties, and structures.

3-3-1 Formation of Mn^{2+}:$ZnSe_{1\_x}S_x$ nanocrystals

This procedure is related to the synthesis of Mn^{2+}-doped II-VI NCs using a tetramer ($[Zn_4(EPh)_{10}]^{2-}$) or decamer ($[Zn_{10}Se_4(EPh)_{16}]^{4-}$) cluster precursor in that a heating-up method is employed and the cluster contains organyl chalcogenide ligands.[28,29] The most widely used

cluster has E = S, likely because of the high cost of the selenol precursor (vs thiol). However, NCs synthesized with this precursor are known to contain sulfur impurities.[29] The key advantages of the dichalcogenide-doping method presented here are the simplified procedure, as preparation of cluster precursor(s) is not required, and the air-stable diselenide precursor is substantially less expensive than the phenylselenol precursor required for metal-selenide cluster synthesis. The procedure used to obtain the NCs is shown in Figure 3-1. Generally, a Zn^{2+} precursor (zinc undecylenate), Mn^{2+} precursor (manganese stearate), and dichalcogenide(s) are combined in a coordinating solvent (oleylamine). After heating at 280 °C in an inert atmosphere for 10−60 minutes, NCs form. The exception was for Mn^{2+}:ZnS (5), which required 300 °C to obtain a significant quantity of NCs. The NCs are isolated by precipitation and resuspension in organic solvent followed by characterization to determine NC photophysical and magnetic properties, and structures.

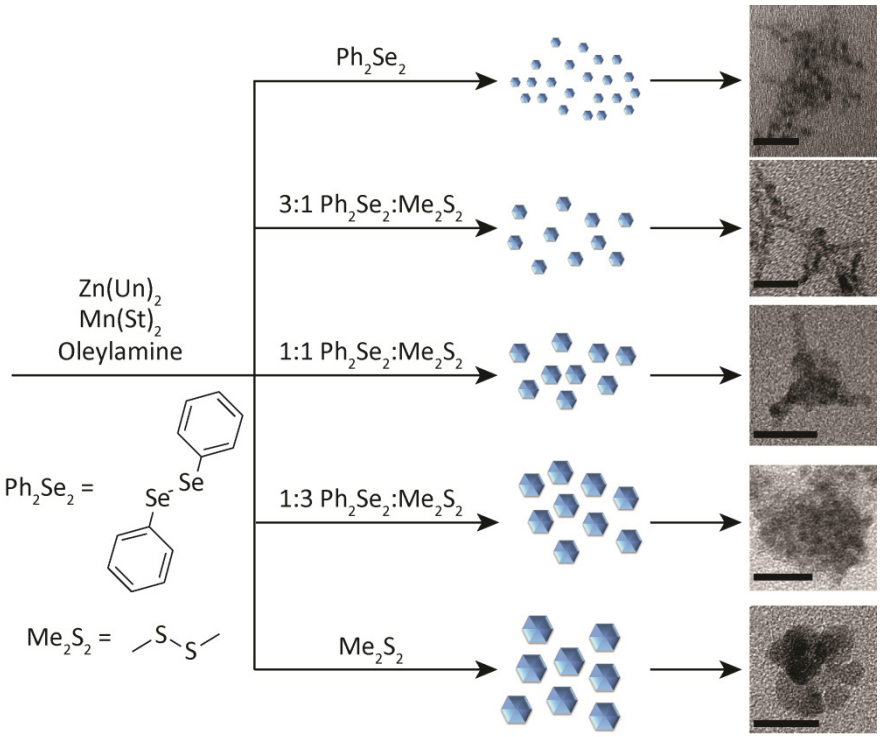

Figure 3-1 General synthetic scheme for formation of Mn^{2+}-doped $ZnSe_{1-x}S_x$ NCs. In the reaction, zinc undecylenate, $Zn(Un)_2$, manganese stearate, $Mn(St)_2$, and a mixture of diphenyl diselenide and dimethyl disulphide (or diphenyl disulphide) are combined and heated to reaction temperature in an alkylamine under an inert atmosphere. Depending on the ratio of diselenide to disulphide, NCs of different shapes and sizes are obtained. Images of samples **1**-**5** are shown. Scale bars are 20 nm.

Initially, NCs were synthesized using only the Ph_2Se_2 dichalcogenide precursor (1). These NCs exhibited absorption and PL spectra characteristic of Mn^{2+}:ZnSe NCs (Figure 3-2, black line). The absorption feature near 390 nm indicates formation of the ZnSe host NCs. The PL spectrum has a peak centred at 586 nm, indicative of Mn^{2+} luminescence. The rapid transfer of energy from the NC to the Mn^{2+} efficiently competes with excitonic recombination, and no blue ZnSe emission is observed. Subsequent reactions combined the Ph_2Se_2 precursor with a disulphide precursor, to form Mn^{2+}:$ZnSe_{1\_x}S_x$ NCs of different shapes. Two disulphide precursors were used: Ph_2S_2 and Me_2S_2. Starting ratios of diselenide to disulphide were varied from 1 : 0 (1), 3 : 1 (2), 1 : 1 (3), 1 : 3 (4), and 0:1 (5). The first absorption feature of the NCs blue-shifted from that of 1, indicating likely sulfur incorporation, with a systematic decrease in wavelength with increasing Me_2S_2.

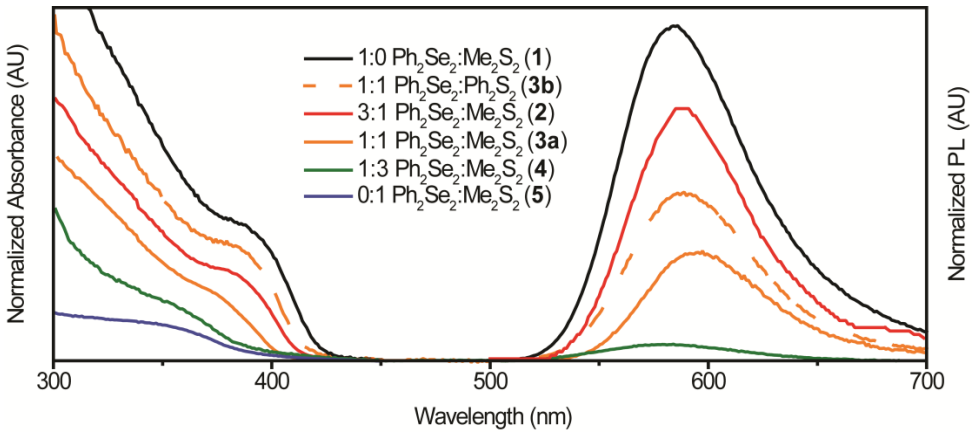

Figure 3-2. Absorption (left) and PL (right) spectra of Mn^{2+}:$ZnSe_{1-x}S_x$ NCs with varying dichalcogenide precursor ratios. The NC first absorption peak shifts from ~390 nm for Ph_2Se_2 alone (1) to a broad feature at ~340 nm for Me_2S_2 alone (5). The PL peak red-shifts from 586 to 589 nm with increasing S. For 4, very little luminescence was detected and for 5 no luminescence was detected.

Comparing absorption and emission spectra for the Me_2S_2 and Ph_2S_2 samples with similar ratios (3a and 3b), yields insight into the effect of disulfide precursor on the resulting product. Although similar ratios were used, the absorption of 3a is noticeably blue-shifted from that of 3b, indicating decreased reactivity of Ph_2S_2 vs. Me_2S_2, as reported previously.[20] These NCs (3b) exhibit a PL peak at 588 nm, slightly red-shifted from the PL peak of 1 at 586 nm. For the other NC samples, the PL peaks red shifted to 589 nm with increasing disulphide (2, 3a). The PL intensity decreased with larger Me_2S_2 amounts, such that only a broad, very weak peak was observed for 4 and none was detectable in the Me_2S_2 only sample (5). To confirm the orange PL associated with Mn^{2+} was coming from the NCs, photoluminescence excitation (PLE) spectra were taken. The resulting spectra (Figure. 3-3) exhibit the characteristic first absorption feature of the NCs with a continued increase at higher energies.

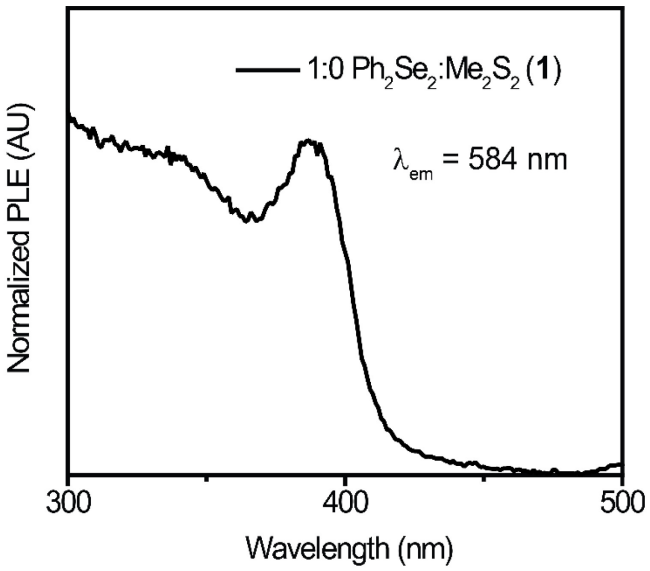

Figure 3-3 Photoluminescence excitation spectrum of Mn^{2+}:ZnSe synthesized with Ph_2Se_2. The emission was detected at 584 nm while scanning excitation wavelengths from 300-500 nm. The PLE spectrum exhibits the characteristic NC first excitonic feature near 390 nm along with a continuous increase in intensity at higher energies

3-3-2 Morphology and structure of Mn^{2+}:$ZnSe_{1\_x}S_x$ nanocrystals

The key to changing the NC shape and degree of branching is the ratio of diselenide to disulphide precursor.

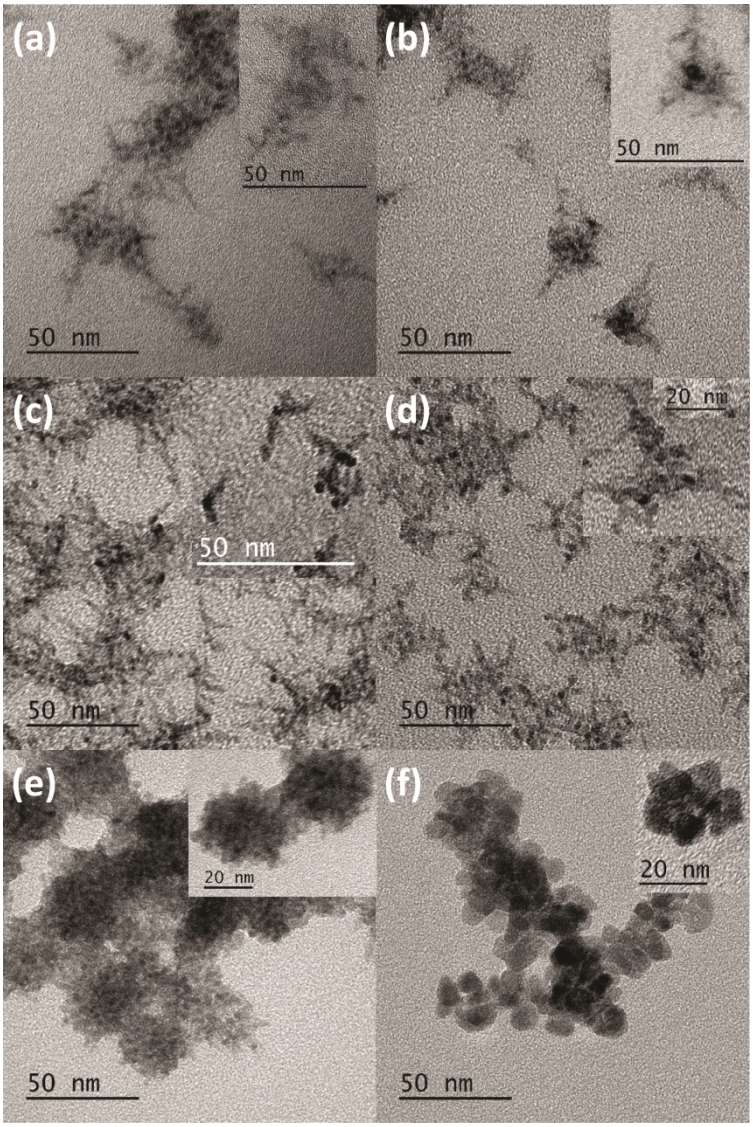

Figure 3-4 TEM images of (a) 1, (b) 3b, (c) 2, (d) 3a, (e) 4, and (f) 5. Large image scale bars are 50 nm. Inset image scale bars are 50 nm for a-c and 20 nm for d-f. Highly branched structures at low S:Se ratios transition to more spherical samples at higher S:Se ratios. Insets highlight particles that are linking together, likely through oriented attachment, to form larger networks and aggregates of the NCs. The shape, size, and structure of these particles is reflected in the larger structure of the resulting nanomaterial.

Figure 3-4 shows TEM images of NCs prepared with varying ratios of diselenide and disulphide. As the amount of disulphide increases, the particles go from branched networks to rounded, linked platelets. Comparing 3a and 3b (Figure 3-4d and b) further illustrates the effect of disulphide on the reaction. The TEM image of 3b more closely resembles that of 1 (Figure 3-4a), exhibiting significant branching. This branching appears to stem not only from the centre of a particle, but also from the outward reaching NC arms (Figure. 3-5 to 3-8).

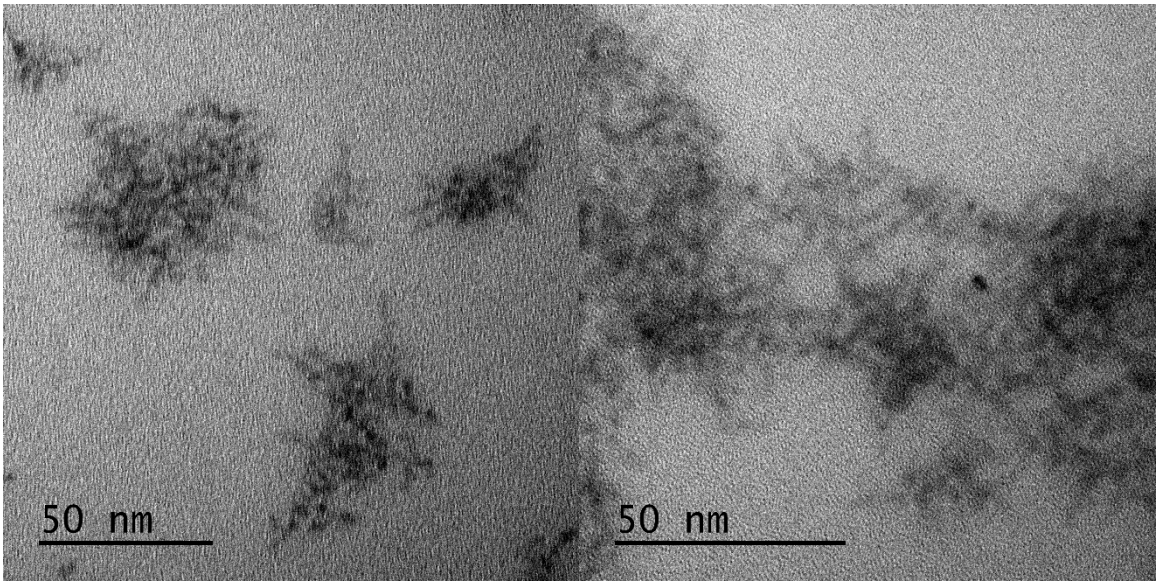

Figure 3-5 TEM images of 1. Additional images of the NCs demonstrating branching patterns.

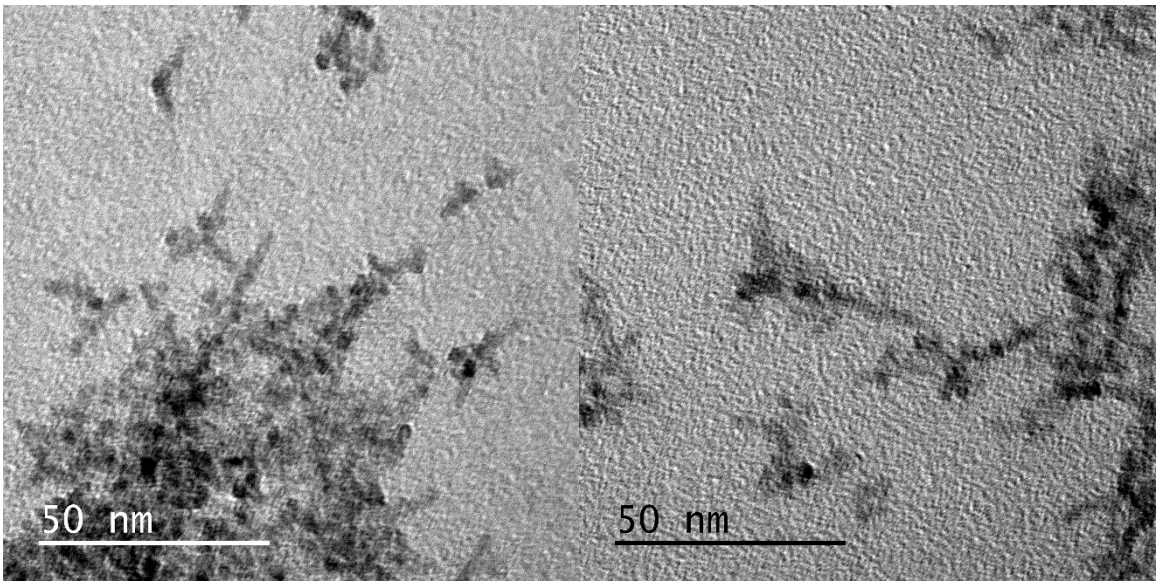

Figure 3-6 TEM images of 2. Additional images of the NCs demonstrating branching patterns.

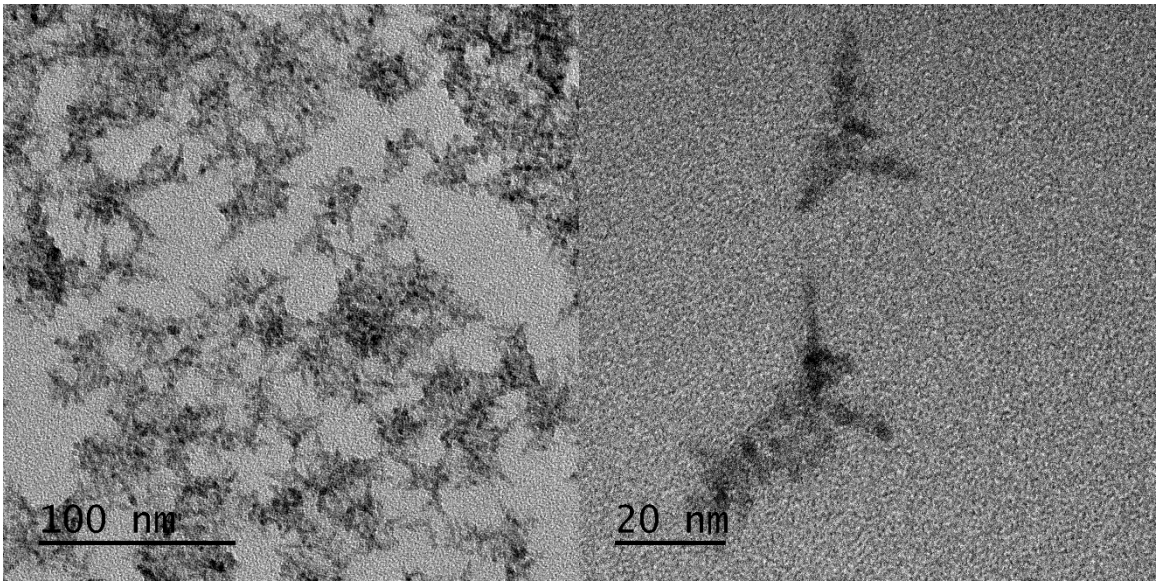

Figure 3-7 TEM images of 3a. Additional images of the NCs demonstrating branching patterns.

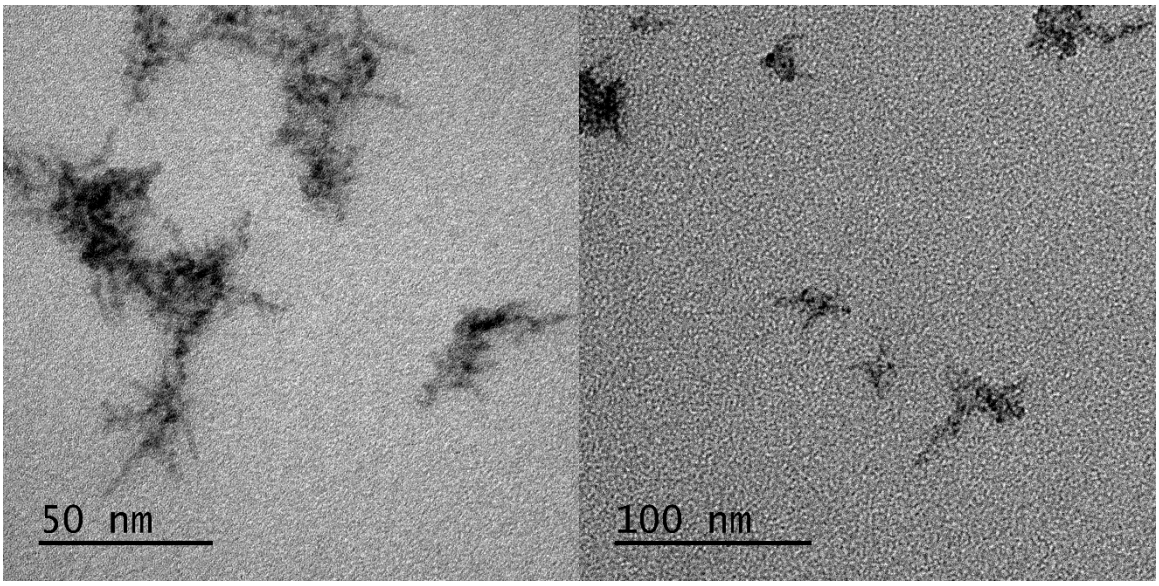

Figure 3-8 TEM images of 3b. Additional images of the NCs demonstrating branching patterns.

The appearance of isolated particles (shown in Figure 3-4 insets) within the samples suggests oriented attachment may be occurring as well, creating highly branched networks.[41,45,46] This will be discussed further in the discussion of the formation mechanism. TEM images of 2 and 3a (Figure 3-4c and d) also exhibit networks of hyperbranched particles.

Although these networks are complex, the insets provide key details about the smaller, branched particles forming the larger networks. For both 2 and 3a, smaller particles with more rounded, thicker arms are observed. These characteristics are passed on to the networks that form. Further increases in the S : Se ratio show formation of larger, rounder particles, followed by oriented attachment to form large, spherical clusters of NCs (Figure 3-4e and Figure 3-9). When only Me_2S_2 is used as the dichalcogenide precursor, large, round platelets form and link together, generating round clusters of these NCs (Figure 3-4f and Figure 3-10). Syntheses of Mn^{2+}:ZnSe with other Mn^{2+} precursors produced similar hyperbranched NCs (Figure 3-11).

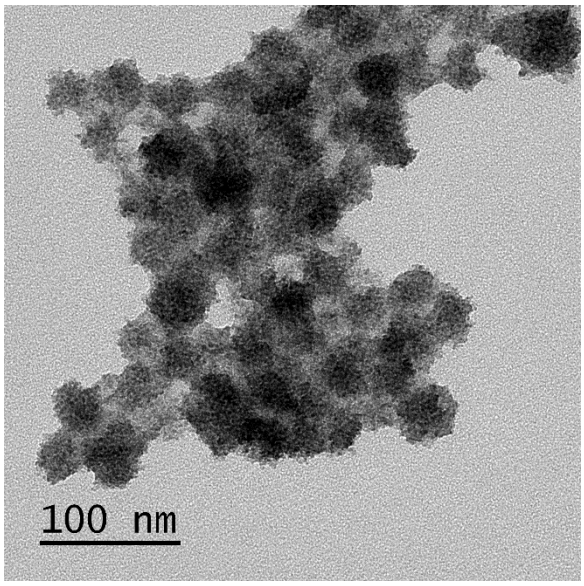

Figure 3-9 TEM image of 4. Additional images of the NCs demonstrating aggregation.

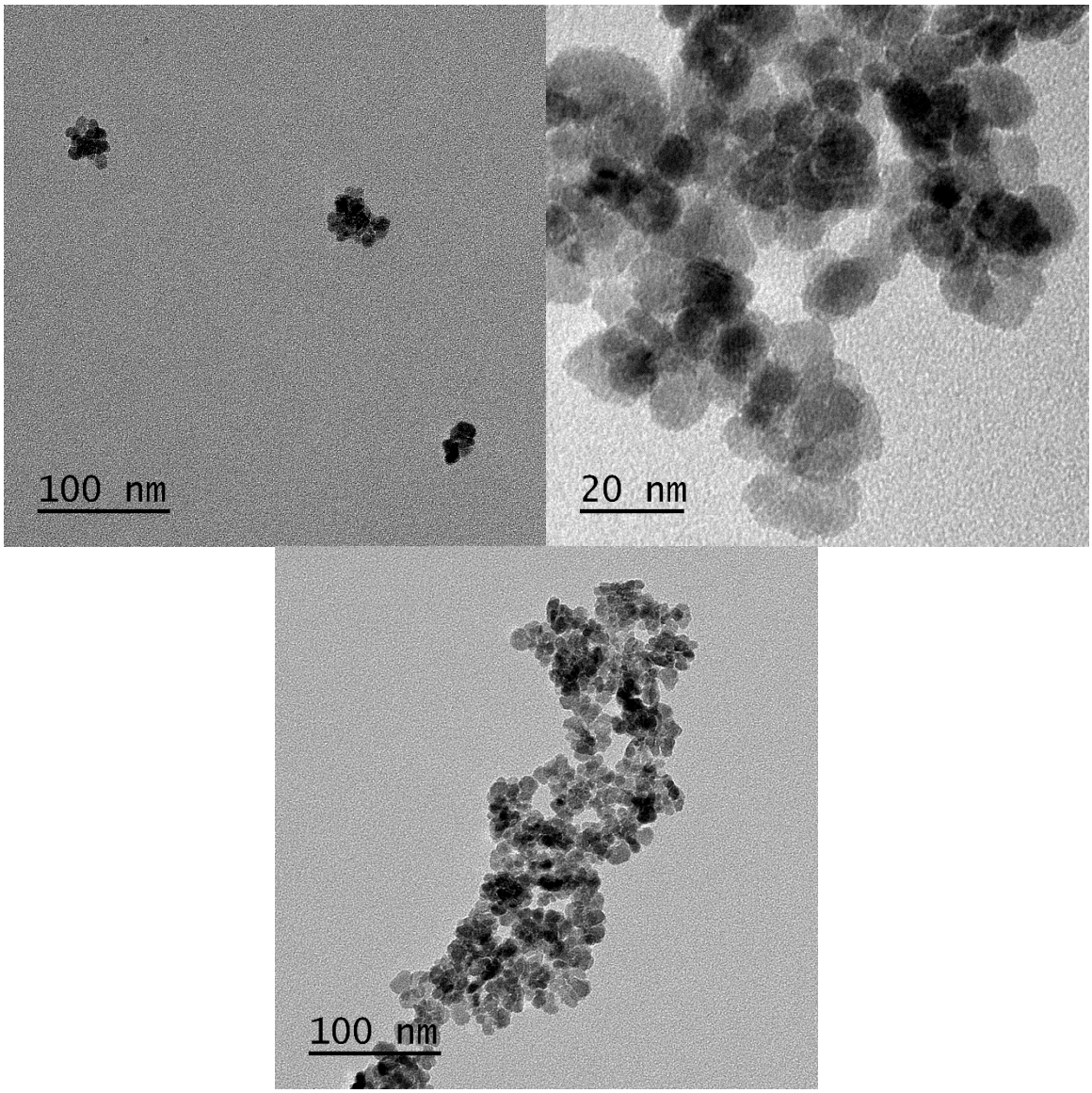

Figure 3-10 TEM images of 5. Additional images of the NCs demonstrating aggregation and formation of larger and smaller assemblies.

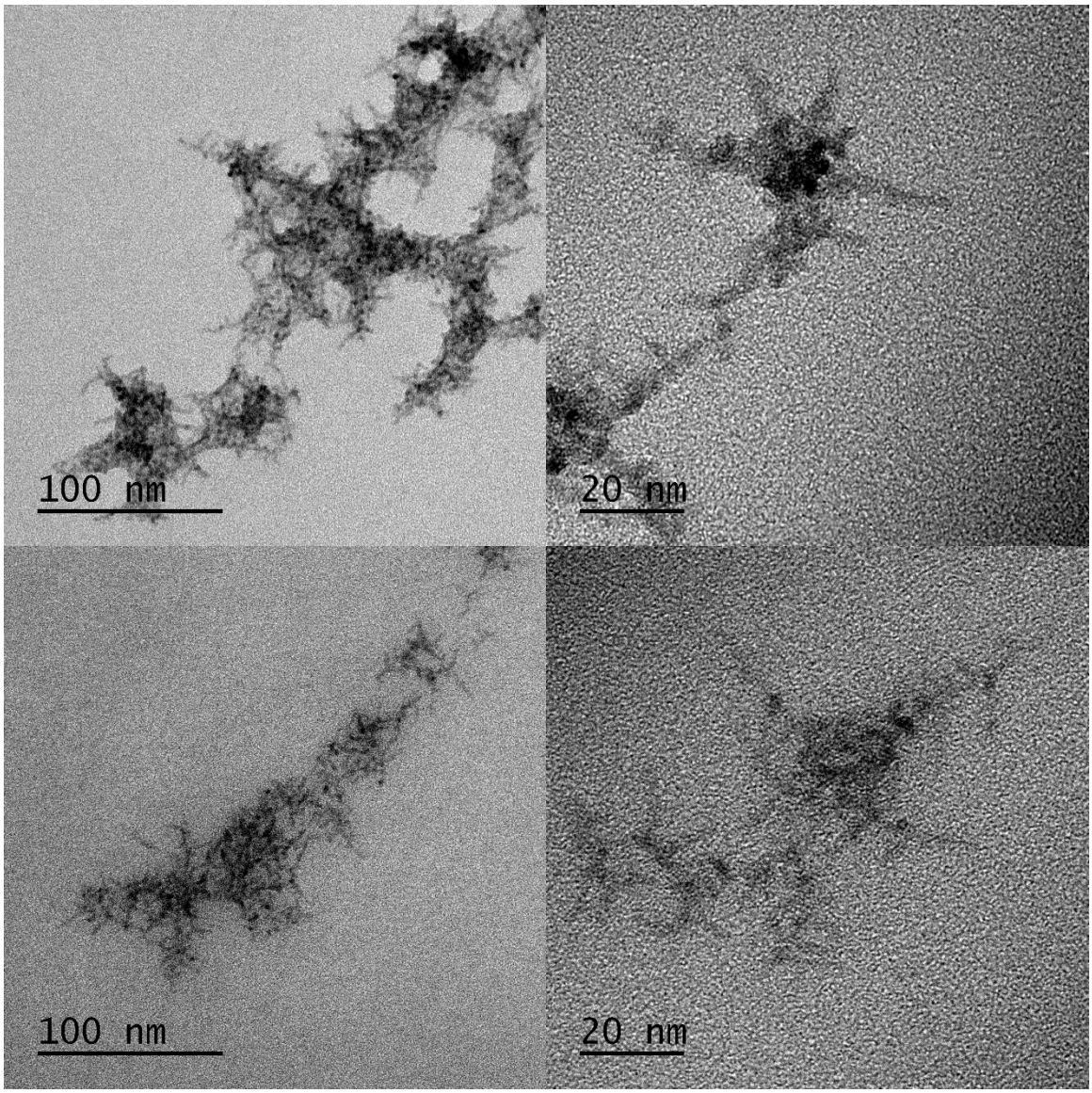

Figure 3-11 TEM images of 1 prepared using $MnCl_2 \cdot 4H_2O$ (top)and $Mn(OAc)_2 \cdot 4H_2O$ (bottom).

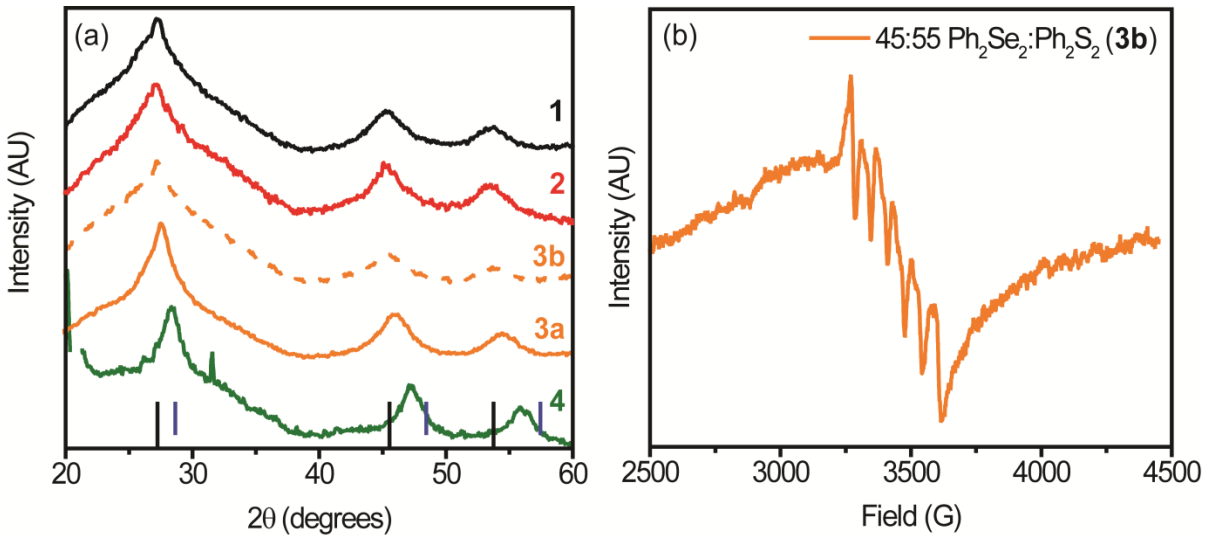

Figure 3-12 (a) XRD patterns of samples 1, 2, 3a, 3b, and 4. The patterns indicate zinc-blend structure and the broadness of the peaks indicates small NC diameters or domains. As the amount of S increases, the peaks shift to larger angles. The black lines at the bottom of the figure represent the positions of bulk ZnSe and the blue, dotted lines represent those of bulk ZnS. (b) EPR spectrum of 3b showing a splitting pattern with 6 peaks and a hyperfine coupling constant of 66.2 G**.**

Additional structural information about the NCs was obtained from XRD. The diffraction patterns in Figure 3-12a exhibit a zinc-blende pattern, with highly broadened peaks due to the small domain size of the NCs. With increasing disulphide precursor, the peaks shift to larger angles, characteristic of a transition from ZnSe to ZnS. Peak positions indicate larger sulphur content for sample 3a than 3b, providing additional evidence for the low reactivity of Ph_2S_2 vs. Me_2S_2. Ultimately the peak shifts for 3a are small relative to what is expected for a 1 : 1 ratio of S : Se in the NCs, indicating a decreased reactivity for Me_2S_2 (vs. Ph_2Se_2). No Mn diffraction peaks are observed, indicating successful doping of Mn^{2+} ions into the NCs.[47] Additional evidence of successful Mn^{2+} doping into these NCs is provided by EPR. The EPR spectrum of 3b

is shown in Figure 3-12b. The 6-peak hyperfine structure characteristic of Mn^{2+} is observed. In addition, a coupling constant of 66.2 G is estimated, consistent with values found for ZnSe (66.1 G)[16] and ZnS (68.4 G).[48]

The estimated value is substantially smaller than that of surface Mn^{2+} (~90 G),[13,14,49] further affirming Mn^{2+} incorporation.

3-3-3 Possible formation mechanisms

The dichalcogenides are known to produce nanomaterials with a variety of morphologies.[20–22] Vela and co-workers presented an elegant study in which differences in dichalcogenide bond dissociation energies were correlated with changes in particle size and shape, and found diselenide precursors reacted more quickly than analogous disulphides.[20] Although the systems studied differ from those presented here (they used Cd^{2+}, different ligands, lower temperatures, and hot-injection), the results can help explain the observed trend in particle size and shape. The formation of the NCs shown in Figure 3-4 can be explained in terms of the precursor reactivity of the disulphide vs. Ph_2Se_2.

Thus, for the faster reacting Ph_2Se_2-containing reactions, the initially formed particles are relatively small in diameter, and begin branching and attaching to form the more complex networks seen in Figure 3-4a−d. This behaviour has been attributed to the introduction of more branching angles due to twinning defects that occur in samples with more rapid growth.[23] When larger amounts of the less reactive Me_2S_2 are present, larger particles formdue to slow growth, which leads to less branching. Over time, these particles begin to link together, likely via oriented attachment.[24,41] At final reaction times, the reaction product is a network of these linked particles. A cartoon of this possible mechanismis shown in Figure 3-1, in which with less Me_2S_2, smaller particles form and aggregate, forming more highlybranched, polycrystalline networks.

With more Me_2S_2, larger NCs form before coming together to form rounded aggregates of platelets. Thus, there does not appear to be an additional ripening process occurring during the attachment process, and the final sample is characteristic of the initial NC size, as observed for similar systems.[20]

3-3-4 Application of NCs for thiol sensing

As mentioned in the introduction, an advantage of branched NCs is their large surface area, which makes them useful for applications in sensing, among others.[25–27] Thiols are known to influence processes in biology and play key roles in nanodevices. [50–54] To explore the potential application of these highly branched Mn^{2+}-doped NCs, the luminescence enhancement in the presence of thiol was studied. DDT was used as a model thiol and Figure 3-13a depicts the PL enhancement observed when small amounts of DDT are added to a solution of 3b. The Mn^{2+} PL increases, until eventually saturating at a concentration of about 70 mM, as shown in Figure 3-13b. Similar, less-sensitive behaviour is observed for the less branched NCs (2) and NCs with no branching (6). This change in sensitivity could be due to the large number of NC defects, which decrease in the order: hyperbranched ≥ branched ≥ unbranched.

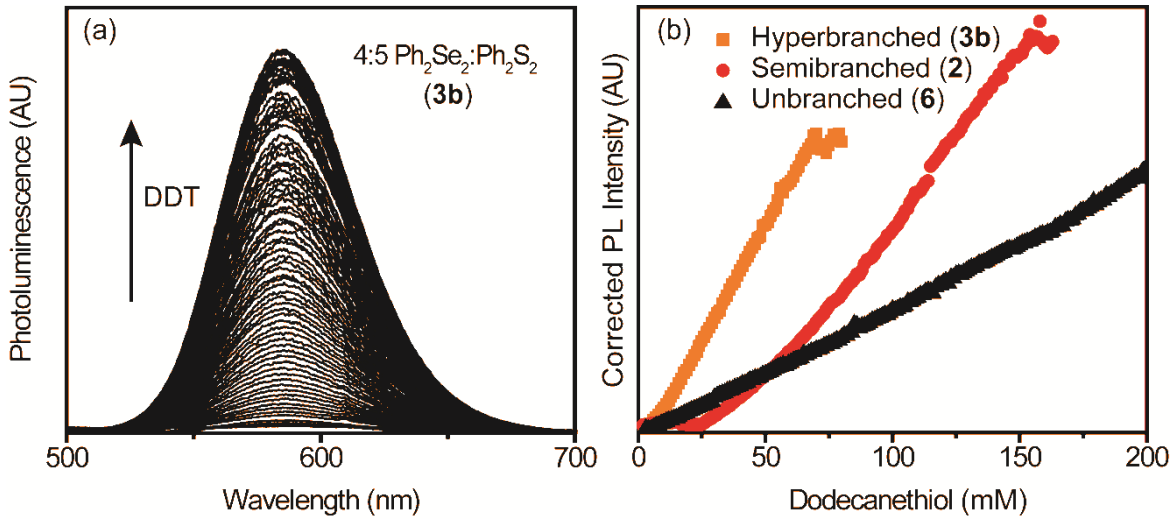

Figure 3-13(a) Steady-state PL of 3b in the presence of dodecanethiol (DDT). Increasing amount of thiol leads to a concomitant increase in Mn^{2+} PL from the NCs. Inset: TEM image of the NCs. (b) Scatter plot of the Mn^{2+} PL intensity vs [DDT] for NC samples with different degrees of branching. The more branched 3b NCs show the steepest increase in PL intensity with thiol. NCs with less (2) and no branching show decreasing sensitivity to thiol, with smaller increases in slope.

Addition of DDT may passivate these defects, providing more efficient energy transfer to the Mn^{2+}-dopants, and a brighter Mn^{2+} luminescence.[55–57] To demonstrate the utility of these NCs for biological sensing, the NCs were transferred to aqueous solution. After transfer, the Mn^{2+} luminescence of the NCs decreased, but not significantly. The NCs illuminated by a UV lamp before and after watersolubilization are shown in Figure 3-14a. Once in aqueous solution, the NCs were titrated with dithiothreitol (DTT), with a corresponding increase in PL (Figure 3-14b). DTT is key in the study of biological functions such as protein unfolding, signal transduction, and as a redox mediator.[58–61] Here, it acts as a reductant, enhancing the NC PL at concentrations from 0 to ~40 mM before decreasing again at concentrations >60 mM (Figure 3-14c). The sensitivity of the NCs to DTT is linear within this range, with an analytical sensitivity of 2.9 mM and a detection limit of 1.0 mM.

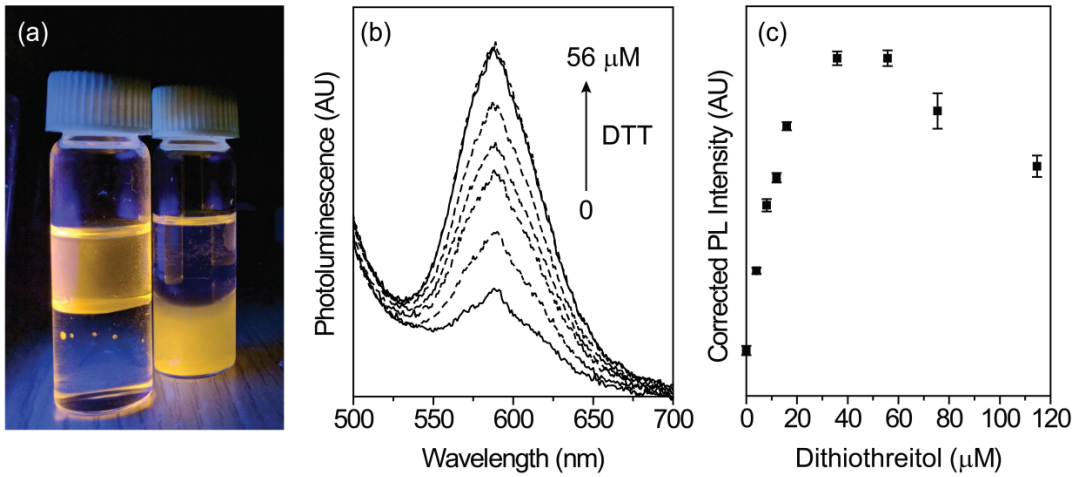

Figure 3-14 (a) Photograph of Mn^{2+}-doped hyperbranched NCs illuminated by a UV lamp in aqueous solution and in chloroform. (b) Steady-state PL of hyperbranched Mn^{2+}-ZnSe NCs in PBS with addition of a dithiothreitol (DTT) solution. As the concentration of DTT increases from 0 to 56 μM, the Mn^{2+} PL increases. (c) Scatter plot of the Mn^{2+} PL intensity vs [DTT] exhibiting a linear increase in luminescence in the μM range before decreasing in intensity at concentrations >60 μM.

This simple sensor exhibits a large, linear increase in luminescence with thiol, highlighting the advantages of these NCs as sensors. In organic solvent, differences in sensitivity (DPL vs. DDT) vary with branching, although additional study is required to explore the complex interplay of structure, branching, defect formation, and dopant incorporation, which all likely play a role in the luminescence response. In aqueous medium, enhancement of PL by DTT is linear at low concentrations, with high sensitivities. The mechanism of PL increase is likely related to passivation of surface traps, providing a pathway for enhanced sensitivity to biological thiols through the increase in surface defects present in these hyperbranched Mn^{2+}-doped materials.

3-4 Summary

A new synthetic method for obtaining doped $ZnSe_{1\_x}S_x$ NCs yields luminescent NCs of a variety of structures. Variations in dichalcogenide precursor can be used to tune the NC size and shape. Knowing the reactants reactivity, syntheses can be designed to obtain NCs of desired size, shape, and dopant incorporation. This method provides access to luminescent materials that are not usually emissive due to high defect levels. The resulting emissive, hyperbranched materials decrease losses in PL due to defects by employing Mn^{2+} as a luminescent trap. These NCs can be used as turn-on thiol sensors, with sensitivity varying with branching in organic solution. A similar response is observed in aqueous solution, with a large increase in PL at low thiol levels. This synthetic procedure is extendable to other NC systems synthesized using dichalcogenides and other dopants, providing a new pathway to luminescent, hyperbranched materials.

3-5 Conclusion

Our study showed that luminescent hyperbranched NCs could be synthesized through doping. The synthesized NCs can be used for thiol sensing, and the more branched NCs have higher sensitivity to the thiols. One limitation of the synthesized NCs is that the shell growth on giant NCs and embedding them in silica shell will give micro size particles with low solubility so non-branched, spherical NCs have higher application potential in aqueous media.

3-6 References

(1) Jüstel, T. Phosphors for Plasma Display Panels. In *Luminescence*; Ronda, C., Ed.; Wiley-VCH Verlag GmbH & Co. KGaA, 2007; pp 61–73.

(2) Blasse, P. D. G.; Grabmaier, P. D. B. C. Lamp Phosphors. In *Luminescent Materials*; Springer Berlin Heidelberg, 1994; pp 108–133.

(3) Thakar, R.; Chen, Y.; Snee, P. T. Efficient Emission from Core/(Doped) Shell Nanoparticles: Applications for Chemical Sensing. *Nano Lett.* **2007**, *7* (11), 3429–3432.

(4) Santra, S.; Dutta, D. Quantum Dots for Cancer Imaging. In *Nanoparticles in Biomedical Imaging*; Bulte, J. W. M., Modo, M. M. J., Eds.; Fundamental Biomedical Technologies; Springer New York, 2008; pp 463–485.

(5) Wu, P.; Yan, X.-P. Doped Quantum Dots for Chemo/Biosensing and Bioimaging. *Chem. Soc. Rev.* **2013**, *42* (12), 5489–5521.

(6) Santra, P. K.; Kamat, P. V. Mn-Doped Quantum Dot Sensitized Solar Cells: A Strategy to Boost Efficiency over 5%. *J. Am. Chem. Soc.* **2012**, *134* (5), 2508–2511.

(7) Debnath, T.; Maity, P.; Maiti, S.; Ghosh, H. N. Electron Trap to Electron Storage Center in Specially Aligned Mn-Doped CdSe d-Dot: A Step Forward in the Design of Higher Efficient Quantum-Dot Solar Cell. *J. Phys. Chem. Lett.* **2014**, *5* (16), 2836–2842.

(8) Tian, J.; Lv, L.; Fei, C.; Wang, Y.; Liu, X.; Cao, G. A Highly Efficient (>6%) Cd1−xMnxSe Quantum Dot Sensitized Solar Cell. *J. Mater. Chem. A* **2014**, *2* (46), 19653–19659.

(9) Hu, Z.; Xu, S.; Xu, X.; Wang, Z.; Wang, Z.; Wang, C.; Cui, Y. Co-Doping of Ag into Mn:ZnSe Quantum Dots: Giving Optical Filtering Effect with Improved Monochromaticity. *Sci. Rep.* **2015**, *5*, 14817.

(10) Kim, H.-J.; Lee, H.-D.; Kumar, C. S. S. P.; Rao, S. S.; Chung, S.-H.; Punnoose, D. The Effect of Manganese in a CdS/PbS Colloidal Quantum Dot Sensitized TiO2 Solar Cell to Enhance Its Efficiency. *New J. Chem.* **2015**.

(11) Ithurria, S.; Guyot-Sionnest, P.; Mahler, B.; Dubertret, B. ${\mathrm{Mn}}^{2+}$ as a Radial Pressure Gauge in Colloidal Core/Shell Nanocrystals. *Phys. Rev. Lett.* **2007**, *99* (26), 265501.

(12) Yang, Y.; Chen, O.; Angerhofer, A.; Cao, Y. C. On Doping CdS/ZnS Core/Shell Nanocrystals with Mn. *J. Am. Chem. Soc.* **2008**, *130* (46), 15649–15661.

(13) Acharya, S.; Sarma, D. D.; Jana, N. R.; Pradhan, N. An Alternate Route to High-Quality ZnSe and Mn-Doped ZnSe Nanocrystals. *J. Phys. Chem. Lett.* **2010**, *1* (2), 485–488.

(14) Zheng, W.; Wang, Z.; Wright, J.; Goundie, B.; Dalal, N. S.; Meulenberg, R. W.; Strouse, G. F. Probing the Local Site Environments in Mn:CdSe Quantum Dots. *J. Phys. Chem. C* **2011**, *115* (47), 23305–23314.

(15) Beaulac, R.; Ochsenbein, S. T.; Gamelin, D. R. Colloidal Transition-Metal-Doped Quantum Dots. In *Nanocrystal Quantum Dots, Second Edition*; CRC Press, 2010; pp 397–453.

(16) Norris, D. J.; Yao, N.; Charnock, F. T.; Kennedy, T. A. High-Quality Manganese-Doped ZnSe Nanocrystals. *Nano Lett.* **2001**, *1* (1), 3–7.

(17) Bhargava, R. N.; Gallagher, D.; Hong, X.; Nurmikko, A. Optical Properties of Manganese-Doped Nanocrystals of ZnS. *Phys. Rev. Lett.* **1994**, *72* (3), 416–419.

(18) Yu, J. H.; Kwon, S.-H.; Petrášek, Z.; Park, O. K.; Jun, S. W.; Shin, K.; Choi, M.; Park, Y. I.; Park, K.; Na, H. B.; et al. High-Resolution Three-Photon Biomedical Imaging Using Doped ZnS Nanocrystals. *Nat. Mater.* **2013**, *12* (4), 359–366.

(19) Norako, M. E.; Franzman, M. A.; Brutchey, R. L. Growth Kinetics of Monodisperse Cu−In−S Nanocrystals Using a Dialkyl Disulfide Sulfur Source. *Chem. Mater.* **2009**, *21* (18), 4299–4304.

(20) Guo, Y.; Alvarado, S. R.; Barclay, J. D.; Vela, J. Shape-Programmed Nanofabrication: Understanding the Reactivity of Dichalcogenide Precursors. *ACS Nano* **2013**, *7* (4), 3616–3626.

(21) Wang, J.; Singh, A.; Liu, P.; Singh, S.; Coughlan, C.; Guo, Y.; Ryan, K. M. Colloidal Synthesis of Cu2SnSe3 Tetrapod Nanocrystals. *J. Am. Chem. Soc.* **2013**, *135* (21), 7835–7838.

(22) Brutchey, R. L. Diorganyl Dichalcogenides as Useful Synthons for Colloidal Semiconductor Nanocrystals. *Acc. Chem. Res.* **2015**, *48* (11), 2918–2926.

(23) Kanaras, A. G.; Sönnichsen, C.; Liu, H.; Alivisatos, A. P. Controlled Synthesis of Hyperbranched Inorganic Nanocrystals with Rich Three-Dimensional Structures. *Nano Lett.* **2005**, *5* (11), 2164–2167.

(24) Li, H.; Kanaras, A. G.; Manna, L. Colloidal Branched Semiconductor Nanocrystals: State of the Art and Perspectives. *Acc. Chem. Res.* **2013**, *46* (7), 1387–1396.

(25) Zhou, Z.-Y.; Tian, N.; Li, J.-T.; Broadwell, I.; Sun, S.-G. Nanomaterials of High Surface Energy with Exceptional Properties in Catalysis and Energy Storage. *Chem. Soc. Rev.* **2011**, *40* (7), 4167–4185.

(26) Nguyen, T.-D.; Dinh, C.-T.; Do, T.-O. Tailoring the Assembly, Interfaces, and Porosity of Nanostructures toward Enhanced Catalytic Activity. *Chem. Commun.* **2014**, *51* (4), 624–635.

(27) Nose, K.; Soma, Y.; Omata, T.; Otsuka-Yao-Matsuo, S. Synthesis of Ternary CuInS2 Nanocrystals; Phase Determination by Complex Ligand Species. *Chem. Mater.* **2009**, *21* (13), 2607–2613.

(28) Cumberland, S. L.; Hanif, K. M.; Javier, A.; Khitrov, G. A.; Strouse, G. F.; Woessner, S. M.; Yun, C. S. Inorganic Clusters as Single-Source Precursors for Preparation of CdSe, ZnSe, and CdSe/ZnS Nanomaterials. *Chem. Mater.* **2002**, *14* (4), 1576–1584.

(29) Archer, P. I.; Santangelo, S. A.; Gamelin, D. R. Inorganic Cluster Syntheses of TM2+-Doped Quantum Dots (CdSe, CdS, CdSe/CdS): Physical Property Dependence on Dopant Locale. *J. Am. Chem. Soc.* **2007**, *129* (31), 9808–9818.

(30) Vlaskin, V. A.; Barrows, C. J.; Erickson, C. S.; Gamelin, D. R. Nanocrystal Diffusion Doping. *J. Am. Chem. Soc.* **2013**, *135* (38), 14380–14389.

(31) Yu, J. H.; Liu, X.; Kweon, K. E.; Joo, J.; Park, J.; Ko, K.-T.; Lee, D. W.; Shen, S.; Tivakornsasithorn, K.; Son, J. S.; et al. Giant Zeeman Splitting in Nucleation-Controlled Doped CdSe:Mn2+ Quantum Nanoribbons. *Nat. Mater.* **2010**, *9* (1), 47–53.

(32) Yao, T.; Kou, S.; Sun, Y.; Zhao, Q.; Yang, J. Facile Synthesis, Optical Properties and Growth Mechanism of Elongated Mn-Doped ZnSe1−xSx Nanocrystals. *CrystEngComm* **2012**, *14* (24), 8440.

(33) Lu, S. W.; Lee, B. I.; Wang, Z. L.; Tong, W.; Wagner, B. K.; Park, W.; Summers, C. J. Synthesis and Photoluminescence Enhancement of Mn2+-Doped ZnS Nanocrystals. *J. Lumin.* **2000**, *92* (1–2), 73–78.

(34) Bryan, J. D.; Gamelin, D. R. Doped Semiconductor Nanocrystals: Synthesis, Characterization, Physical Properties, and Applications. In *Progress in Inorganic Chemistry*; Karlin, K. D., Ed.; John Wiley & Sons, Inc., 2005; pp 47–126.

(35) Lee, J. Y.; Kim, D. S.; Kang, J. H.; Yoon, S. W.; Lee, H.; Park, J. Novel Zn1-XMnxSe (x = 0.1−0.4) One-Dimensional Nanostructures: Nanowires, Zigzagged Nanobelts, and Toothed Nanosaws. *J. Phys. Chem. B* **2006**, *110* (51), 25869–25874.

(36) Chin, P. T. K.; Stouwdam, J. W.; Janssen, R. A. J. Highly Luminescent Ultranarrow Mn Doped ZnSe Nanowires. *Nano Lett.* **2009**, *9* (2), 745–750.

(37) Zhang, M.; Lu, Y.; Chen, J.-F.; Zhang, T.-K.; Liu, Y.-Y.; Yang, Y.; Yao, W.-T.; Yu, S.-H. Selective Synthesis of Zn1 − XMnxSe Nanobelts and Nanotubes from [Zn1 − XMnxSe](DETA)0.5 Nanbelts in Solution (x = 0−0.15) and Their EPR and Optical Properties. *Langmuir* **2010**, *26* (15), 12882–12889.

(38) Acharya, S.; Sarkar, S.; Pradhan, N. Material Diffusion and Doping of Mn in Wurtzite ZnSe Nanorods. *J. Phys. Chem. C* **2013**, *117* (11), 6006–6012.

(39) Jin, C. Q.; Ge, C. H.; Xu, G.; Wei, Y. X.; Ding, Q. P.; Zhu, M.; Duan, H. B. Controllable Synthesis and Cathodoluminescent Property of 1D Wurtzite ZnS Nanostructures. *J. Alloys Compd.* **2015**, *648*, 481–487.

(40) Wu, Y. A.; Warner, J. H. Shape and Property Control of Mn Doped ZnSe Quantum Dots: From Branched to Spherical. *J. Mater. Chem.* **2012**, *22* (2), 417–424.

(41) Lv, W.; He, W.; Wang, X.; Niu, Y.; Cao, H.; Dickerson, J. H.; Wang, Z. Understanding the Oriented-Attachment Growth of Nanocrystals from an Energy Point of View: A Review. *Nanoscale* **2014**, *6* (5), 2531–2547.

(42) Xue, X.; Penn, R. L.; Leite, E. R.; Huang, F.; Lin, Z. Crystal Growth by Oriented Attachment: Kinetic Models and Control Factors. *CrystEngComm* **2014**, *16* (8), 1419–1429.

(43) Dance, I. G.; Choy, A.; Scudder, M. L. Syntheses, Properties, and Molecular and Crystal Structures of (Me4N)4[E4M10(SPh)16] (E = Sulfur or Selenium; M = Zinc or Cadmium): Molecular Supertetrahedral Fragments of the Cubic Metal Chalcogenide Lattice. *J. Am. Chem. Soc.* **1984**, *106* (21), 6285–6295.

(44) Vlaskin, V. A.; Beaulac, R.; Gamelin, D. R. Dopant−Carrier Magnetic Exchange Coupling in Colloidal Inverted Core/Shell Semiconductor Nanocrystals. *Nano Lett.* **2009**, *9* (12), 4376–4382.

(45) Penn, R. L.; Banfield, J. F. Imperfect Oriented Attachment: Dislocation Generation in Defect-Free Nanocrystals. *Science* **1998**, *281* (5379), 969–971.

(46) Zhang, H.; Penn, R. L.; Lin, Z.; Cölfen, H. Nanocrystal Growth via Oriented Attachment. *CrystEngComm* **2014**, *16* (8), 1407–1408.

(47) Yang, B.; Shen, X.; Zhang, H.; Cui, Y.; Zhang, J. Luminescent and Magnetic Properties in Semiconductor Nanocrystals with Radial-Position-Controlled Mn2+ Doping. *J. Phys. Chem. C* **2013**, *117* (30), 15829–15834.

(48) Park, B. j.; Im, W. b.; Chung, W. j.; Seo, H. s.; Ahn, J. t.; Jeon, D. y. Internal Pressure Effect on Cathodoluminescence Enhancement of ZnS:Mn2+ Synthesized by a Sealed Vessel. *J. Mater. Res.* **2007**, *22* (10), 2838–2844.

(49) Zu, L.; Wills, A. W.; Kennedy, T. A.; Glaser, E. R.; Norris, D. J. Effect of Different Manganese Precursors on the Doping Efficiency in ZnSe Nanocrystals. *J. Phys. Chem. C* **2010**, *114* (50), 21969–21975.

(50) Donhauser, Z. J.; Mantooth, B. A.; Kelly, K. F.; Bumm, L. A.; Monnell, J. D.; Stapleton, J. J.; Price, D. W.; Rawlett, A. M.; Allara, D. L.; Tour, J. M.; et al. Conductance Switching in Single Molecules Through Conformational Changes. *Science* **2001**, *292* (5525), 2303–2307.

(51) Townsend, D. M.; Tew, K. D.; Tapiero, H. The Importance of Glutathione in Human Disease. *Biomed. Pharmacother.* **2003**, *57* (3–4), 145–155.

(52) Li, Q.; Lancaster, J. R. Chemical Foundations of Hydrogen Sulfide Biology. *Nitric Oxide-Biol. Chem.* **2013**, *35*, 21–34.

(53) Weiss, E. A. Organic Molecules as Tools To Control the Growth, Surface Structure, and Redox Activity of Colloidal Quantum Dots. *Acc. Chem. Res.* **2013**, *46* (11), 2607–2615.

(54) Sun, L.; Diaz-Fernandez, Y. A.; Gschneidtner, T. A.; Westerlund, F.; Lara-Avila, S.; Moth-Poulsen, K. Single-Molecule Electronics: From Chemical Design to Functional Devices. *Chem Soc Rev* **2014**, *43* (21), 7378–7411.

(55) Weaver, A. L.; Gamelin, D. R. Photoluminescence Brightening via Electrochemical Trap Passivation in ZnSe and Mn2+-Doped ZnSe Quantum Dots. *J. Am. Chem. Soc.* **2012**, *134* (15), 6819–6825.

(56) Rinehart, J. D.; Weaver, A. L.; Gamelin, D. R. Redox Brightening of Colloidal Semiconductor Nanocrystals Using Molecular Reductants. *J. Am. Chem. Soc.* **2012**, *134* (39), 16175–16177.

(57) Sarkar, S.; Patra, B. K.; Guria, A. K.; Pradhan, N. The Redox Chemistry at the Interface for Retrieving and Brightening the Emission of Doped Semiconductor Nanocrystals. *J. Phys. Chem. Lett.* **2013**, *4* (12), 2084–2090.

(58) Feeney, R. E.; Yamasaki, R. B.; Geoghegan, K. F. Chemical Modification of Proteins: An Overview. In *Modification of Proteins*. *J. Am. Chem. Soc*, **1982**; 198, 3–55.

(59) García-Santamarina, S.; Boronat, S.; Hidalgo, E. Reversible Cysteine Oxidation in Hydrogen Peroxide Sensing and Signal Transduction. *Biochemistry* **2014**, *53* (16), 2560–2580.

(60) Cleland, W. W. Dithiothreitol, a New Protective Reagent for SH Groups. *Biochemistry* **1964**, *3* (4), 480–482.

(61) Szajewski, R. P.; Whitesides, G. M. Rate Constants and Equilibrium Constants for Thiol-Disulfide Interchange Reactions Involving Oxidized Glutathione. *J. Am. Chem. Soc.* **1980**, *102* (6), 2011–2026.

Chapter 4 - Mn^{2+}-ZnSe/ZnS@SiO_2 Nanoparticles for Turn-on Luminescence Thiol Detection

4-1 Introduction

Imaging of biological environments has become a critical strategy for the discovery and treatment of disease.[1–3] The ability to resolve microscopic events spatially and temporally has led to a multitude of imaging probes providing advances in resolution, sensitivity, targeting and even treatment.[4–7] Despite these advances, no one probe possesses all the properties necessary for comprehensive diagnostics. These limits have sparked an interest in combining imaging modalities, taking advantage of their complimentary abilities.[8,9] For example, good spatial resolution achieved by magnetic resonance imaging (MRI) may be combined with the high sensitivity of optical imaging. Thus, MRI may be used to pinpoint the position of a probe while optical imaging yields detailed information on the probe local environment. Development of new and improved multimodal probes is an active area of interdisciplinary research where advances have made earlier identification and real-time monitoring of various diseases possible.

Probes for optical imaging must be emissive, and preferably be photostable and absorb light at wavelengths in the near-infra red (NIR), where there is minimal absorption by tissue.[7,10,11] Although a variety of dyes are available, use of semiconductor nanocrystals (NCs) has become popular due to the many beneficial properties they possess.[12] In addition to their photostability and good emission quantum yields, they also have large one- and two-photon absorptions, narrow and tunable emission bands, and provide a scaffold for construction of nanoprobes.[3,11,13] NCs have been used in construction of magneto-optical imaging agents in several ways.[8] One of the simplest, both in design and synthesis, is incorporation of ions into the NC matrix.[14] This

design provided the benefits of co-localization and the need for only a single probe injection. The problem with use of doped NCs as magneto-optical imaging agents is the trade-off between luminescence quantum yield (QY) and concentration of paramagnetic ion.[15–18] At high dopant concentrations, useful for magnetic imaging, the luminescence is quenched.

Sensors of the intracellular environment are useful for detection of many analytes.[19–22] The high functionality of thiols within cells creates an immediate demand for the development of suitable probes for continuous and sensitive detection. Literature describes multiple detection methods for thiols and thiol-containing peptides,[23,24] but most of the available probes are based on organic dyes that are prone to photobleaching, produce broad photoluminescence (PL) spectra and are reliant on cellular extracts.One of the most abundant cellular thiols is the cysteine-containing tripeptide, glutathione (GSH). Optimum cellular ratios of reduced to oxidized GSH can lead to heart disease, cancer, stroke, and many neurological disorders.[25–27] GSH is a vital antioxidant for the detoxification of reactive oxygen species, and patients with dementia often have low concentrations of GSH within the brain.[24] The intracellular concentration GSH ranges from 1 to 15 mM, with concentrations across cellular compartments poorly established.[25,28] Therefore, development of a probe that is resistant to photobleaching and provides real time monitoring of GSH is of practical importance.

Mn^{2+}-doped wide bandgap semiconductors are used in many photo- and electroluminescent applications[29–31] and the availability of luminescent colloidal NCs of these materials expanded their use to bioimaging and sensing.[32–34] Figure 4-1a illustrates an energy level diagram for Mn^{2+}-doped wide bandgap semiconductors. After excitation, energy is rapidly transferred to the Mn^{2+} $^4T_1$ excited state relaxing to the $^6A_1$ ground state. This energy is released radiatively producing a peak centred near 590 nm. The UV-vis and PL of Mn^{2+}:ZnSe NCs in toluene is

shown in Figure 4-1b and a photograph of the NCs in toluene under UV light (Figure 4-1c) illustrates their bright, orange luminescence. To preserve this luminescence in aqueous solution a thick shell of ZnS is often added to the NC surface. This shell passivates the surface of the NCs and isolates them from their surrounding environment. For applications in which interaction between the NC and its surroundings are desired, such as sensing and MRI contrast, the use of these shells must be balanced with the requirement for interaction of the NC with its surroundings.

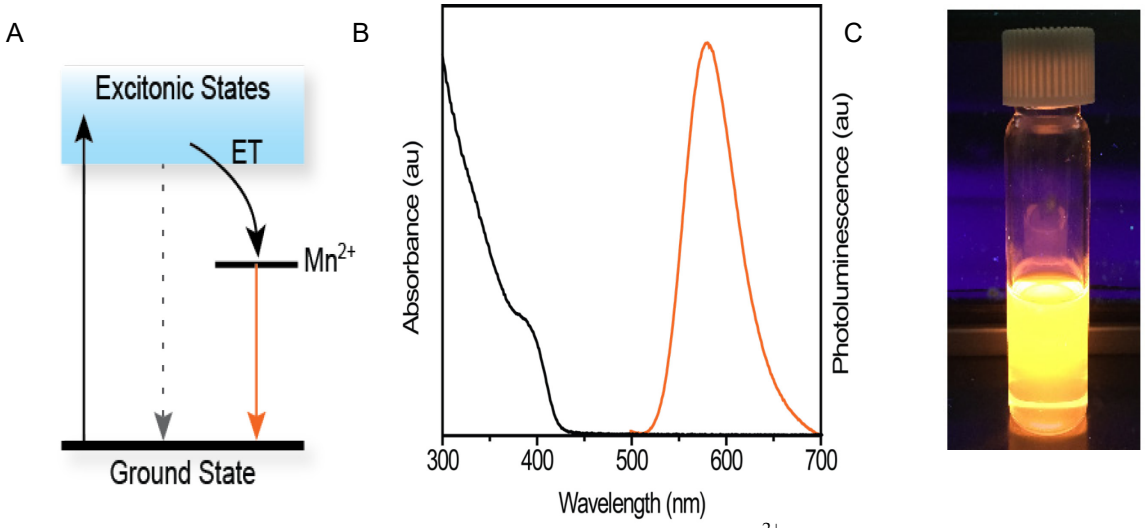

Figure 4-1.(a) Energy level diagram describing the Mn^{2+} luminescence process. Following photoexcitation of the semiconductor, energy is rapidly transferred from the semiconductor to the Mn^{2+} ion. The resulting luminescence is due to the $^4T_1 \rightarrow {}^6A_1$ spin-forbidden transition and is therefore long-lived. (b) UV-vis absorption and PL spectra of a Mn^{2+}:ZnSe NCs illustrating the large Stokes shift present in these materials. (c) Photograph of a solution of orange-emitting Mn^{2+}:ZnSe/ZnS NCs under UV light.

Here we address water-soluble Mn^{2+}:ZnSe/ZnS@SiO_2NPs that can optically sense biological thiols. As opposed to NPs encapsulated with a thick shell, having Mn^{2+} ions on or near the NP surface enables luminescence to be governed by surface chemistry. We take advantage of the NC surface chemistry to provide turn-on luminescence enhancement that is tunable with addition of

ZnS barrier layers. Using the NC surface directly, tunable sensitivity is obtained by increasing the ZnS shell thickness, decreasing the sensitivity of the probe to its surrounding environment. The design of NP sensors for biological environments by modifying their chemical surfaces expands opportunities for design of new probes and sensing modalities offering access to new applications in biomedicine.

Thiols are known to influence processes in biology and play key roles in nanodevices.[35–39] To explore the potential application of these Mn^{2+}-doped NCs as sensors, the luminescence of these NCs in the presence of thiol was studied. Of particular interest is the possibility of tuning the probe sensitivity using ZnS barrier layers. This prospect was first examined using Mn^{2+}:ZnSe core NCs in organic solvent. We impose enhanced NC luminescence sensitive to thiols by mitigating the NC-thiol interaction. Mitigation is achieved by varying the NC shell density and the corresponding luminescence change is caused by direct interaction between thiol and the NCs.

The goal of this chapter is to address/answer following questions:

I. How does the shell thickness affect the sensing property of core-shell Mn^{2+}:ZnSe/ZnS QDs?

II. Do the QDs give same performance in both aqouce and oeganic media?

4-2 Results and Discussion

Our NP sensors are synthesized in a multistep process described in detail in the methods section. Briefly, luminescent Mn^{2+}-doped core NCs form from lyothermal decomposition of a single-source precursor as described previously[14,40]. The reaction is monitored using UV-vis absorption during which a first-absorption feature corresponding to the ZnSe quantum dots grows in near

380 nm and red-shifts as the NCs increase in size. The small amount of Mn^{2+} precursor added prevents formation of MnSe, and the product core NCs exhibit properties corresponding mostly to their ZnSe lattice with the large exception of the PL, which corresponds to the Mn^{2+} $^4T_1 \rightarrow {}^6A_1$ transition observed near 590 nm (Figure 4-1b). The amount of Mn^{2+} was adjusted to provide bright PL and limited oxidation after exposure of the core NCs to air.

After core synthesis and isolation, shells of ZnS are added to the NCs using an adapted process.[41,42] Using the well-established selective ion adsorption and reaction (SILAR) method, monolayers (MLs) of Zn^{2+} and S^{2-} are added to the Mn^{2+}:ZnSe core NCs. To examine the effect of shell thickness, samples with thin (~1-2 MLs), medium (~4 MLs) and thick (~8-10 MLs) ZnS shells were prepared and used in all further experiments. These shells serve to both passivate surface defects and isolate the NC core from its surrounding environment. More isolation and surface passivation decreases the sensitivity of the NC to its local environment. For sensor design, this is key in tuning sensitivity.

4-2-1 Shell-thickness dependent thiol detection in organic solvent

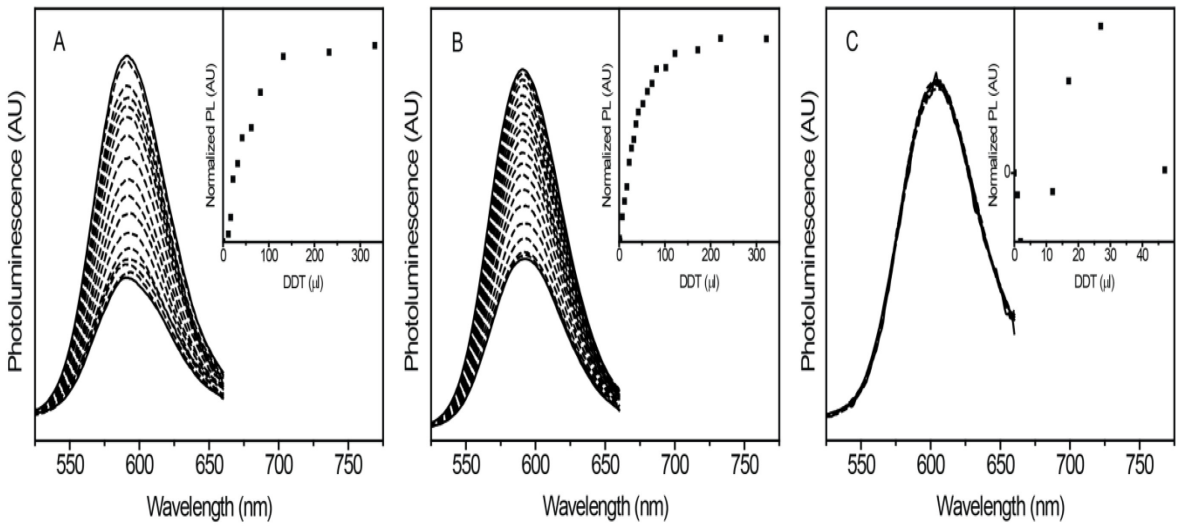

Figure 4-2 PL spectra of Mn^{2+}:ZnSe/ZnS NCs suspended in chloroform with:(a) thin, (b) medium,and (c) thick ZnS shells in the presence of increasing amounts of dodecanethiol (DDT).Insets: corresponding plots of normalized PL (PL change) with increasing thiol.The increase in PL in the presence of DDT is much larger for samples with medium shell thicknesses whereas the change in PL in the thick shell sample is negligible.

The luminescence response of the NCs to thiol was first tested in organic solvent. Following isolation from the reaction mixture, the NCs are soluble only in hydrophobic environments. The hydrophobic dodecanethiol (DDT) was used to test the thin shell NC response. As seen in Figure 4-2a, there is a large increase in Mn^{2+} luminescence with increasing amounts of DDT. A similar increase is observed when a medium thickness shell is added (Figure 4-2b), but only a negligible change for the thick shell sample (Figure 4-2c). Scatter plots of the PL intensity vs thiol show initial increases for thin (Figure 4-2a inset) and medium (Figure 4-2b inset) shell samples, but no change for the thick shell sample (Figure 4-2c inset). The scatter plot in Figure 4-2a shows an increase in PL up to ~75 μL DDT before saturating and the medium shell sample (Figure 4-2b inset) shows an increase in PL up to near 150 μL DDT before leveling out. This difference is also observed when comparing sensitivities for these similar sensors. As shell thickness increased, the sensitivity first increased, from thin to medium, followed by a large decrease from medium to thick, indicating these NPs are basically insensitive.

4-2-2 Thiol sensing in aqeuous solution

To use these probes for sensing biological thiols they must be transferred to aqueous solution. Methods for phase transfer such as simple ligand exchange were unsuccessful as the particles tended to aggregate and fall out of solution. The method that generated the best sensors was addition of a silica shell to the core/shell NCs using an adapted inverse micelle approach detailed

in the methods section.[43] The product NPs consist of a Mn^{2+}-doped ZnSe core with shells of ZnS and a coating or encapsulating layer of silica, which provides water dispersibility. The absorption and luminescence are retained in aqueous solution.

4-2-3 Luminescence enhancement with different thiols

Titrations of different thiols with these NPs were done in aqueous solution to characterize their specificity and scope. Four biologically relevant thiols with different molecular structures were chosen for the luminescence titrations with the NPs: dithiothreitol (DTT), N-acetyl cysteine (NAC), cysteine (CYS) and glutathione (GSH). Aqueous solutions of these thiols were made and titrated into NP solutions. PL spectra from an exemplary titration is shown in Figure 4-3a. Here, as the concentration of DTT increases from 0 to 20 μM, the NPs exhibit increasing Mn^{2+} PL. A scatter plot of PL intensity against [DTT] (Figure 4-3a inset) illustrates a linear increase in PL prior to a decrease at concentrations >20 μM. Similar luminescence enhancement is observed with other thiols. Figures 4-3b and 3c show luminescence increasing with different sensitivities to CYS and NAC, respectively. As the concentration of CYS increases from 0 to 25 μM, the NPs exhibit increasing Mn^{2+} PL (Figure 4-3b). The corresponding scatter plot of PL intensity against final [CYS] illustrates a linear increase prior to PL decreasing at concentrations >25 μM (Figure 4-3b inset). Similarly, for NAC the NPs exhibit increasing Mn^{2+} PL (Figure 4-3c) as the concentration of NAC increases from 0 to 40 μM, and the corresponding scatter plot shows a linear PL increase prior to decreasing at [NAC]>40 μM (Figure 4-3c inset).So, these NP sensors exhibit turn-on luminescence in the presence of several biologically relevant thiols. In addition to sensing different thiols, this enhancement extends to different luminescent materials of interest, namely Mn^{2+}:ZnCdSe/ZnS@SiO_2 dual-emitting NPs of interest for optical thermometry. As shown in Figure 4-4 the PL of both peaks increases in the presence of DTT. This turn-on

response is perpendicular to the ratiometric changes in dual-emission with temperature, high lighting the utility of this turn-on sensing mechanism with these NPs.

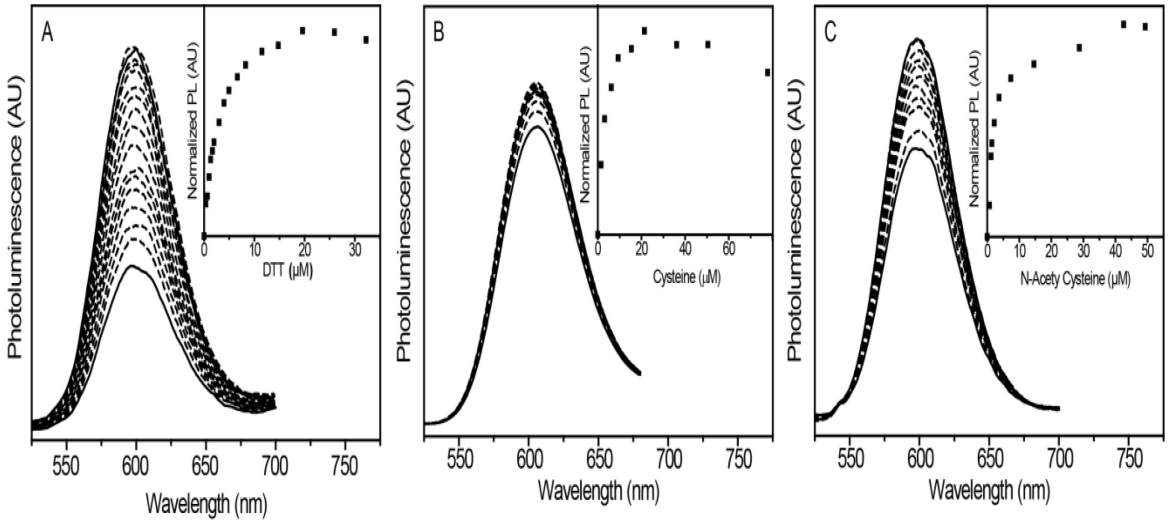

Figure 4-3 PL spectra of Mn^{2+}:ZnSe/ZnS@SiO_2NPs with medium ZnS shellsencapsulated in silica suspended in PBS with successive addition of 1 mM (a) dithiothreitol (DTT), (b) L-cysteine (CYS), and (c) N-acetylcysteine (NAC). Insets: corresponding plots of normalized PL (PL change) with increasing thiol.

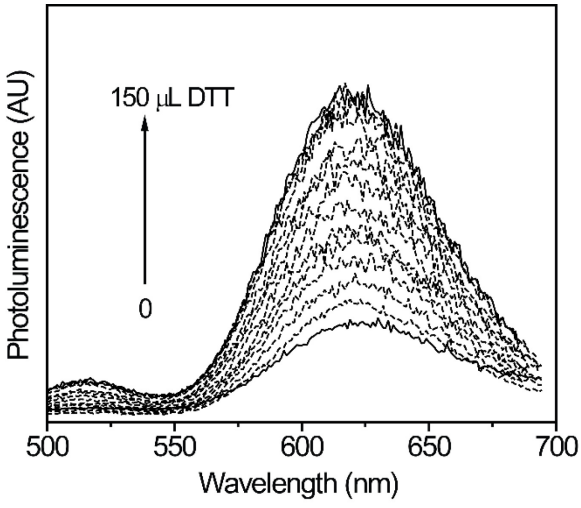

Figure 4-4 Photoluminescence spectra of Mn^{2+}-doped ZnCdSe NPs with medium ZnS shells encapsulated in silica suspended in PBS with successive addition of 1 mM dithiothreitol (DTT).

4-2-4 Glutathione sensing with different shell thicknesses

In addition to the three thiols used in the previous section, the NPs also exhibited turn-on luminescence with GSH. To see if the tunability of the sensors using shell thickness extended to aqueous solution, we prepared Mn^{2+}:ZnSe/ZnS@SiO_2 NPs with varying ZnS densities: thin, medium, and thick. The NPs with a thin ZnS shell did not suspend well in aqueous solution and their PL was too low to obtain good signal-to-noise. But, titrations of NPs with medium ZnS shells showed enhanced Mn^{2+} luminescence with increasing amounts of GSH (Figure 4-5a). Importantly, the probe luminescence was sensitive enough to differentiate GSH at concentrations of 0 to 22μM (Figure 4-5a inset). To assess if the sensitivity is tunable by adjusting the ZnS shell thickness, aqueous GSH titrations were also performed with NPs consisting of a thick ZnS shell (Figure 4-5b). The inset of Figure 4-5b shows the PL intensity initially increased a small amount before rapidly leveling off. No significant intensity change was measured between concentrations ranging from 9 to 420 μM. This experiment supports the notion that with increasing surface protection and passivation through ZnS shells, the NP sensitivity is greatly reduced. The overall decrease in brightness is most likely attributed to the formation of an alternative annihilation pathway for the excited exciton to travel often ascribed to defects present at core-thick shell interfaces.

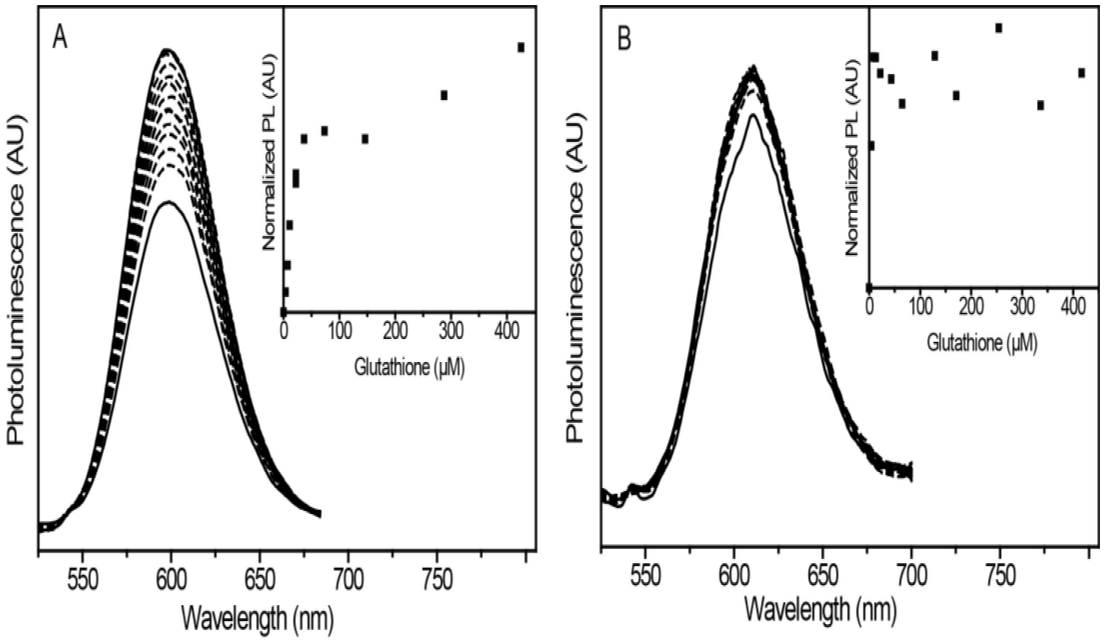

Figure 4-5 (a) PL spectra of Mn^{2+}:ZnSe/ZnS@SiO_2 NPs with medium ZnS shells suspended in PBS with successive addition of 10 mM L-glutathione (GSH). As the concentration of GSH increases from 0 – 25 μM, the Mn^{2+} PL simultaneously increases. (b) PL spectra of Mn^{2+}:ZnSe/ZnS@SiO_2 NPs with thick ZnS shells suspended in PBS with successive addition of 10 mM GSH. The Mn^{2+} PL increases as [GSH] approaches ~10 μM, and quickly levels off. Insets: corresponding plots of normalized PL (PL change) with increasing thiol.The medium shell sample shows linear PL restoration prior to plateauing at 37 μM. The thick shell sample shows nearly immediate stagnant PL response towards with no significant change in PL response over a range of 9-420 μM.

4-2-5 Thiol selectivity

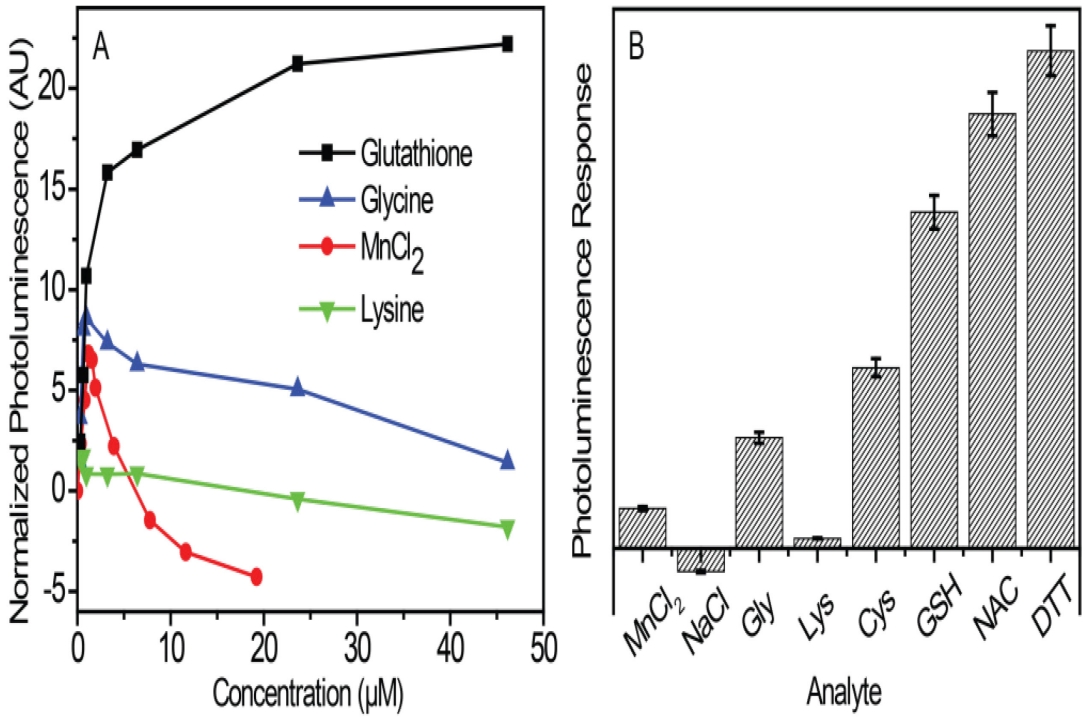

Figure 4-6: (a) Scatter plot of normalized Mn^{2+}:ZnSe/ZnS@SiO_2 PL vs analyte concentration for GSH, GLY, $MnCl_2$, and LYS.(b) PL response of NP solutions in the presence of various analytes. Relative intensities were obtained by averaging the PL response as a function of concentration. Multiple regression analysis results indicate all control analyte PL intensities were significantly less than GSH, NAC, and DTT.

Although sensitivity to several analytes can be advantageous under some conditions, broad analyte enhancement of NP PL limits the utility of these sensors. Further investigation of additional biological analytes revealed salts and amino acids did not induce sufficient optical emission (Figure 4-6). Figure 4-6a shows a scatter plot of the PL change of these NPs in the presence of GSH and several other analytes. Although the NP PL increases at first for both glycine (GLY) and $MnCl_2$, a rapid decrease follows beyond a concentration of few μM. The PL spectrum of NPs and lysine (LYS) exhibits a small decrease initially before a continuous decrease at concentrations approaching 45 μM. PL spectra with corresponding scatter plots can

be found in the SI (Figures 4-7 to 4-10). Further analysis of this data and that for other analytes is plotted in Figure 4-6b. ANOVA and multiple regression variance tests indicate that the thiols tested produced stronger PL responses than control analytes. NAC and DTT exhibited a p-value threshold of 0.02 and GSH a value of 0.07. The signal response of the NPs is very selective towards biological thiols relative to other salts and amino acids.

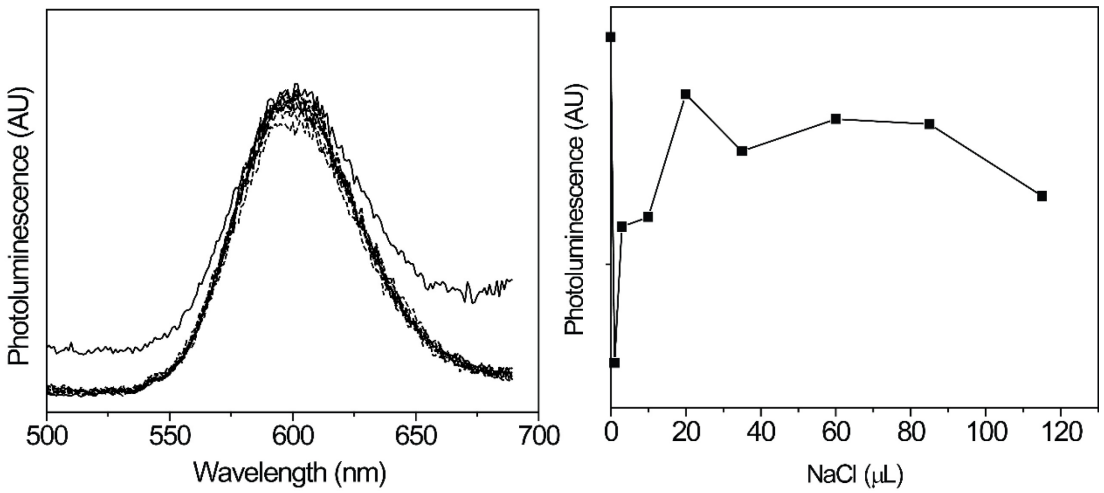

Figure 4-7: Left: Photoluminescence spectra of Mn^{2+}:ZnSe/ZnS@SiO_2 NPs with medium ZnS shells encapsulated in silica suspended in PBS with successive addition of 1 mM NaCl. Right: Corresponding scatter plot.

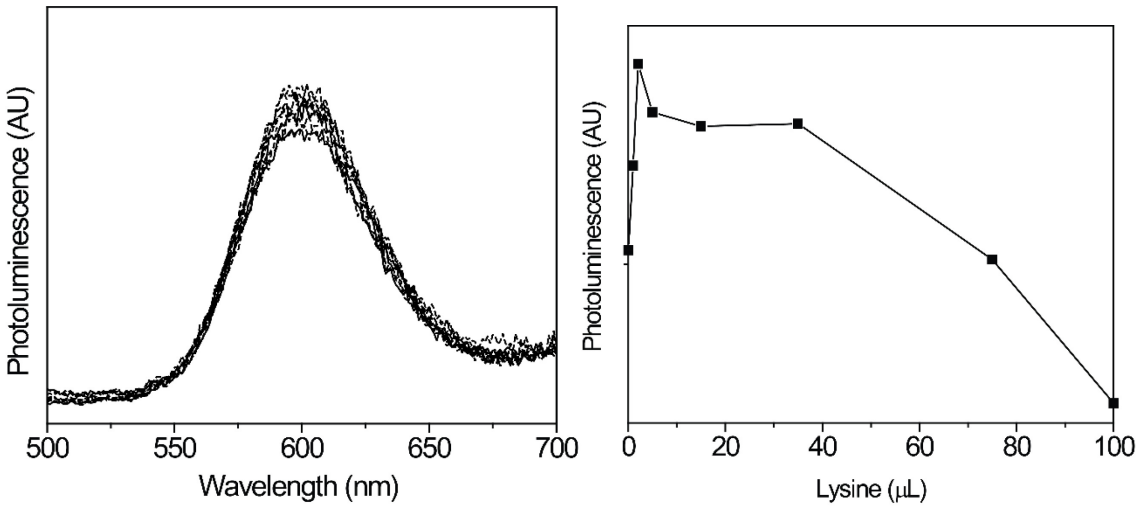

Figure 4-8: Left: Photoluminescence spectra of Mn^{2+}:ZnSe/ZnS@SiO_2 NPs with medium ZnS shells encapsulated in silica suspended in PBS with successive addition of 1 mM lysine (LYS). Right: Corresponding scatter plot.

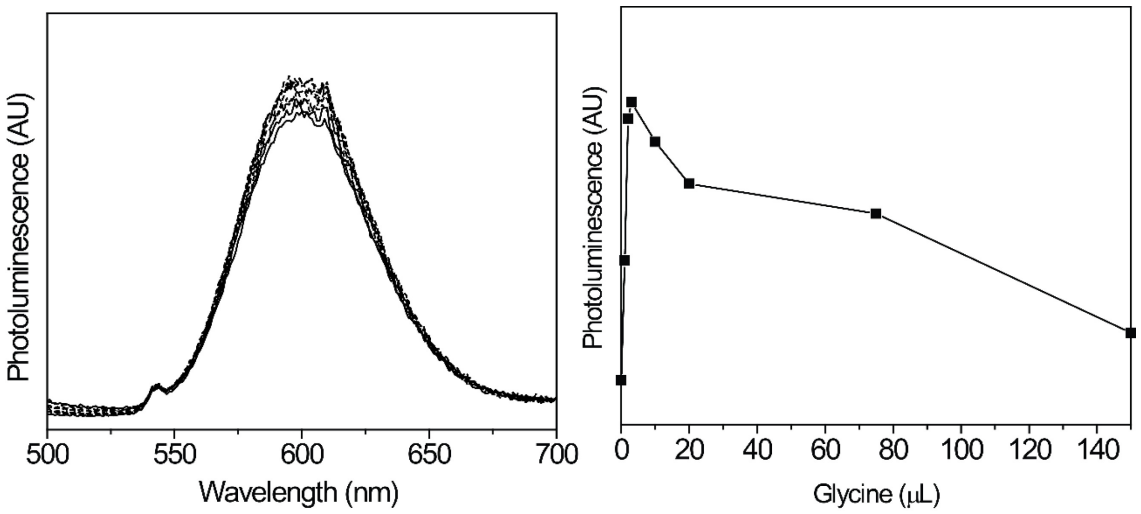

Figure 4-9: Left: Photoluminescence spectra of Mn^{2+}:ZnSe/ZnS@SiO_2 NPs with medium ZnS shells encapsulated in silica suspended in PBS with successive addition of 1 mM glycine (GLY). Right: Corresponding scatter plot.

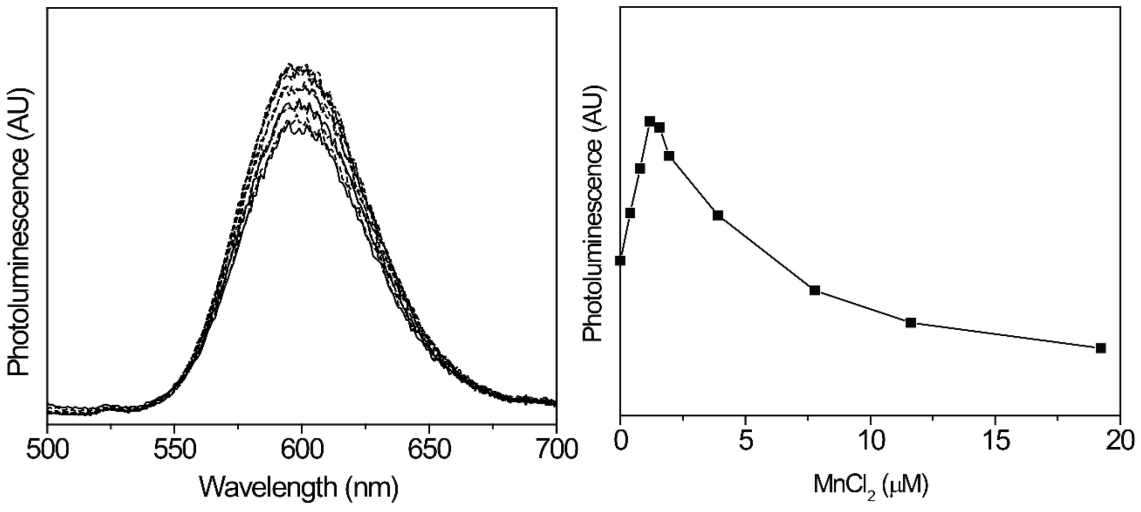

Figure 4-10: Left: Photoluminescence spectra of Mn^{2+}:ZnSe/ZnS@SiO_2 NPs with medium ZnS shells encapsulated in silica suspended in PBS with successive addition of 1 mM $MnCl_2$. Right: Corresponding scatter plot.

4-2-6 Prospects for multimodal imaging and sensing

Mn^{2+}-containing materials can be used as contrast agents in MRI. To assess the potential use of these NPs as bimodal imaging agents and sensors, we examined their magnetic properties in the presence and absence of DTT.Addition of thiol to the NPs increases the Mn^{2+} PL likely through interaction of the thiol with the NP surface. The exact nature of the enhancement is not certain but is probably due to passivation of surface defects through reduction of oxidized ions on or near the NP surface. If these are Mn ions, a change in magnetic properties could be observed. Based on the thiol-NP PL data, we also expect the medium shell thickness sample to exhibit more of a change than the thick shell sample in the presence and absence of thiol. The medium shell sample should also exhibit faster relaxation because the Mn^{2+} are more isolated from the surface in the thick shell sample. The T_1 values measured for these Mn^{2+}:ZnSe/ZnS@SiO_2 NPs (Table S1) are very similar for all NP samples despite shell thickness or thiol presence. Also evident from the table is the small difference between the relaxation times for the blank samples (water) and those of the samples with NPs. This indicates the effect of the NPs on relaxation time is small under these conditions. This is not surprising as the concentrations of NPs needed for optical imaging are much smaller than those required for MR imaging. The low concentration of Mn^{2+} in the samples and the isolation of these cations from their surroundings by the shells and layers of other material added would also decrease the effect of the NPs on relaxation time. These results highlight the additional challenges in multimodal sensor design for luminescence

and magnetism. Optimizing a sample for optical imaging and sensing of an analyte in a specific concentration range can limit the usefulness of the probe for magnetic measurements. These NPs designed for tunable thiol sensing are not optimized for use in magnetism, but the potential for multiparameter control provides an enticing opportunity for sensor design and development.

Analytes	*p*-value
GSH-DTT	0.6064518
GLY-DTT	0.0002633
LYS-DTT	0.0000016
$MnCl_2$-DTT	0.0000015
NAC-DTT	0.9267174
NaCl-DTT	0.0000001
GLY-GSH	0.0705745
LYS-GSH	0.0019124
$MnCl_2$-GSH	0.0030278
NAC-GSH	0.9976071
NaCl-GSH	0.0002704
LYS-GLY	0.9137878
$MnCl_2$-GLY	0.9808447
NAC-GLY	0.0175741
NaCl-GLY	0.7065187
$MnCl_2$-LYS	0.9997852
NAC-LYS	0.0003176
NaCl-LYS	0.9997029
NAC-$MnCl_2$	0.0004637
NaCl-$MnCl_2$	0.9847784
NaCl-NAC	0.0000373

Table 4-1 *p*-values for thiols and control analytes**.**

Run	NCs (s)	+DT T (s)	Water (s)
1	2.54888	2.63426	2.60044
2	2.53549	2.71390	2.69495
3	2.59246	2.64803	2.59054
4	2.63351	2.64220	2.61833

Table 4-2 T_1 values for medium shell Mn^{2+}:ZnSe/ZnS@SiO_2 NPs before and after thiol addition.

4-3 Summary

Mn^{2+}-doped NCs exhibit turn-on luminescence in the presence of thiols. Tunable sensitivity is obtained simply by changing the thickness of the ZnS barrier shell, controlling the ability of thiol to interact with the NC surface. This behavior, first observed in organic solvent, can be preserved in aqueous solution when a silica shell is added to the NCs. This is demonstrated by luminescence enhancement with several thiols of interest. Using several control analytes, the NPs are shown to be selective for thiols, although not necessarily able to distinguish between thiols. Optimization for a desired sensing range is possible for the concentrations and analytes included here. Mn^{2+}-doped NPs have potential for multimodal imaging, although these probes, designed for tunable thiol sensing, are not optimized for use in MRI. Nevertheless, these NPs are stable within aqueous environments and superior to other opticalsensing agents such as organic dyes.These findings are helpful in enabling further investigation of intracellular sensing of GSH and other thiols. The potential for tunable control over luminescent and magnetic properties

provides an attractive opportunity for multimodal sensor advancement.Further development hinges on successful deployment of these NPs in biological environments and balance of magnetic and optical properties to mitigate the decrease in sensitivity and brightness but still achieve enhanced relaxation times.

4-4 Materials and Methods

All the chemicals used are commercially available and were used without further purification; Manganese(II) chloride tetrahydrate ($MnCl_2$•$4H_2O$, 99.99%), L-glutathione reduced (≥98.0%), Sodium chloride (NaCl, ≥99%), oleylamine (OLA, ≥98%), dodecanethiol (DDT, ≥98%), Agerose, selenium (≥99.5%), sulfur (≥99.5%), tetramethylammonium chloride (NMe_4Cl, ≥98%), triethylamine (TEA, ≥99%), octadecene (ODE, 90%), IGEPAL (CA-520, CA-630, CA-720), tetraethylorthosilicate (TEOS, 99.999%), ammonium hydroxide solution (NH_4OH, 7N), agarose, cyclohexane, toluene, water, phosphate buffered saline (PBS), and chloroform from Aldrich, N-acetylcysteine (98%), phenylselenol (PhSeH, 98%) and methanol (MeOH) from Acros, zinc nitrate hexahydrate ($Zn(NO_3)_2$•$6H_2O$, ≥99%) from J. T. Baker, acetone, dithiothreitol (DTT), glycine (≥98.5%), cysteine (≥99.5%), and L-lysine (≥98.5%) from Fisher.

4-4-1 $[NMe_4]_2[Zn_4(SePh)_{10}]$

The cluster precursor was prepared by adapting previous methods.[44,45] Three separate solutions were prepared and degassed for 30-60 minutes by bubbling with N_2: 1) $Zn(NO_3)_2$•$6H_2O$ (7.318 g) in 35 mL MeOH, 2) Me_4NCl (4.42 g) in 20 mL MeOH, and 3) TEA (9.5 g) in 20 mL MeOH. Under a N_2 overpressure, PhSeH (10 g) was added to solution 3, followed by stirring for 20 minutes. Solution 1 was then transferred to solution 3 dropwise via cannula, forming a cloudy solution. Next, solution 2 was cannula transferred to solution 3 over a period of 10-30 min,

followed by cooling in an ice bath for 30 minutes. The solid was then filtered and rinsed thoroughly with MeOH and toluene, yielding a white powder.

4-4-2 Mn^{2+}:ZnSe and Mn^{2+}:ZnCdSe Nanocrystals

Colloidal Mn^{2+}:ZnSe NCs were synthesized by adapting previously described methods.[14,45] Briefly, OLA (10 g), $MnCl_2 \cdot 4H_2O$ (0.0012 g, 6.1 μmol), and for the ZnCdSe alloys $CdCl_2 \cdot 2.5H_2O$ (0.0146 g, 64μmol), were combined in a flask and degassed at 100 °C under vacuum for 120 minutes. After cooling below 80 °C, the cluster precursor (0.2 g, 0.1 mmol) and Se (0.0108 g, 0.137 mmol) were added under N_2 overpressure. After briefly degassing the solution under vacuum at 100 °C, the reaction is heated to 280 °C under N_2 and the NCs are grown at this temperature for 15 minutes. After cooling below 80 °C, the NCs were isolated by precipitation and resuspension with methanol and toluene, respectively.

4-4-3 ZnS passivation shell growth

For addition of zinc sulfide to the nanocrystal surfaces, a previously reported procedure was adapted[42]. First, core particles, suspended in a small amount of toluene (about 25-50% of a core synthesis, above) were added to a 50 mL three-neck flask containing octadecene (ODE, 1.5 g) and oleylamine (OLA, 1.5 g). The reaction flask was kept under vacuum at 100 °C for 30 minutes. Under a nitrogen atmosphere, the reaction was heated to 220 °C, at which point an ODE solution containing zinc oleate (0.2 M) was added to the nanocrystal suspension over a period of 3-4 minutes, by syringe. The zinc precursor was allowed to react for 25 minutes prior to the addition of the sulfur precursor. A solution of sulfur in ODE (ODE-S), formed by combining elemental sulfur (1 mmol) and ODE (5 mL), was added to the core solution over a period of 5 minutes, using a syringe pump. The precursors were allowed to react for 25 minutes prior to the addition of more zinc precursor. This process was repeated until the desired shell thickness was

reached. Following synthesis, these nanocrystals were washed by repeated precipitation with ethanol and resuspension in toluene.

4-4-4 Water-soluble Mn^{2+}:ZnSe Nanoparticles

A previous procedure was adapted to form silica encapsulated NCs soluble in aqueous solution[43].Core/shell NCs were washed by repeated precipitation with acetone and resuspension in chloroform. Silica shells were prepared by adding IGEPAL (1.3 mL, CA-520, CA-630 or CA-720) to glass vials containing cyclohexane (10 mL). This solution was stirred for 30 minutes before 200 μL of dispersed NCswere added. After stirring for 15 minutes, TEOS (80 μL) was added and the solution was stirred for 10 minutes. Finally, NH_4OH solution (150 μL) was added and samples were stirred overnight.

4-4-5 Agarose gel protocol

A uniform solution of 0.05 g agarose in 5 mL water was prepared using a hot bath and then after cooling the solution to about 70 °C, 1 mL of aqueous solution of desired NPs was added to it and mixed thoroughly. The mixture was sonicated until an air-bubble free gel formed.

4-4-6 Physical measurements

In this study a Cary 5000 UV-vis-NIR spectrophotometer was used for recording UV-vis absorption spectra. A PTI Quanta Master 400 fluorometer was used to record PL spectra and perform thiol titration experiments. The samples were prepared in a cuvette with a stir bar. A syringe pump was used for the titration with injection of thiol via a syringe as described previously[46]. While stirring, spectra were taken at intervals of 2-30 minutes, depending on sample brightness and sensitivity. Titrations were done until luminescence saturation or decrease. For

MRI measurements, a sample of Mn^{2+}:ZnSe/ZnS@SiO_2 was diluted in 5 mL distilled water and divided into two tubes. Then, DTT (0.0224 g, 0.15 mmol)was added to one of them The longitudinal relaxation time of these samples was determined using an inversion recovery pulse sequence using a 14.1 T NMR system (Bruker Avance III, WB, 600 MHz NMR-MRI).

4-5 Conclusion

Our results show that the shell thickness of Mn:ZnSe@ZnS QDs affects the sensing properties of NCs significantly. The thick shell prevents interactions of matrix components with Mn(II) ion in both organic and aqueous medium resulting no sensing performance of QDs. The QDs with thin shell have sensing performance both in organic and aqueous medium. The QDs with thin shell has high sensitivity in organic solvents, but they lose their sensing property in aqueous medium permanently.

4-6 References

(1) Kelkar, S. S.; Reineke, T. M. Theranostics: Combining Imaging and Therapy. *Bioconjug. Chem.* **2011**, *22* (10), 1879–1903.

(2) Blasberg, R.; Piwnica-Worms, D. Imaging: Strategies, Controversies, and Opportunities. *Clin. Cancer Res.* **2012**, *18* (3), 631–637.

(3) Lim, E.-K.; Kim, T.; Paik, S.; Haam, S.; Huh, Y.-M.; Lee, K. Nanomaterials for Theranostics: Recent Advances and Future Challenges. *Chem. Rev.* **2015**, *115* (1), 327–394.

(4) Chen, G.; Roy, I.; Yang, C.; Prasad, P. N. Nanochemistry and Nanomedicine for Nanoparticle-Based Diagnostics and Therapy. *Chem. Rev.* **2016**, *116* (5), 2826–2885.

(5) Li, C. A Targeted Approach to Cancer Imaging and Therapy. *Nat. Mater.* **2014**, *13* (2), 110–115.

(6) Smith, B. R.; Gambhir, S. S. Nanomaterials for In Vivo Imaging. *Chem. Rev.* **2017**, *117* (3), 901–986.

(7) Bulte, J. W. M.; Modo, M. M. J. Introduction: The Emergence of Nanoparticles as Imaging Platform in Biomedicine. In *Nanoparticles in Biomedical Imaging*; Bulte, J. W. M., Modo, M. M. J., Eds.; Fundamental Biomedical Technologies; Springer New York, 2008; pp 1–5.

(8) Louie, A. Multimodality Imaging Probes: Design and Challenges. *Chem. Rev.* **2010**, *110* (5), 3146–3195.

(9) Garcia, J.; Tang, T.; Louie, A. Y. Nanoparticle-Based Multimodal PET/MRI Probes. *Nanomed.* **2015**, *10* (8), 1343–1359.

(10) Bose, A.; Wui Wong, T. Chapter 11 - Nanotechnology-Enabled Drug Delivery for Cancer Therapy A2 - Thomas, Sabu. In *Nanotechnology Applications for Tissue Engineering*; Grohens, Y., Ninan, N., Eds.; William Andrew Publishing: Oxford, **2015**; pp 173–193.

(11) *Principles of Fluorescence Spectroscopy*; Lakowicz, J. R., Ed.; Springer US: Boston, MA, 2006.

(12) Bruchez, M.; Moronne, M.; Gin, P.; Weiss, S.; Alivisatos, A. P. Semiconductor Nanocrystals as Fluorescent Biological Labels. *Science* **1998**, *281* (5385), 2013–2016.

(13) Medintz, I. L.; Uyeda, H. T.; Goldman, E. R.; Mattoussi, H. Quantum Dot Bioconjugates for Imaging, Labelling and Sensing. *Nat. Mater.* **2005**, *4* (6), 435–446.

(14) Cumberland, S. L.; Hanif, K. M.; Javier, A.; Khitrov, G. A.; Strouse, G. F.; Woessner, S. M.; Yun, C. S. Inorganic Clusters as Single-Source Precursors for Preparation of CdSe, ZnSe, and CdSe/ZnS Nanomaterials. *Chem. Mater.* **2002**, *14* (4), 1576–1584.

(15) Yang, H.; Santra, S.; Holloway, P. H. Syntheses and Applications of Mn-Doped II-VI Semiconductor Nanocrystals. *J. Nanosci. Nanotechnol.* **2005**, *5* (9), 1364–1375.

(16) Beaulac, R.; Archer, P. I.; Gamelin, D. R. Luminescence in Colloidal Mn2+-Doped Semiconductor Nanocrystals. *J. Solid State Chem.* **2008**, *181* (7), 1582–1589.

(17) Jahanbin, T.; Gaceur, M.; Gros-Dagnac, H.; Benderbous, S.; Merah, S. A. High Potential of Mn-Doped ZnS Nanoparticles with Different Dopant Concentrations as Novel MRI Contrast Agents: Synthesis and in Vitro Relaxivity Studies. *J. Nanoparticle Res.* **2015**, *17* (6), 1–12.

(18) Wang, Y.; Wu, B.; Yang, C.; Liu, M.; Sum, T. C.; Yong, K.-T. Synthesis and Characterization of Mn:ZnSe/ZnS/ZnMnS Sandwiched QDs for Multimodal Imaging and Theranostic Applications. *Small* **2016**, *12* (4), 534–546.

(19) Rabinowitz, J. D.; Vacchino, J. F.; Beeson, C.; McConnell, H. M. Potentiometric Measurement of Intracellular Redox Activity. *J. Am. Chem. Soc.* **1998**, *120* (10), 2464–2473.

(20) Han, J.; Burgess, K. Fluorescent Indicators for Intracellular PH. *Chem. Rev.* **2010**, *110* (5), 2709–2728.

(21) Ruedas-Rama, M. J.; Walters, J. D.; Orte, A.; Hall, E. A. H. Fluorescent Nanoparticles for Intracellular Sensing: A Review. *Anal. Chim. Acta* **2012**, *751*, 1–23.

(22) Kerr, C. A.; Rica, R. de la. Photoluminescent Nanosensors for Intracellular Detection. *Anal. Methods* **2015**, *7* (17), 7067–7075.

(23) Hee Lee, M.; Seung Kim, J.; L. Sessler, J. Small Molecule-Based Ratiometric Fluorescence Probes for Cations, Anions, and Biomolecules. *Chem. Soc. Rev.* **2015**, *44* (13), 4185–4191.

(24) Chew, O.; Whelan, J.; Millar, A. H. Molecular Definition of the Ascorbate-Glutathione Cycle in Arabidopsis Mitochondria Reveals Dual Targeting of Antioxidant Defenses in Plants. *J. Biol. Chem.* **2003**, *278* (47), 46869–46877.

(25) Montero, D.; Tachibana, C.; Rahr Winther, J.; Appenzeller-Herzog, C. Intracellular Glutathione Pools Are Heterogeneously Concentrated. *Redox Biol.* **2013**, *1* (1), 508–513.

(26) Paul, B. D.; Sbodio, J. I.; Xu, R.; Vandiver, M. S.; Cha, J. Y.; Snowman, A. M.; Snyder, S. H. Cystathionine γ-Lyase Deficiency Mediates Neurodegeneration in Huntington/'s Disease. *Nature* **2014**, *509* (7498), 96–100.

(27) Schumacher, D. M.; Metzler, M.; Lehmann, L. Mutagenicity of the Mycotoxin Patulin in Cultured Chinese Hamster V79 Cells, and Its Modulation by Intracellular Glutathione. *Arch. Toxicol.* **2005**, *79* (2), 110–121.

(28) van 't Erve, T. J.; Wagner, B. A.; Ryckman, K. K.; Raife, T. J.; Buettner, G. R. The Concentration of Glutathione in Human Erythrocytes Is a Heritable Trait. *Free Radic. Biol. Med.* **2013**, *65*, 742–749.

(29) Jüstel, T. Phosphors for Plasma Display Panels. In *Luminescence*; Ronda, C., Ed.; Wiley-VCH Verlag GmbH & Co. KGaA, 2008; pp 61–73.

(30) Blasse, G.; Grabmaier, B. C. Lamp Phosphors. In *Luminescent Materials*; Springer Berlin Heidelberg, 1994; pp 108–133.

(31) Beaulac, R.; Ochsenbein, S. T.; Gamelin, D. R. Colloidal Transition-Metal-Doped Quantum Dots. In *Nanocrystal Quantum Dots, Second Edition*; Klimov, V. I., Ed.; CRC Press: Boca Raton, FL, USA, 2010; pp 397–453.

(32) Thakar, R.; Chen, Y.; Snee, P. T. Efficient Emission from Core/(Doped) Shell Nanoparticles: Applications for Chemical Sensing. *Nano Lett.* **2007**, *7* (11), 3429–3432.

(33) Santra, S.; Dutta, D. Quantum Dots for Cancer Imaging. In *Nanoparticles in Biomedical Imaging*; Bulte, J. W. M., Modo, M. M. J., Eds.; Fundamental Biomedical Technologies; Springer New York, 2008; pp 463–485.

(34) Wu, P.; Yan, X.-P. Doped Quantum Dots for Chemo/Biosensing and Bioimaging. *Chem. Soc. Rev.* **2013**, *42* (12), 5489–5521.

(35) Donhauser, Z. J.; Mantooth, B. A.; Kelly, K. F.; Bumm, L. A.; Monnell, J. D.; Stapleton, J. J.; Price, D. W.; Rawlett, A. M.; Allara, D. L.; Tour, J. M.; et al. Conductance Switching in Single Molecules Through Conformational Changes. *Science* **2001**, *292* (5525), 2303–2307.

(36) Townsend, D. M.; Tew, K. D.; Tapiero, H. The Importance of Glutathione in Human Disease. *Biomed. Pharmacother.* **2003**, *57* (3–4), 145–155.

(37) Li, Q.; Lancaster, J. R. Chemical Foundations of Hydrogen Sulfide Biology. *Nitric Oxide-Biol. Chem.* **2013**, *35*, 21–34.

(38) Weiss, E. A. Organic Molecules as Tools To Control the Growth, Surface Structure, and Redox Activity of Colloidal Quantum Dots. *Acc. Chem. Res.* **2013**, *46* (11), 2607–2615.

(39) Sun, L.; Diaz-Fernandez, Y. A.; Gschneidtner, T. A.; Westerlund, F.; Lara-Avila, S.; Moth-Poulsen, K. Single-Molecule Electronics: From Chemical Design to Functional Devices. *Chem Soc Rev* **2014**, *43* (21), 7378–7411.

(40) Archer, P. I.; Santangelo, S. A.; Gamelin, D. R. Inorganic Cluster Syntheses of TM2+-Doped Quantum Dots (CdSe, CdS, CdSe/CdS): Physical Property Dependence on Dopant Locale. *J. Am. Chem. Soc.* **2007**, *129* (31), 9808–9818.

(41) Li, J. J.; Wang, Y. A.; Guo, W.; Keay, J. C.; Mishima, T. D.; Johnson, M. B.; Peng, X. Large-Scale Synthesis of Nearly Monodisperse CdSe/CdS Core/Shell Nanocrystals Using Air-Stable Reagents via Successive Ion Layer Adsorption and Reaction. *J. Am. Chem. Soc.* **2003**, *125* (41), 12567–12575.

(42) McLaurin, E. J.; Vlaskin, V. A.; Gamelin, D. R. Water-Soluble Dual-Emitting Nanocrystals for Ratiometric Optical Thermometry. *J. Am. Chem. Soc.* **2011**, *133* (38), 14978–14980.

(43) Lian, J.; Xu, Y.; Lin, M.; Chan, Y. Aqueous-Phase Reactions on Hollow Silica-Encapsulated Semiconductor Nanoheterostructures. *J. Am. Chem. Soc.* **2012**, *134* (21), 8754–8757.

(44) Dance, I. G.; Choy, A.; Scudder, M. L. Syntheses, Properties, and Molecular and Crystal Structures of (Me4N)4[E4M10(SPh)16] (E = Sulfur or Selenium; M = Zinc or Cadmium): Molecular Supertetrahedral Fragments of the Cubic Metal Chalcogenide Lattice. *J. Am. Chem. Soc.* **1984**, *106* (21), 6285–6295.

(45) Vlaskin, V. A.; Beaulac, R.; Gamelin, D. R. Dopant−Carrier Magnetic Exchange Coupling in Colloidal Inverted Core/Shell Semiconductor Nanocrystals. *Nano Lett.* **2009**, *9* (12), 4376–4382.

(46) Yazdanparast, M. S.; Webb, M. T.; McLaurin, E. J. Single-Step Synthesis of Hyperbranched, Luminescent Mn2+-Doped ZnSe1−xSx Nanocrystals Using Dichalcogenide Precursors. *J. Mater. Chem. C* **2016**, *4* (28), 6907–6913.

Chapter 5 - Mild condition post-synthetic modification of InP QDs

5-1 Introduction

Colloidal NCs have a lot of applications in a variety of devices such as photocatalysis[1–4], light emitting diods[5,6], displays[7–9] and solar sells.[10–14] In colloidal inorganic nanocrystals, more than half of the atoms can be at the surface[15] and due to that, properties of these materials can be significantly affected by the chemistry of their surface.[7,16–21] Due to that, a lot of studies are done on the modification of the surface of NCs especially in case of the quantum dots (QDs) in which the optical properties are very sensitive to the surface chemistry of particles.[16,22–25]

Because of the high toxicity of cadmium, indium-based quantum dots, notably InP, have attracted a lot of attractions due to their emission in the visible region of electromagnetic spectra.[26–30] One of the aspects of the studies on InP quantum dots is improving optoelectronic properties through surface passivation using inorganic ligands. There are reports on using ionic-liquids for in situ ligand-striping and etching of InP QDs. In these studies, a long reaction time used for HF generation from the decomposition of ionic liquids.[31,32] The drawback of in situ formation of HF at high temperature is long reaction time. Ramasamy et al. reported a new technical procedure for the synthesis of InP QDs with narrow size distribution and shown that besides slow heating of reaction mixture, the reaction mixture needs to be kept at high temperature for a very short time to minimize size distribution broadening caused by the Ostwald ripening process.[33] With that, in case of in situ HF etching, long reaction time causes more ligand stripping and etching but also size distribution broadening due to Ostwald ripening.

Moreover, materials that are in the reaction mixture affect the synthesis of NCs. Koh et al. showed that the formation of highly reactive intermediate species in the mixture of indium myristate and tris methylsilyle phosphine cause formation of NCs with broad size distribution in fast heating synthesis, but in presence of Zn(II), different intermediate will be formed which leads formation of NCs with narrow size distribution.[34] Also, it has been shown that impurities can affect the NCs synthesis and surface properties. For instance, it is shown that an unusual long degassing process in the synthesis of PbS is necessary. Trace water generates hydroxyl groups which coordinate to the intermediate clusters and affect the size and surface properties of the final nanoparticle.[35] In the case of InP NCs, at the early stage of synthesis, water interacts with phosphorus precursors[36], and at the late stage of the synthesis, hydrolysis of water affect the intraparticle processes.[37] These both affect the size distribution of NCs. Water can be introduced to the reaction as an impurity or as a product of decarboxylation reaction[38], amidation reaction.[37] As the continent of water is dependent on the purity of reactants and the reaction time and temperature, controlling the size and size distribution of NCs has been challenging. Introducing more reactants to the reaction mixture of InP synthesis for in situ modifications can affect the water content of the reaction mixture both as an impurity and as a product of side reactions. On the other hand, anions also affect the synthesis due to their different effects on the stabilization of NCs.[39]

The post-synthetic modification has also used for surface passivation of InP NCs. The advantage of this method is that as the etching process is carried out after the synthesis, one can have better control over synthesis of NCs. Micic et al. showed that the HF etching of InP as a post-synthetic modification removes long lifetime defect luminescence by removing or passivating surface states and yields high quantum yield. They claimed that phosphorus vacancies act as a trap and

causes long red-shifted emission and etching has no effect on the band-edge emission of the InP QDs which has short red shifted[40]. They believe that upon HF or NH_4F etching post-synthetic modification, phosphorus vacancies and oxygen will be replaced by fluoride ions[40]. In their study, they used a methanolic solution contains 10% water and 5% HF as the etching reagent and dispersed tri-n-octylphosphine oxide TOPO caped InP QDs in n-butanol as solvent[40].

Talapin et al. used HF-photoetching to prepare size selective monodisperse InP QDs of different sizes with quantum yields in the range of 20-40% at room temperature[41]. They claim that the dangling bonds of the surface phosphorus act as a trap for photogenerated holes and etching helps passivation of the surface via interaction of fluorine with the dangling bonds[41].

Mnoyan et al. used fluoric and sulfuric acids and UV irradiation to prepare electrostatically stabilized, with no alkyl ligands on the surface InP QDs with 16% quantum yield.[42] They showed that for selectively etching of nonradiative sites of InP QDs, fluoric acid needs to be in the reaction mixture. They also showed that ligand exchange could lead to higher band edge emission of QDs and different sized of NCs can be obtained through etching.[42]

In this chapter we will address/answer following questions:

I. Is it possible to use metal ions for surface ligand exchange based on hard and soft ion/ligand classification?
II. Does the ligand exchange cause surface passivation and give luminescent QDs?

5-2 Result and discussion

5-2-1 Etching and size of the NCs

Due to the nonlinear relationship between the diameter of NCs and their volume the etching of NCs intrinsically can causes size distribution broadening. The surfaces of particles of different

sizes have different energies[43–45] and consequently, can undergo etching with different rates. A simple theoretical study on spherical nanoparticles shows that as in etching ions will be removed from the surface of particles and because the smaller particles have a smaller surface, which means that in the case of removing one layer of ions from a large particle, more layers will be removed from small particles. For simplifying we assumed that etching happens with the same rate on NCs regardless of their size. This means that first, etching causes size distribution broadening, and second, as etching affects the smaller particles more, an asymmetrical size-distribution diagram will be obtained from etching of samples with asymmetrical size-distribution diagram (Figure 5-1).

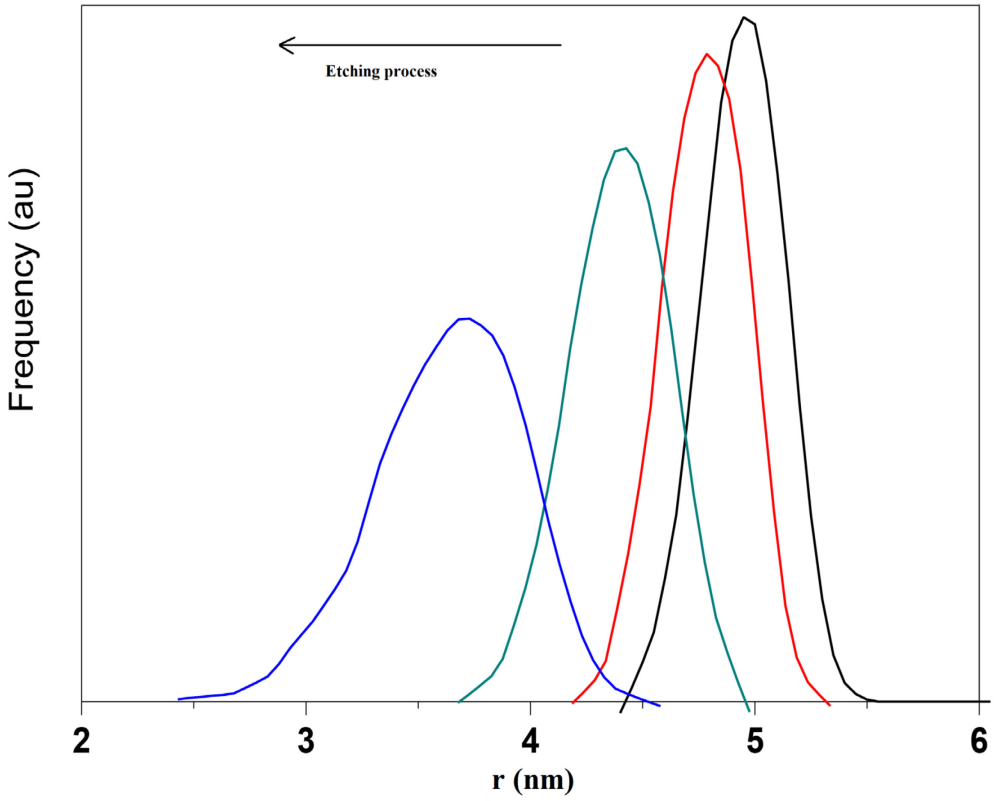

Figure 5-1 Theoretical calculation on size distribution change of spherical NCs via an etching process.

As the band gap and absorption spectra of QDs are size dependent, here UV-Vis absorption spectra of NCs are used for the study of the etching of NCs. Figure 5-2 shows how the absorption of NCs change by their size. The relationship between the size of both CdSe and InP NCs and their absorption is non-linear.[39,46]

It means that for two sample of NCs with different sizes but same size distribution _for instance one sample 3 nm ±.3 and one 5nm ±0.3) absorption feature and emission of the larger InP NCs sample will be narrower than of those of smaller one.

In comparison with CdSe, in the case of InP NCs, size distribution broadening will cause more broadening in absorption feature and emission of NCs. In another word, for two samples of InP and CdSe NCs to have the same emission spectra, the size distribution of InP NCs needs to be much narrower than of CdSe. This intrinsic deference made InP NCs synthesis more challenging because the resulted NCs need to have more monodispersity to give narrow emission spectra.

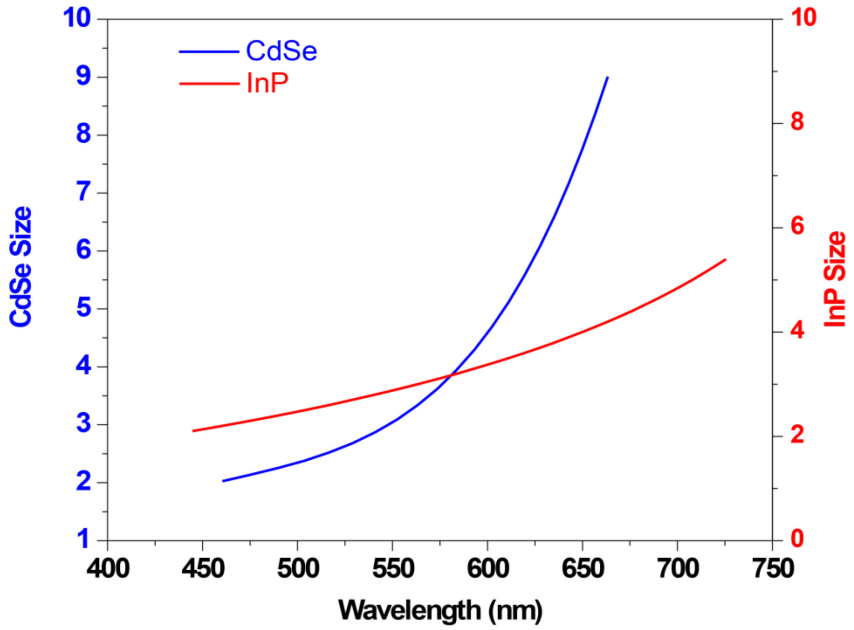

Figure 5-2 Size-dependent absorption of CdSe and InP NCs.

With this, it is necessary to start etching with NCs with very narrow size distribution. For this, InP NCs with narrow size distribution were prepared by the slow heating process and to have more; we performed size selection precipitation as well. Figure 5-3 shows the absorbance spectra of the initially synthesized NCs. As it can be seen, the size distribution of NCs seems relatively narrow; however our size selection separation shows that particles with very different sizes had been formed in the synthesis.

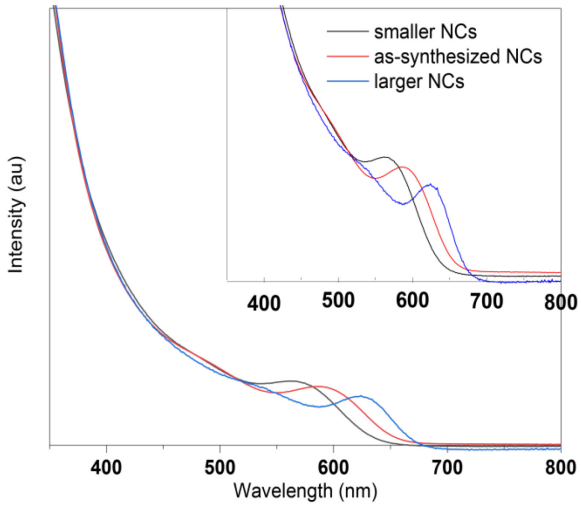

Figure 5-3 Absorption spectrum of as-synthesized InP NCs and larger and smaller obtained after size selected precipitation.

This difference in absorption is very large regarding etching study. It should be noted that the reproducibility of the etching process is dependent on the size distribution of the sample. In the synthesis, NCs with different sizes will be obtained and from synthesis to synthesis, a different combination of NCs of different sizes will be formed. In the other word, although the UV-Vis of different synthesis might have exitonic peak at the same wavelength, the size distribution of NCs might be different or the abundance of different sizes NCs can be different. These differences

cause using the same amount of the etching reagent for etching samples obtained from different synthesis gives different results.

To have an idea about the minimum and maximum amount of $InCl_3$ needed for etching a calibration curve of the amount of $InCl_3$ VS InP were prepared. To do a systematic etching, based on our calibration curve, we set six different amount of etching reagents and to check the reproducibility we placed three reactions for each amount. Figure 5-4 shows the UV-Vis of NCs. As it can be seen, more amount of $InCl_3$ cause more etching. The UV-Vis spectra of etched NCs are recorded in DMSO, and the scattering spectra of NCs indicates their low solubility. We found that etched NCs are insoluble in $CHCl_3$ and tend to disperse in polar solvents; however, more etched NCs have higher solubility in DMSO than lees etched ones. The graph of 1st exitonic peak VS amount of $InCl_3$ shows that there is not a linear relationship between change in absorption feature and the amount of etchant. There can be several explanations for it. As explained, the etching affect the size of NCs and (figure 5-2) there isn't linear relationship between size of NCs and 1st exitonic peak and second, etching happen in term of volume and smaller NCs have much less volume, and less amount of etching is needed for their etching

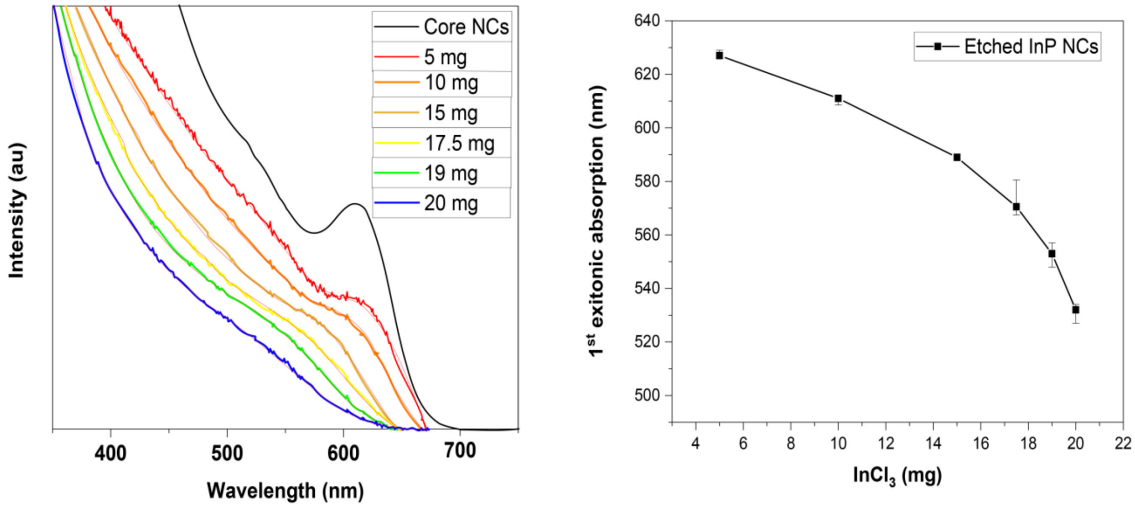

Figure 5-4 a) Absorption spectra of the etched NCs b) scatter plot of 1st exitonic absorption of etched NCs with different amount of $InCl_3$. More $InCl_3$ causes more shift of the 1st exitonic absorption of the etched NCs to higher frequencies.

To make the scatter plot, the 1st exitonic peak of each spectra was determined using the second derivative of each graph. Scatter plot also shows that for smaller NCs less amount of etching reagent is needed. It also shows that etching of NCs has very good reproducibility, especially for larger NCs. It should be noticed that high level of etching results in small NCs which are very susceptible to the etchant and very small change in the amount of etching reagent affect the result significantly _for very last two cases, the difference in the amount of the etchant is 1 mg. With that, the amount of the etchant needs to be measured very accurately and the small error bars for highly etched samples can be because of the uncertainty in measuring $InCl_3$.

Presence of fluoride-containing salts in etching reaction cause NCs to have emission. Figure 5-5 shows the emission of NCs and scatter plot of FWHM of emission spectra of NCs. As it can be seen, more etching leads to bigger FWHM due to more size distribution broadening. Although we used size selected precipitation technique to have initial NCs with narrower size distribution, it should be noted that the samples are not monodisperse and as etching have more effect on smaller NCs, it causes size distribution broadening, especially for highly etched samples.

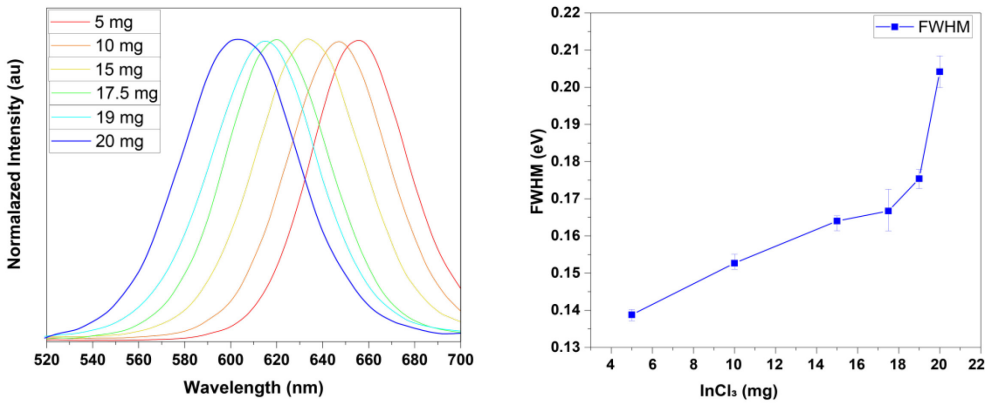

Figure 5-5 a) Emission spectrum of etched NCs b) scatter plot of FWHM of the emission of the etched NCs. More $InCl_3$ causes more shift of the emission spectra to higher energies and also broder emission spectra.

We observed that etched NCs have no solubility in non-polar solvents and precipitate out of etching mixture and as it can be seen from UV-Vis spectra, they low solubility in polar solvents. Figure 5-6a shows UV-Vis absorption spectra of a set of NCs before and after etching TEM image of a sample before and after etching. The NCs size has shifted from 4.37 nm to 2.07.

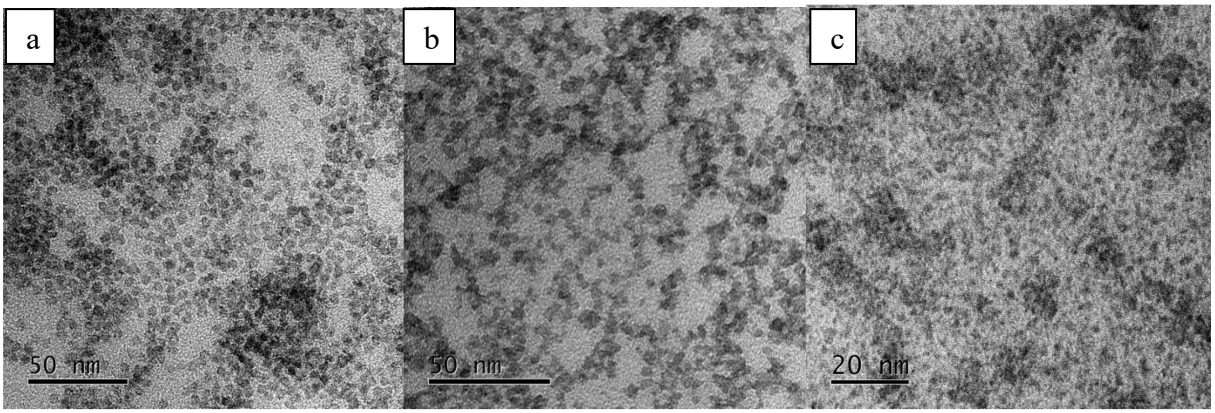

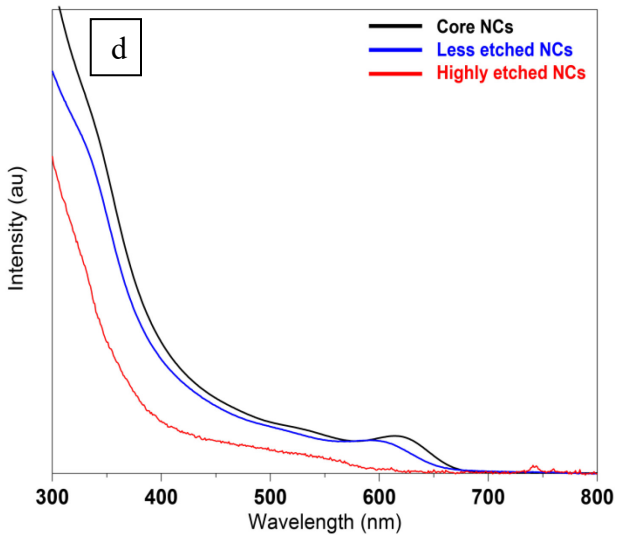

Figure 5-6 a) TEM images of initial NCs, b and c) etched NCs with different amount of $InCl_3$ and d) UV-Visible absorption of the NCs.

The crystalline structure of NCs studied before and after etching using XRD analysis and as shown in Figure 5-7 The peaks are broader after etching due to the decrease in the size of the NCs.

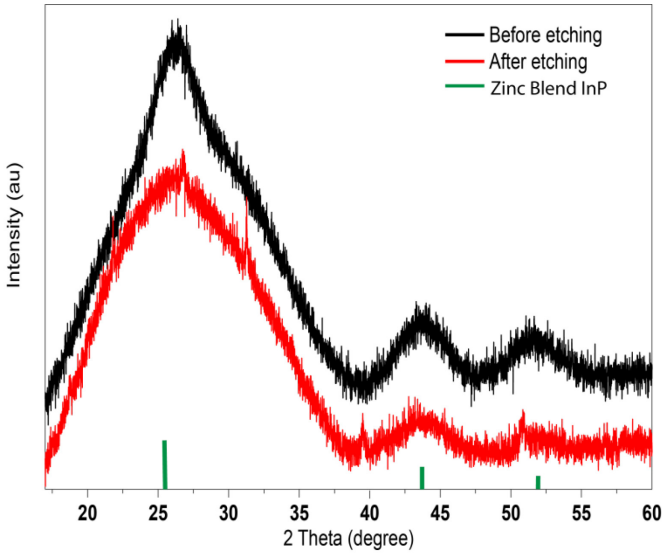

Figure 5-7 XRD pattern of InP NCs before and after etching.

The etching process studied using other metal salts and Bu_4NBF_4. Figure 5-8 shows the UV-Vis absorption spectra of the etched NCs using $MnCl_2$ and $CdCl_2$. It was observed that the absorption spectra of NCs shifted to higher wavelengths which indicates formation os smaller NCs but the no emission was observed in this cases.

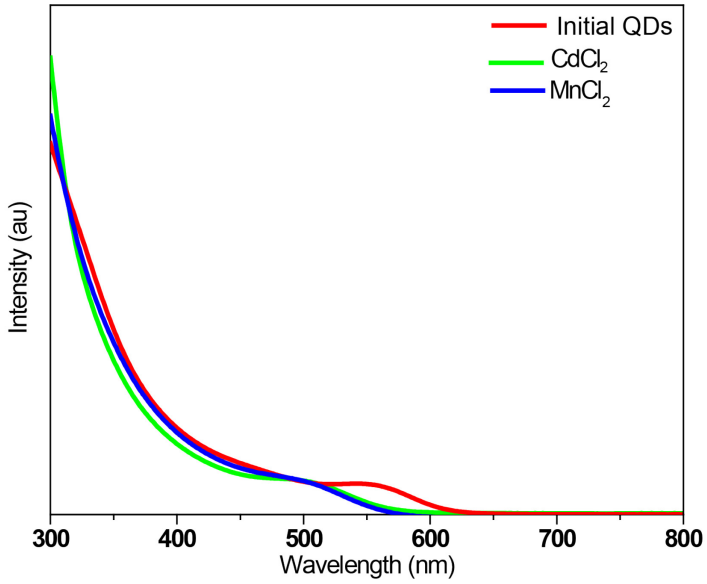

Figure 5-8 UV-Visible absorption of the InP QDs etched using $CdCl_2$ and $MnCl_2$.

In case of using $ZnCl_2$ emissive NCs obtained. It also observed that Bu_4NBF_4 also can be used as the source of fluoride ion and results in emissive NCs.

5-2-2 ^{1}H, ^{19}F, and ^{31}P NMR studies

The mechanism of the etching process is studied using NMR analysis. We found that $InCl_3$ has a very low solubility in $CDCl_3$ compared to $CHCl_3$ and because of that we did our reactions for NMR studies in mixtures of $CHCl_3$ and $CDCl_3$. Figure 5-9 shows the ^{1}H-NMR spectra of the reaction of $InCl_3$ and Bu_4NPF_6 with InP NCs in 2:1 mixture of $CDCl_3$ and $CHCl_3$. As is shown in

figure 5-9, all main peaks are assigned to organic chemicals that used in the preparation of initial InP NCs or for etching step.

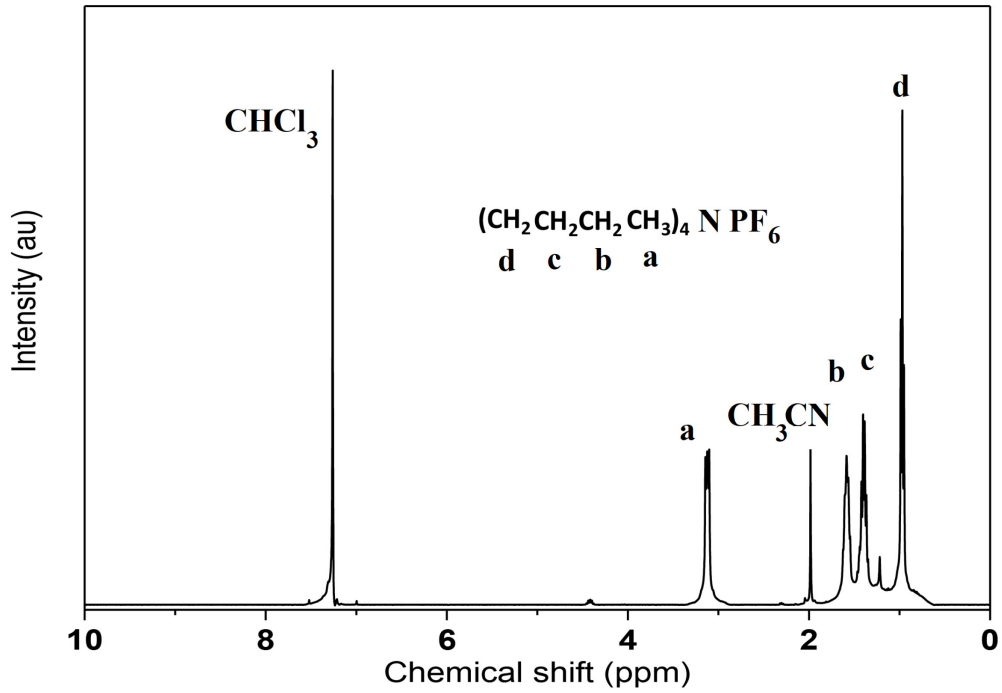

Figure 5-9 ^{1}H NMR spectrum of the etching solution of $InCl_3$ and Bu_4NPF_6 with InP NCs in 2:1 mixture of $CDCl_3$ and $CHCl_3$. All peaks correspond to compounds used I the preparation of InP QDs or etching process**.**

The ^{19}F-NMR gives more information about species that are formed in the reaction. As shown in figure 5-10, besides doublet peaks related to PF_6^- at -71 ppm and -73.5 ppm, [47] new peaks are observed at -83.3 ppm and -85.9 ppm which are related to $PO_2F_2^-$. Also, a peak at -152.16 ppm is observed which corresponds to BF_4^-.[48, 49]

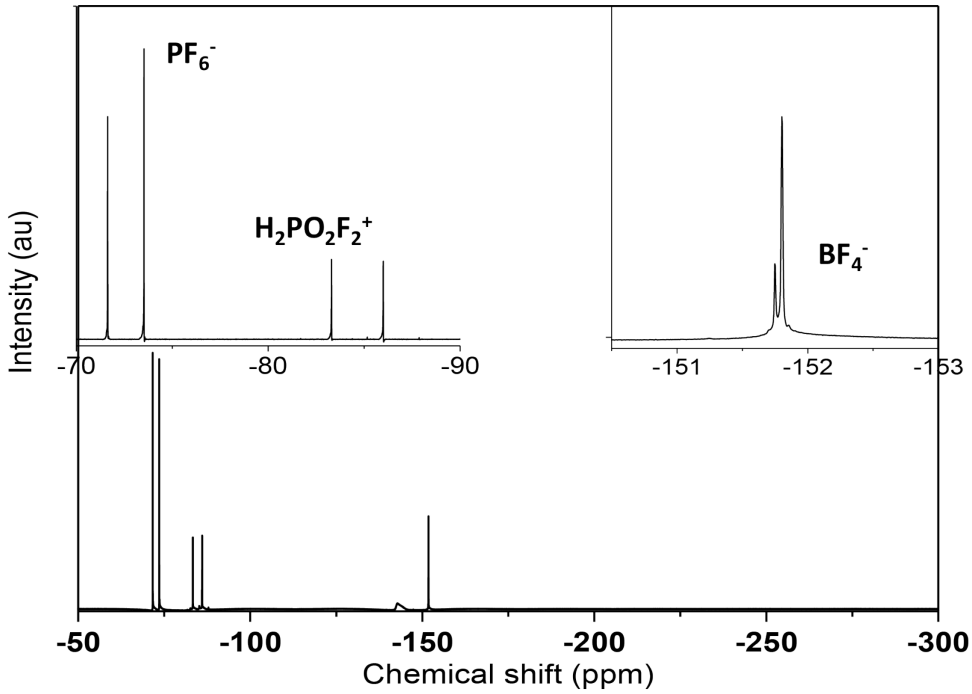

Figure 5-10 ^{19}F NMR spectrum of the etching solution of InP NCs using $InCl_3$ and Bu_4NPF_6 in $CDCl_3$ and $CHCl_3$ (2:1). The peaks at -71.6 and -73.5 ppm correspond to doublet peaks of PF_6^- and peaks at -83.3 and -85.9 ppm correspond to $H_2PO_2F_2$ in (A). The peaks around -151.8 ppm in (B) correspond to BF4−, likely formed from etching of glass vial (Borosilicate).

To find the origin of BF_4^-, $^{19}FNMR$ of the reaction of $InCl_3$ with Bu_4NPF_6 in a mixture of $CHCl_3$ and $CDCl_3$ was studied. As shown in Figure 5-11, the peak related to BF_4^- appeared at -151.9 ppm. This peak is seen after adding InP NCs to the reaction mixture. This shows that BF_4^- is not absorbed on the surface of NCs and stay in the solution.

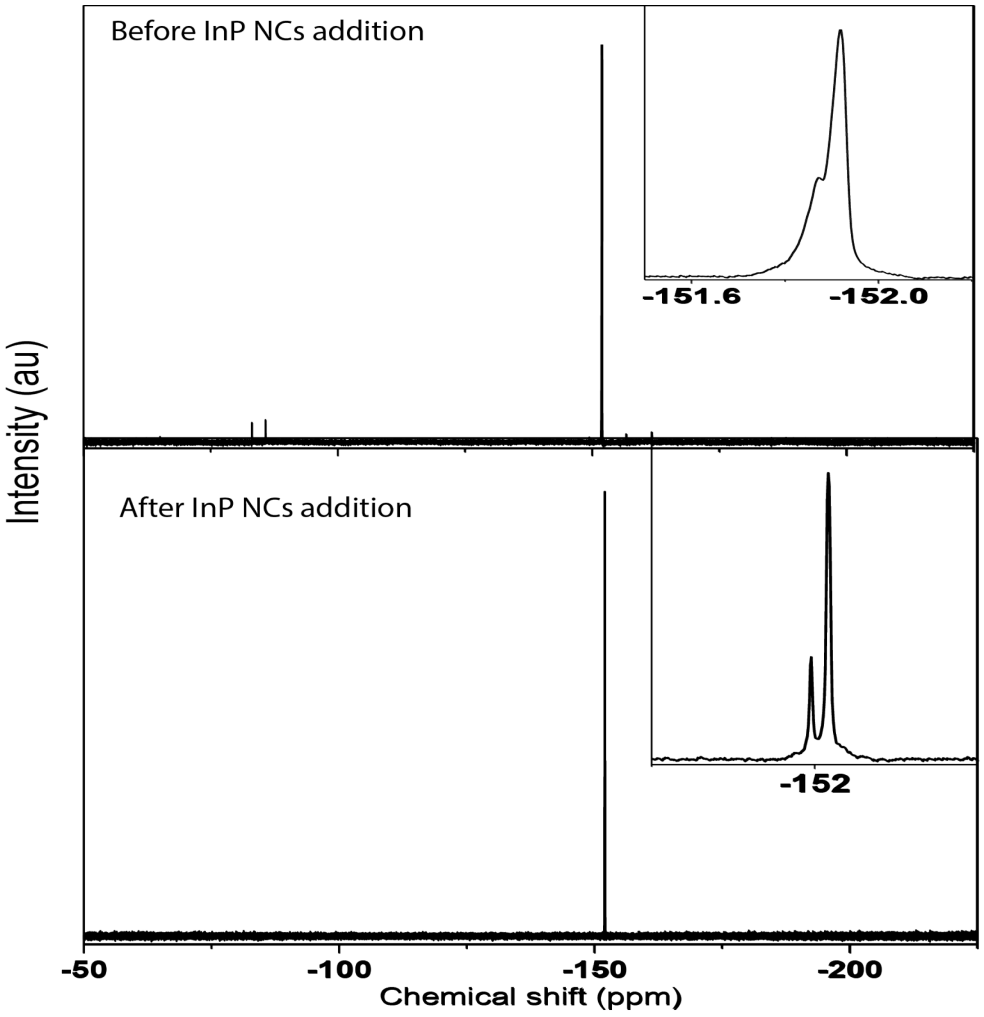

Figure 5-11 ^{19}F NMR spectrum of the etching solution containing $InCl_3$ and Bu_4NPF_6 in $CDCl_3$ and $CHCl_3$ (2:1) before and after adding InP QDs. The peaks around -152 ppm in corresponds to $BF4^-$.

Figure 5-12 shows hydrogen coupled and hydrogen decoupled ^{31}PNMR studies of the sample. The triplet peak centered at -19 ppm is related to $H_2PO_2F_2^+$ and heptuplet peak of PF_6^- is centered at -143 ppm[50] and the peak at -237.2 ppm in H-decoupled spectra indicates the formation of PH_3 during the etching process. This PH_3 peak split to 4 peaks in H-coupled spectra.

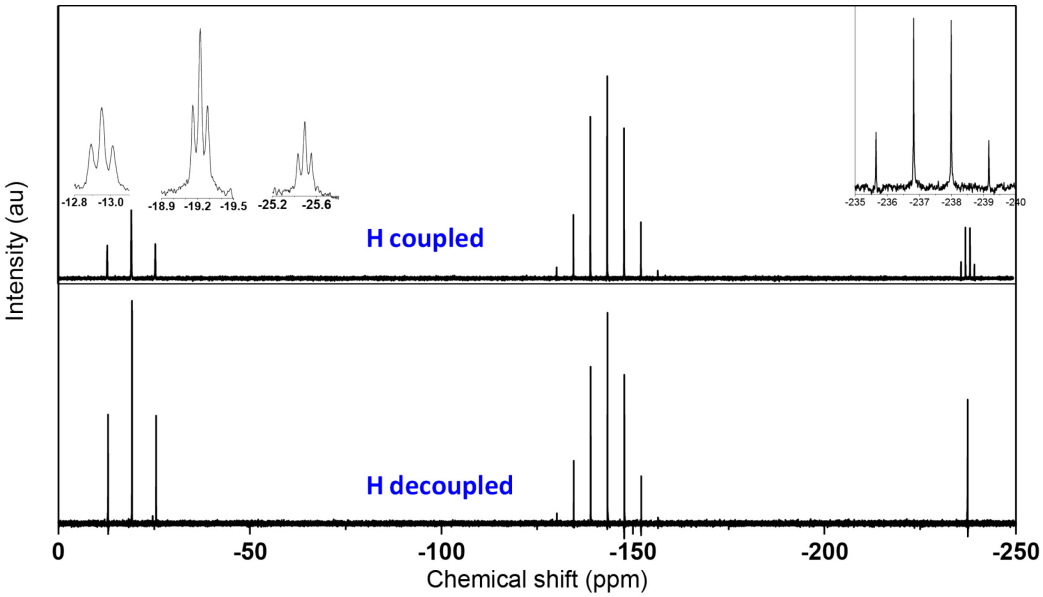

Figure 5-12 proton-coupled and decoupled ^{31}P NMR spectra of the etching solution of InP QDs containing $InCl_3$ and Bu_4NPF_6 in $CDCl_3$ and $CHCl_3$ (2:1). The triplet peak centered around -19.2 ppm corresponds to $H_2PO_2F_2^{+\cdot}$ heptuplet peak of PF_6^- centered at about -143 ppm and peak at about -237 ppm of PH_3 which split to four peaks when coupled with hydrogen.

To find if the $H_2PO_2F_2$ and PH_3 are originated from InP NCs or PF_6^-, the reaction of $InCl_3$ and InP NCs is studied. Figure 5-13 shows the ^{31}P NMR spectra of the reaction mixture and the peak at -237 ppm which split when measuring hydrogen coupled spectra indicates the formation of PH_3. This observation, indicates that PH_3 is originated from InP NCs.

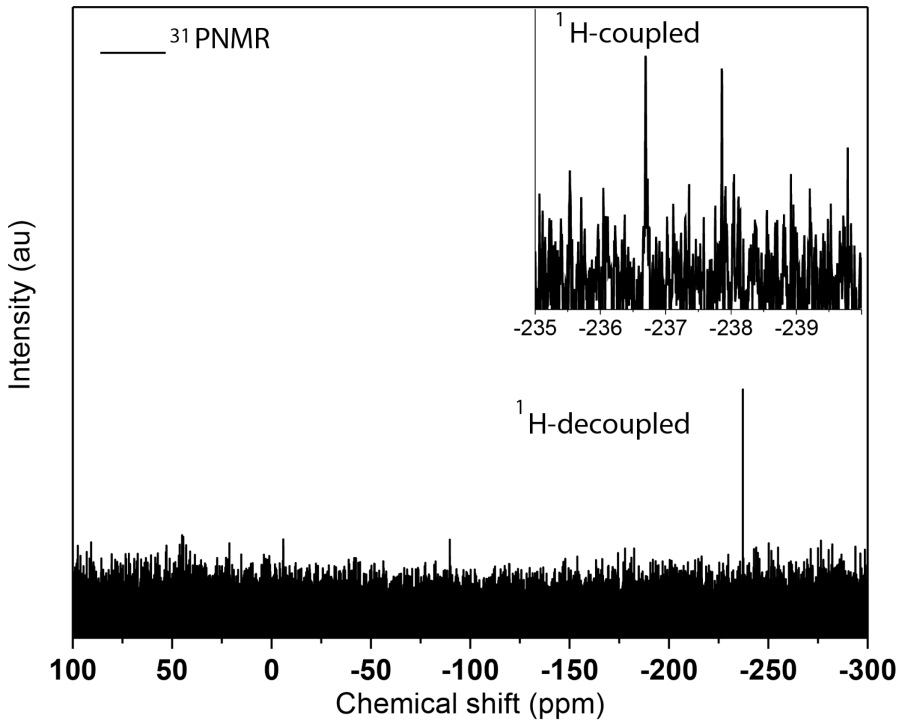

Figure 5-13 proton-coupled and decoupled ^{31}P NMR spectra of the etching solution of InP QDs containing $InCl_3$ in $CDCl_3$ and $CHCl_3$ (2:1). The peak at about -237 ppm corresponds to PH_3 which split to four peaks when coupled with hydrogen.

In another study, ^{19}F NMR of reaction of $InCl_3$ and Bu_4NBF_4 with InP NCs was addressed. As no peak related to $H_2PO_2F_2$ was observed (Figure 5-14), the origin of this compound should be PF_6^- ion. In ^{31}P NMR spectra of the sample, peak of PH_3 was observed at -237 ppm which split in case of recording ^1H-coupled spectra (Figure 5-15).

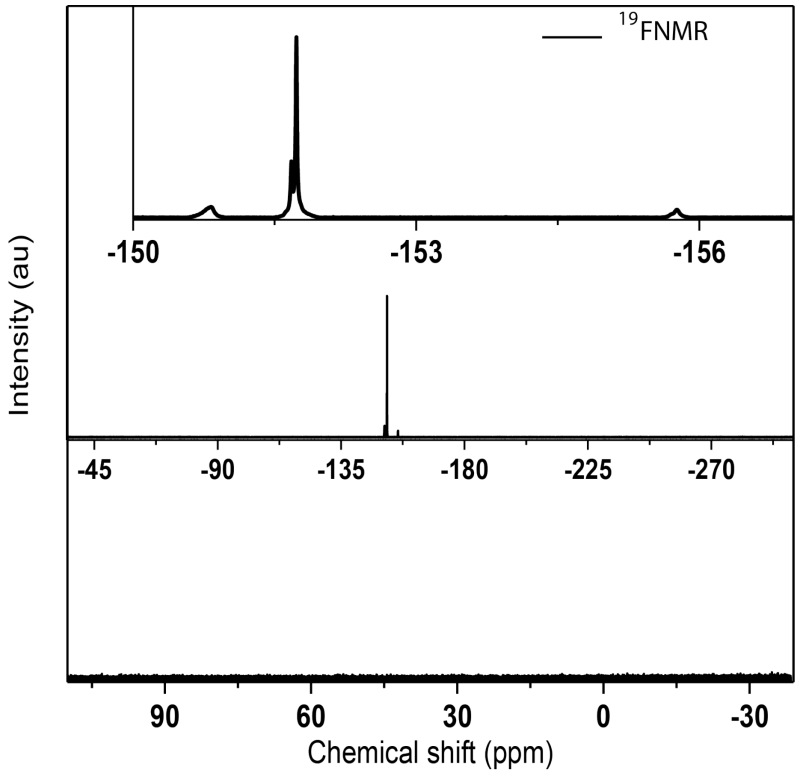

Figure 5-14 ^{19}F NMR spectrum of the etching solution containing InP QDs, $InCl_3$ and Bu_4NBF_4 in $CDCl_3$ and $CHCl_3$ (2:1). No peak related to $H_2PO_2F_2$ observed. The peaks around -152 ppm in corresponds to $BF4^-$.

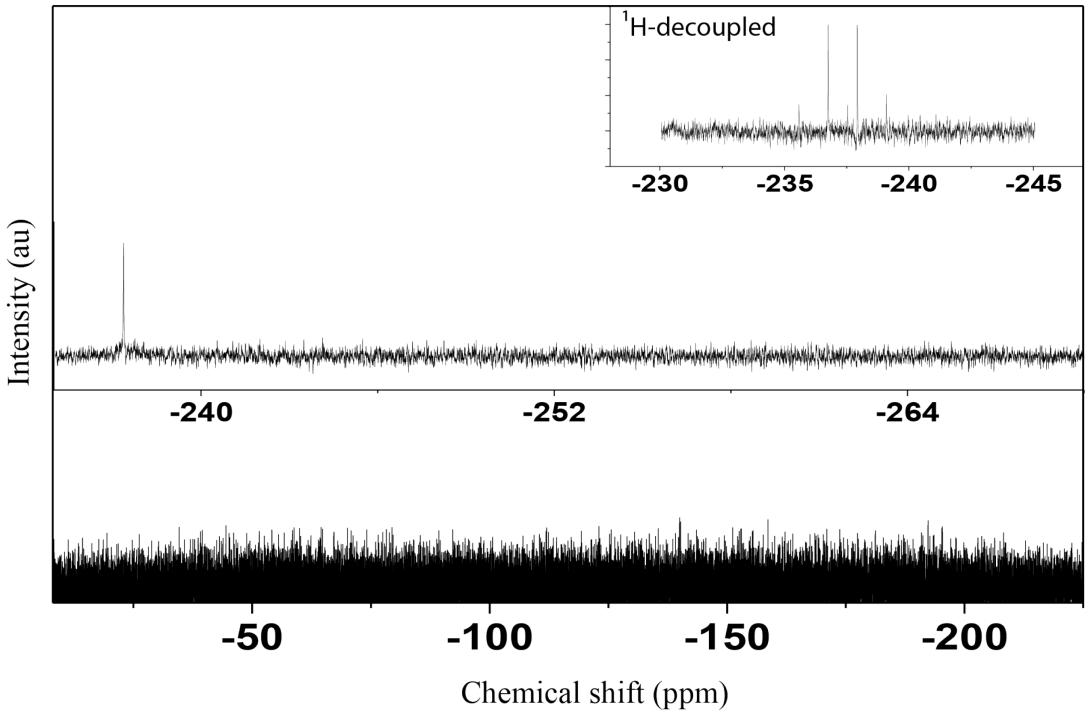

Figure 5-15 ^{31}P NMR spectrum of the etching solution containing $InCl_3$, Bu_4NBF_4 and InP in $CDCl_3$ and $CHCl_3$ (2:1). The peak corresponds to PH_3 which split to four peaks when coupled with hydrogen is appear at about -237 ppm.

Our study showed that no reaction happens using just $CDCl_3$ as solvent and addition of $CHCl_3$ is necessary for the etching process to happen. The reason for this can be the presence of EtOH as stabilizer and trace amount of water as an impurity in $CHCl_3$. As can be seen in figure 5-16, in the absence of MeOH no peak related to the formation of PH_3 was observed in ^{31}P NMR study shows that but, after addition of MeOH, the peak related to PH_3 emerged.

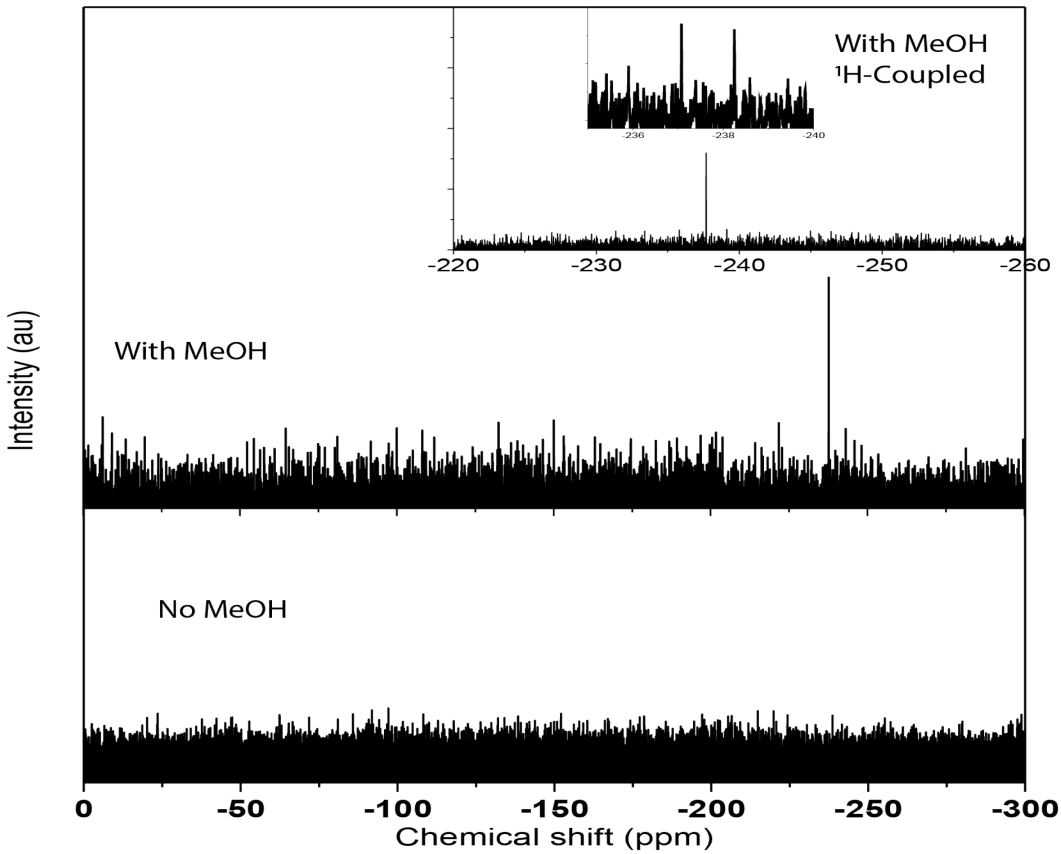

Figure 5-16 ^{31}P NMR spectrum of the etching solution containing $InCl_3$ and Bu_4NPF_6 in $CDCl_3$ with and without MeOH. Ds. I case of pure $CDCl_3$ no peak related to the PH_3 observed but, after adding MeOH, PH_3 peak appeared at around -237.

5-2-3 Zeta potential measurements

Zeta potential measurement carried out using a ZetaPALS zeta potential analyzer, Brookhaven. NCs are separated using centrifuge and dispersed in DMSO. Figure 5-17 a and b show the measured zeta potential for etched NCs in the presence of Bu_4NPF_6 containing salt and without using F^- containing salt respectively. The zeta potential is positive no matter if the PF_6^- is used in the etching process or not. It should be noticed that as DMSO is not an option in the used instrument, there can be inaccuracy with the magnitude of the measured zeta potential value. The

positive values indicate cationic surface due to the presence of cations on the surface. The NMR data indicate the presence of $H_2PO_2F_2^+$ ion in the reaction mixture, but as etched NCs in the absence of F^- containing salts have positive charge, the surface charge can be resulted from surface indium ions generated from formation of P-H bonds (Figure 5-18)

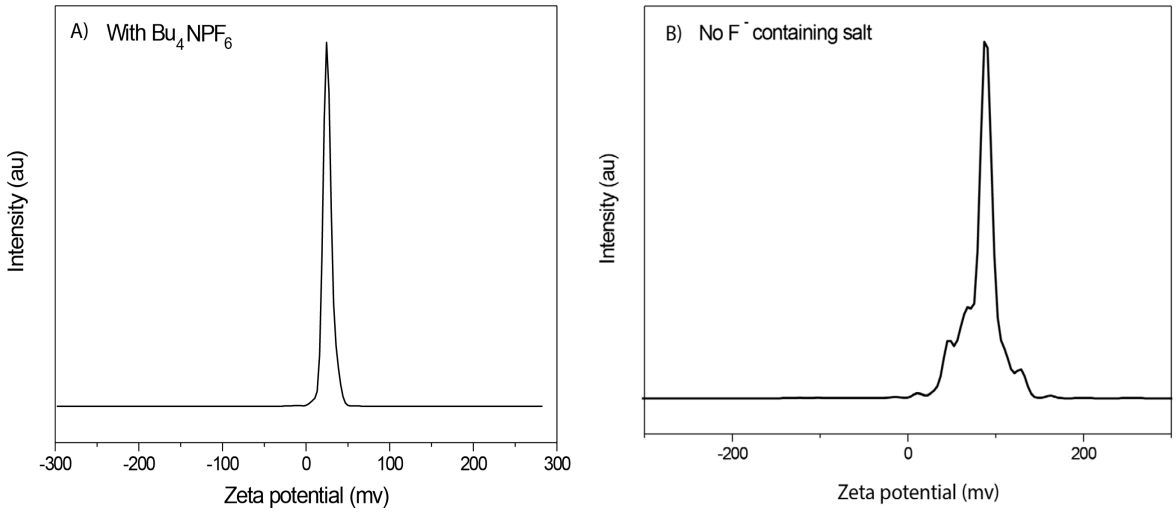

Figure 5-17 Zeta potential measurements of the NCs from etching of InP QDs using $InCl_3$ in the presence of Bu_4NPF_6 (A) and without Bu_4NPF_6 (B). Positive charge indicates the presence of cations on the surface of the QDs.

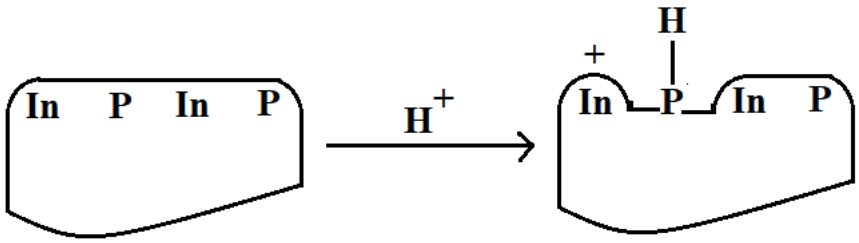

Figure 5-18 Possible mechanisms of positive charge formation on the QDs surface

5-4 Mechanism

Considering formation of PH_3 in the reaction mixture, the etching is due to the presence of acid in the reaction mixture. It is known that reaction of metal ions with water can form acid. [51-54] The source of acid can be reaction of $InCl_3$ with trace water of the $CHCl_3$. On the other hand, formation of $BF4^-$ indicates presence of HF in the reaction mixture. Decomposition of PF_6^- can generate HF and fluoro phosphates such as $PO_2F_2^-$.[55-58] The reactions regarding etching are shown below.

$In^{3+} + 6\ H_2O \rightarrow In(H_2O)_5OH + H^+$

$2H_2O + PF_6^- \rightarrow PO_2F_2^- + 4HF$

$3H^+ + InP \rightarrow In^{3+} + PH_3$

5-3 Materials and Methods

All the chemicals used are commercially available and were used without further purification; methanol (MeOH) and Tetrabutylammonium hexafluorophosphate (Bu_4NPF_6, 99.8%), from Acros, palmitic acid (PA, ≥99%), octadecane (ODE 90%), indium chloride ($InCl_3$, 99.9%), toluene, dimethyl sulfoxide (DMSO ≥99.9%) and chloroform ($CHCl_3$ 99.8%) from Sigma-Aldrich; tris(trimethylsilyl)phosphine ($P(TMS)_3$), 98% (10% in hexane), tri-n-octylphosphine (TOP) (97%), and indium acetate ($In(OAc)_3$, 99.99% trace metals basis) from Strem.

5-3-1 Synthesis and etching

The NCs were synthesized as it described Ramasamy et al.[39] First, 10 ml stock solution of $In(PA)_3$ from degassing Indium acetate (1 mmol) and palmitic acid (3 mmol) in 10 mL of ODE for 2h. Separately, in a 250 ml three-neck flask, Indium acetate (0.15 mmol) and palmitic acid (0.45 mmol) were mixed with 10 mL of ODE and degassed at 110 for 2 h. Then, after refilling

with N_2, the flask was cooled to RT. Then, a solution containing 0.1 mmol of $(TMS)_3P$ and 1 mL of TOP was quickly injected into the flask. And the mixture was heated to 305 °C (15 °C/min) and kept at that temperature for 2 min. Then the heating mantle was removed and the reaction was cooled down to 210 °C. At this point 1.5 mL of previously prepared $In(PA)_3$ stock solution was injected to the reaction mixture and kept at 210 °C for 30 min and then cooled to RT. Then, a solution containing 0.1 mmol of $(TMS)_3P$ and 1 mL of TOP injected into it and heated up again in the same way as described before. The growth process was repeated for four times.

After synthesis, the QDs were washed using toluene as solvent and acetone as a precipitating agent. During the washing NCs, were separated based on their sizes using less amount of acetone and lower centrifuge rpm. After washing for 4 times, NCs were dispersed in chloroform and after adding ACN, precipitated out using centrifuge and dispersed and stored in chloroform.

To etch NCs, under an inert atmosphere, 0.0050-0.0200 mg of $InCl_3$ was placed in glass vial 3 ml of chloroform was added to it and then 0.5 ml of InP NCs stock solution containing Bu_4NPF_6 (50 mM) added to it and stirred overnight. Then the particles centrifuged out and stored in $CHCl_3$ or DMSO.

5-4 Summary

In summary, a new method for room temperature, post-synthetic etching of InP NCs is studied. The combination of $InCl_3$ and Bu_4NPF_6 used for ligand stripping and etching of NCs. The size of final NCs can be tuned by controlling the amount of $InCl_3$. The study showed that the presence of fluoride-containing salt is necessary for surface passivation and band edge emission of the NCs. Our expectation was surface ligand exchange but we found that due to the formation of

acids in the reaction mixture, an etching process causes change in size and HF causes surface passivation and obtaining luminescent QDs with different sizes.

5-5 Conclusion

In this study, we achieved our goal which was obtaining luminescent QDs, but it happens through a different mechanism. Our goal was ligand exchange, however, what we observed is acid etching of QDs. The mixture of InCl3 and Bu4NPF6 in CHCl3 forms HF and HCl acids and these acids etch QDs and yield luminescent QDs. By controlling the reactants concentrations, the amount of formed acids can be controlled and the etching process can be tunned.

5-6 Reference

(1) Vaneski, A.; Schneider, J.; Susha, A. S.; Rogach, A. L. Aqueous Synthesis of CdS and CdSe/CdS Tetrapods for Photocatalytic Hydrogen Generation. *APL Mater.* **2014**, *2* (1), 012104.

(2) Amirav, L.; Alivisatos, A. P. Photocatalytic Hydrogen Production with Tunable Nanorod Heterostructures. *J. Phys. Chem. Lett.* **2010**, *1* (7), 1051–1054.

(3) Kubacka, A.; Fernández-García, M.; Colón, G. Advanced Nanoarchitectures for Solar Photocatalytic Applications. *Chem. Rev.* **2012**, *112* (3), 1555–1614.

(4) Zhang, X.; Qin, J.; Xue, Y.; Yu, P.; Zhang, B.; Wang, L.; Liu, R. Effect of Aspect Ratio and Surface Defects on the Photocatalytic Activity of ZnO Nanorods. *Sci. Rep.* **2014**, *4*.

(5) Yang, Z.; Voznyy, O.; Liu, M.; Yuan, M.; Ip, A. H.; Ahmed, O. S.; Levina, L.; Kinge, S.; Hoogland, S.; Sargent, E. H. All-Quantum-Dot Infrared Light-Emitting Diodes. *ACS Nano* **2015**, *9* (12), 12327–12333.

(6) Son, D. I.; Kwon, B. W.; Park, D. H.; Seo, W.-S.; Yi, Y.; Angadi, B.; Lee, C.-L.; Choi, W. K. Emissive ZnO-Graphene Quantum Dots for White-Light-Emitting Diodes. *Nat. Nanotechnol.* **2012**, *7* (7), 465–471.

(7) Jiang, Y.; Cho, S.-Y.; Shim, M. Light-Emitting Diodes of Colloidal Quantum Dots and Nanorod Heterostructures for Future Emissive Displays. *J. Mater. Chem. C* **2018**, *6* (11), 2618–2634.

(8) Owen, J.; Brus, L. Chemical Synthesis and Luminescence Applications of Colloidal Semiconductor Quantum Dots. *J. Am. Chem. Soc.* **2017**, *139* (32), 10939–10943.

(9) Kim, T.-H.; Cho, K.-S.; Lee, E. K.; Lee, S. J.; Chae, J.; Kim, J. W.; Kim, D. H.; Kwon, J.-Y.; Amaratunga, G.; Lee, S. Y.; et al. Full-Colour Quantum Dot Displays Fabricated by Transfer Printing. *Nat. Photonics* **2011**, *5* (3), 176.

(10) Lan, X.; Voznyy, O.; García de Arquer, F. P.; Liu, M.; Xu, J.; Proppe, A. H.; Walters, G.; Fan, F.; Tan, H.; Liu, M.; et al. 10.6% Certified Colloidal Quantum Dot Solar Cells via Solvent-Polarity-Engineered Halide Passivation. *Nano Lett.* **2016**, *16* (7), 4630–4634.

(11) Tian, J.; Lv, L.; Fei, C.; Wang, Y.; Liu, X.; Cao, G. A Highly Efficient (>6%) $Cd_{1-x}Mn_xSe$ Quantum Dot Sensitized Solar Cell. *J. Mater. Chem. A* **2014**, *2* (46), 19653–19659.

(12) Ning, Z.; Voznyy, O.; Pan, J.; Hoogland, S.; Adinolfi, V.; Xu, J.; Li, M.; Kirmani, A. R.; Sun, J.-P.; Minor, J.; et al. Air-Stable n-Type Colloidal Quantum Dot Solids. *Nat. Mater.* **2014**, *13* (8), 822–828.

(13) Wang, R.; Shang, Y.; Kanjanaboos, P.; Zhou, W.; Ning, Z.; Sargent, E. H. Colloidal Quantum Dot Ligand Engineering for High Performance Solar Cells. *Energy Environ. Sci.* **2016**, *9* (4), 1130–1143.

(14) Yuan, M.; Liu, M.; Sargent, E. H. Colloidal Quantum Dot Solids for Solution-Processed Solar Cells. *Nat. Energy* **2016**, *1* (3), 16016.

(15) Giansante, C. Surface Chemistry Control of Colloidal Quantum Dot Band Gap. *J. Phys. Chem. C* **2018**, *122* (31), 18110–18116.

(16) Pichaandi, J.; Abel, K. A.; Johnson, N. J. J.; van Veggel, F. C. J. M. Long-Term Colloidal Stability and Photoluminescence Retention of Lead-Based Quantum Dots in Saline Buffers and Biological Media through Surface Modification. *Chem. Mater.* **2013**, *25* (10), 2035–2044.

(17) Hou, X.; Mankoci, S.; Walters, N.; Gao, H.; Zhang, R.; Li, S.; Qin, H.; Ren, Z.; Doll, G. L.; Cong, H.; et al. Hierarchical Structures on Nickel-Titanium Fabricated by Ultrasonic Nanocrystal Surface Modification. *Mater. Sci. Eng. C* **2018**, *93*, 12–20.

(18) Gutiérrez Sánchez, C.; Su, Q.; Schönherr, H.; Grininger, M.; Nöll, G. Multi-Ligand-Binding Flavoprotein Dodecin as a Key Element for Reversible Surface Modification in Nano-Biotechnology. *ACS Nano* **2015**, *9* (4), 3491–3500.

(19) Marasini, R.; Pitchaimani, A.; Nguyen, T. D. T.; Comer, J.; Aryal, S. The Influence of Polyethylene Glycol Passivation on the Surface Plasmon Resonance Induced Photothermal Properties of Gold Nanorods. *Nanoscale* **2018**, *10* (28), 13684–13693.

(20) Takahata, R.; Yamazoe, S.; Koyasu, K.; Imura, K.; Tsukuda, T. Gold Ultrathin Nanorods with Controlled Aspect Ratios and Surface Modifications: Formation Mechanism and Localized Surface Plasmon Resonance. *J. Am. Chem. Soc.* **2018**, *140* (21), 6640–6647.

(21) Mazloomi-Rezvani, M.; Salami-Kalajahi, M.; Roghani-Mamaqani, H.; Pirayesh, A. Effect of Surface Modification with Various Thiol Compounds on Colloidal Stability of Gold Nanoparticles. *Appl. Organomet. Chem.* **2018**, *32* (2), e4079.

(22) Tulsani, S. R.; Rath, A. K. Photo-Induced Surface Modification to Improve the Performance of Lead Sulfide Quantum Dot Solar Cell. *J. Colloid Interface Sci.* **2018**, *522*, 120–125.

(23) Mnoyan, A. N.; Kirakosyan, A. G.; Kim, H.; Jang, H. S.; Jeon, D. Y. Electrostatic Stabilized InP Colloidal Quantum Dots with High Photoluminescence Efficiency. *Langmuir* **2015**, *31* (25), 7117–7121.

(24) Jeong, Y. J.; Yun, D.-J.; Noh, S. H.; Park, C. E.; Jang, J. Surface Modification of CdSe Quantum-Dot Floating Gates for Advancing Light-Erasable Organic Field-Effect Transistor Memories. *ACS Nano* **2018**, *12* (8), 7701–7709.

(25) Kroupa, D. M.; Vörös, M.; Brawand, N. P.; McNichols, B. W.; Miller, E. M.; Gu, J.; Nozik, A. J.; Sellinger, A.; Galli, G.; Beard, M. C. Tuning Colloidal Quantum Dot Band Edge Positions through Solution-Phase Surface Chemistry Modification. *Nat. Commun.* **2017**, *8*, 15257.

(26) Lee, S. K.; McLaurin, E. J. Recent Advances in Colloidal Indium Phosphide Quantum Dot Production. *Curr. Opin. Green Sustain. Chem.* **2018**, *12*, 76–82.

(27) Bonilla, C. A. M.; Kouznetsov, V. V. "Green" Quantum Dots: Basics, Green Synthesis, and Nanotechnological Applications. **2016**.

(28) Liu, Z.; Kumbhar, A.; Xu, D.; Zhang, J.; Sun, Z.; Fang, J. Coreduction Colloidal Synthesis of III–V Nanocrystals: The Case of InP. *Angew. Chem. Int. Ed.* **2008**, *47* (19), 3540–3542.

(29) Tamang, S.; Lincheneau, C.; Hermans, Y.; Jeong, S.; Reiss, P. Chemistry of InP Nanocrystal Syntheses. *Chem. Mater.* **2016**, *28* (8), 2491–2506.

(30) Tessier, M. D.; Dupont, D.; De Nolf, K.; De Roo, J.; Hens, Z. Economic and Size-Tunable Synthesis of InP/ZnE (E = S, Se) Colloidal Quantum Dots. *Chem. Mater.* **2015**, *27* (13), 4893–4898.

(31) Lovingood, D. D.; Strouse, G. F. Microwave Induced In-Situ Active Ion Etching of Growing InP Nanocrystals. *Nano Lett.* **2008**, *8* (10), 3394–3397.

(32) Siramdas, R.; McLaurin, E. J. InP Nanocrystals with Color-Tunable Luminescence by Microwave-Assisted Ionic-Liquid Etching. *Chem. Mater.* **2017**, *29* (5), 2101–2109.

(33) Ramasamy, P.; Kim, N.; Kang, Y.-S.; Ramirez, O.; Lee, J.-S. Tunable, Bright, and Narrow-Band Luminescence from Colloidal Indium Phosphide Quantum Dots. *Chem. Mater.* **2017**, *29* (16), 6893–6899.

(34) Koh, S.; Eom, T.; Kim, W. D.; Lee, K.; Lee, D.; Lee, Y. K.; Kim, H.; Bae, W. K.; Lee, D. C. Zinc–Phosphorus Complex Working as an Atomic Valve for Colloidal Growth of Monodisperse Indium Phosphide Quantum Dots. *Chem. Mater.* **2017**, *29* (15), 6346–6355.

(35) Zherebetskyy, D.; Scheele, M.; Zhang, Y.; Bronstein, N.; Thompson, C.; Britt, D.; Salmeron, M.; Alivisatos, P.; Wang, L.-W. Hydroxylation of the Surface of PbS Nanocrystals Passivated with Oleic Acid. *Science* **2014**, *344* (6190), 1380–1384.

(36) Gary, D. C.; Terban, M. W.; Billinge, S. J. L.; Cossairt, B. M. Two-Step Nucleation and Growth of InP Quantum Dots via Magic-Sized Cluster Intermediates. *Chem. Mater.* **2015**, *27* (4), 1432–1441.

(37) Xie, L.; Harris, D. K.; Bawendi, M. G.; Jensen, K. F. Effect of Trace Water on the Growth of Indium Phosphide Quantum Dots. *Chem. Mater.* **2015**, *27* (14), 5058–5063.

(38) Baquero, E. A.; Virieux, H.; Swain, R. A.; Gillet, A.; Cros-Gagneux, A.; Coppel, Y.; Chaudret, B.; Nayral, C.; Delpech, F. Synthesis of Oxide-Free InP Quantum Dots: Surface Control and H2-Assisted Growth. *Chem. Mater.* **2017**, *29* (22), 9623–9627.

(39) Kim, K.; Yoo, D.; Choi, H.; Tamang, S.; Ko, J.-H.; Kim, S.; Kim, Y.-H.; Jeong, S. Halide–Amine Co-Passivated Indium Phosphide Colloidal Quantum Dots in Tetrahedral Shape. *Angew. Chem. Int. Ed.* **2016**, *55* (11), 3714–3718.

(40) Mićić, O. I.; Sprague, J.; Lu, Z.; Nozik, A. J. Highly Efficient Band-edge Emission from InP Quantum Dots. *Appl. Phys. Lett.* **1996**, *68* (22), 3150–3152.

(41) Talapin, D. V.; Gaponik, N.; Borchert, H.; Rogach, A. L.; Haase, M.; Weller, H. Etching of Colloidal InP Nanocrystals with Fluorides: Photochemical Nature of the Process Resulting in High Photoluminescence Efficiency. *J. Phys. Chem. B* **2002**, *106* (49), 12659–12663.

(42) Mnoyan, A. N.; Kirakosyan, A. G.; Kim, H.; Jang, H. S.; Jeon, D. Y. Electrostatic Stabilized InP Colloidal Quantum Dots with High Photoluminescence Efficiency. *Langmuir* **2015**, *31* (25), 7117–7121.

(43) and, H. M. L.; Jiang, Q. Size-Dependent Surface Energies of Nanocrystals *J. Phys. Chem. B*, **2004**, 108 (18), 5617–5619.

(44) Liu, D.; Lian, J. S.; Jiang, Q. Surface Energy and Electronic Structures of Ag Quasicrystal Clusters *J. Phys. Chem. C*, **2009**, 113 (4), 1168–1170.

(45) Yao, Y.; Wei, Y.; Chen, S. Size Effect of the Surface Energy Density of Nanoparticles. *Surf. Sci.* **2015**, *636*, 19–24.

(46) Yu, W. W.; Qu, L.; Guo, W.; Peng, X. Experimental Determination of the Extinction Coefficient of CdTe, CdSe, and CdS Nanocrystals. *Chem. Mater.* **2003**, *15* (14), 2854–2860.

(47) K. Glasson, C. R.; V. Meehan, G.; K. Clegg, J.; F. Lindoy, L.; Turner, P.; B. Duriska, M.; Willis, R. A New FeII Quaterpyridyl M 4 L 6 Tetrahedron Exhibiting Selective Anion Binding. *Chem. Commun.* **2008**, *0* (10), 1190–1192.

(48) Beniwal, V.; Shukla, S. K.; Kumar, A. Deviation of Polarity from Linearity in Liquid Mixtures Containing an Ionic Liquid. *Phys. Chem. Chem. Phys.* **2015**, *17* (47), 31613–31617.

(49) Tamanini, E.; Ponnuswamy, N.; Dan Pantoş, G.; M. Sanders, J. K. New Host –Guest Chemistry of Supramolecular Nanotubes. *Faraday Discuss.* **2010**, *145* (0), 205–218.

(50) Caporali, M.; Gonsalvi, L.; Kagirov, R.; Mirabello, V.; Peruzzini, M.; Sinyashin, O.; Stoppioni, P.; Yakhvarov, D. The First Water-Soluble Tetraphosphorus Ruthenium Complex. Synthesis, Characterization and Kinetic Study of Its Hydrolysis. *J. Organomet. Chem.* **2012**, *714*, 67–73.

(51) Hawkes, S. J. All Positive Ions Give Acid Solutions in Water. *J. Chem. Educ.* **1996**, *73* (6), 516.

(52) Jackson, V. E.; Felmy, A. R.; Dixon, D. A. Prediction of the PKa's of Aqueous Metal Ion +2 Complexes. *J. Phys. Chem. A* **2015**, *119* (12), 2926–2939.

(53) Lindqvist-Reis, P.; Muñoz-Páez, A.; Díaz-Moreno, S.; Pattanaik, S.; Persson, I.; Sandström, M. The Structure of the Hydrated Gallium(III), Indium(III), and Chromium(III) Ions in Aqueous Solution. A Large Angle X-Ray Scattering and EXAFS Study. *Inorg. Chem.* **1998**, *37* (26), 6675–6683.

(54) Yu, D.; Du, R.; Xiao, J.-C.; Xu, S.; Rong, C.; Liu, S. Theoretical Study of PKa Values for Trivalent Rare-Earth Metal Cations in Aqueous Solution. *J. Phys. Chem. A* **2018**, *122* (2), 700–707.

(55) Christe, K. O.; Dixon, D. A.; Schrobilgen, G. J.; Wilson, W. W. Tetrafluorophosphate Anion. *J. Am. Chem. Soc.* **1997**, *119* (17), 3918–3928.

(56) Jones, M. M.; Clark, H. R. Acid and Metal Salt Catalyzed Hydrolyses of PO2F2- and PO3F2-. *Inorg. Chem.* **1971**, *10* (1), 28–33.

(57) Tasaki, K.; Kanda, K.; Nakamura, S.; Ue, M. Decomposition of LiPF6 and Stability of PF5 in Li-Ion Battery Electrolytes. Density Functional Theory and Molecular Dynamics Studies. *ChemInform* **2004**, *35* (7).

Chapter 6 - Conclusion

In this dissertation, a mixture of dichalcogenides with different reactivities used for the synthesis of highly branched nanocrystals of ternary cadmium chalcogenides. Study of the effects of chalcogenide ratio, and reaction time on the morphology and composition of final QDs leads to the demonstration of shape evolution mechanism of QDs, and it's shown that simple tetrapod QDs and hyperbranched QDs can be obtained by controlling the reaction conditions.

Emissive QDs, were obtained through doping of hyperbranched ZnSeS QDs with Mn(II) ion which used for thiol sensation. It was observed that the more branched QDs have higher sensitivity to thiols.

The effect of ZnS shell thickness on the turn-on luminescence thiol sensing of spherical Mn:ZnSe@ZnS in the aqueous and organic matrix was studied. It observed that QDs with thin have highest sensitivity in organic medium but no performance in an aqueous matrix. Thick ZnS shell causes QDs to have a very low sensitivity to thiols. QDs with medium-thick ZnS shell, give the best performance in the aqueous medium. The NCs had no performance for thiol sensing using MRI. In our study, we have not optimized our NCs preparation steps for MRI study.

We also studied HF free post-synthetic etching of InP NCs under mild condition using $InCl_3$ and Bu_4NPF_6. To best of our knowledge, it is the first report on the etching of InP NCs in such condition. Luminescent NCs with different sizes obtained by tuning the etching process using different amounts of $InCl_3$. NMR studies show formation of PH_3, BF_4^- and $H_2PO_2F_2$ in the reaction mixture. Formation of these species indicates that the etching process is probably due to the formation of acid in the reaction mixture. The mechanism of the etching is not revealed fully in detail yet and understanding it will help more precise control over the etching process for obtaining NCs better optoelectronic properties.